Mixed Imaging Sequences for Improved Spatiotemporal Resolution in Cardiac Imaging

by

Blake Herrema

B.S., Dordt University, 2019

A thesis submitted to the

Faculty of the Graduate School of the

University of Colorado in partial fulfillment

of the requirements for the degree of

Master of Science

Department of Biomedical Engineering

2022

Committee Members:

Nick Bottenus, Chair

Mark Borden

Stephen Becker

Herrema, Blake (M.S., Biomedical Engineering)

Mixed Imaging Sequences for Improved Spatiotemporal Resolution in Cardiac Imaging

Thesis directed by Dr. Nick Bottenus

Ultrasound imaging of the heart is a vital diagnostic tool in modern medicine. The heart resides in a challenging imaging environment and exhibits a variety of tissue velocities. Therefore, high frame-rate ultrasound sequences are required that can penetrate depth and resolve motion. Modern imaging strategies often transmit either focused waves or broad waves. This work investigated the potential to use REFoCUS, an element-based beamforming method, to combine focused and broad transmissions within a mixed sequence. First, consistency of REFoCUS in the presence of motion was considered both in simulation and experimentally, as compared to virtual source beamforming. By imaging a moving point target, the point spread function (PSF) from differing motion cases was evaluated quantitatively. Each PSF was plotted as a contour plot in order to calculate the metrics of cystic contrast and cystic resolution. Second, REFoCUS was used to beamform mixed RF data that included transmissions from both focused and broad waves. The goal of designing a mixed sequence was to combine the reduced sensitivity to motion offered by focused waves with the ability to increase frame-rate offered by broad waves. The same metrics of contour plots, cystic contrast, and cystic resolution were used here. Applying weighting to mixed sequences reduced motion sensitivity in sequences incorporating broad waves, thereby improving the performance of select mixed sequences. Overall, this work showed that REFoCUS performs comparably to virtual source in terms of motion sensitivity, confirmed that focused transmissions are less sensitive to motion than broad waves, and created a mixed sequence that combines the benefits of focused and broad wave transmissions.

Dedication

To my family and to my God.

Acknowledgements

I would like to extend my sincerest gratitude to my advisor, Dr. Nick Bottenus, who not only introduced me to the fundamentals of ultrasound and synthetic aperture imaging, but also supported me throughout the research process and provided invaluable feedback. Also, I am thankful for Dr. Mark Borden and Dr. Stephen Becker and the crucial roles they played serving on my committee. Furthermore, I am very grateful for the assistance that Laura Lewis provided as I navigated deadlines and approached graduation. Furthermore, I would like to acknowledge Melton Parham and Nazli Javadi, the other members of the Bottenus Lab, for engaging in discussions about ultrasound and for sharing in the highs and lows of graduate school. Lastly, I would like to thank my friends and family for supporting me the last two years. In particular, I am grateful to my brothers, Jordan and Austin Herrema, for expressing genuine interest in my work and offering insights from their research experience.

Contents

Chapter

1 Introduction **1**

1.1 Importance of Ultrasound Imaging 1

1.2 Cardiac Ultrasound 1

1.3 Modern Echocardiography Techniques 2

1.4 In-Vivo Challenges in Echocardiography 4

1.5 Beamforming Methods 5

1.6 REFoCUS Beamforming 9

2 Methods **12**

2.1 Experimental Setup 12

2.2 Simulation Setup 14

2.3 Motion Sensitivity - Virtual Source vs. REFoCUS 15

2.3.1 Moving Point Target - Simulation 15

2.3.2 Moving Point Target - Experimental Validation 20

2.4 Mixed Sequences 20

2.4.1 Data Combination 20

2.4.2 Moving Point Target - Mixed Sequences - Simulation 22

2.4.3 Moving Point Target - Weighted Mixed Sequences - Simulation 23

2.4.4 Speckle Phantom - Weighted Mixed Sequences - Image Uniformity 25

3 Results **26**

3.1 Motion Sensitivity - Virtual Source vs. REFoCUS 26

3.1.1 Moving Point Target - Simulation 26

3.1.2 Moving Point Target - Simulation - Opposite Direction 46

3.1.3 Moving Point Target - Experimental Validation 64

3.2 Mixed Sequences 75

3.2.1 Data Combination 75

3.2.2 Moving Point Target - Un-Weighted and Weighted - Mixed Sequences 75

3.2.3 Speckle Phantom - Weighted Mixed Sequences - Image Uniformity 87

4 Discussion **91**

4.1 Transmission Order in Mixed Sequences 91

4.2 Degradation Behavior in the Presence of Motion 92

4.3 Inherent Masking with REFoCUS 93

4.4 Relationship Between Resolution and Frame-Rate 94

4.5 Conclusions 95

4.6 Future Work 96

Bibliography **97**

Appendix

A Data Combination - Virtual Source vs. REFoCUS **100**

B Delay Matrices for Mixed Sequences **103**

Tables

Table

2.1 Observed Velocities from Simulated Point Target Motion 17

Figures

Figure

1.1 Linear and Phased Array Beamforming Comparison 6

1.2 Geometric Masks Applied for Virtual Source 8

2.1 Experimental Setup for Moving Point Target 13

2.2 Sample Contour Plot and Sample CR Curve 19

3.1 Simulation - Lateral Motion - Plane Waves - PSFs 28

3.2 Simulation - Lateral Motion - Focused Waves - PSFs 29

3.3 Simulation - Lateral Motion - Off-Focus - PSFs 30

3.4 Simulation - Lateral Motion - Plane Waves - CR Curves 33

3.5 Simulation - Lateral Motion - Focused Waves - CR Curves 34

3.6 Simulation - Lateral Motion - Off-Focus - CR Curves 35

3.7 Simulation - Lateral Motion - Cystic Resolution 36

3.8 Simulation - Axial Motion - Plane Waves - PSFs 38

3.9 Simulation - Axial Motion - Focused Waves - PSFs 39

3.10 Simulation - Axial Motion - Off-Focus - PSFs 40

3.11 Simulation - Axial Motion - Plane Waves - CR Curves 43

3.12 Simulation - Axial Motion - Focused Waves - CR Curves 44

3.13 Simulation - Axial Motion - Off-Focus - CR Curves 45

3.14 Simulation - Axial Motion - Cystic Resolution 46

3.15 Simulation - Opposite Lateral Motion - Plane Waves - PSFs 48
3.16 Simulation - Opposite Lateral Motion - Focused Waves - PSFs 49
3.17 Simulation - Opposite Lateral Motion - Off-Focus - PSFs 50
3.18 Simulation - Opposite Lateral Motion - Plane Waves - CR Curves 52
3.19 Simulation - Opposite Lateral Motion - Focused Waves - CR Curves 53
3.20 Simulation - Opposite Lateral Motion - Off-Focus Waves - CR Curves 54
3.21 Simulation - Opposite Lateral Motion - Cystic Resolution 55
3.22 Simulation - Opposite Axial Motion - Plane Waves - PSFs 57
3.23 Simulation - Opposite Axial Motion - Focused Waves - PSFs 58
3.24 Simulation - Opposite Axial Motion - Off-Focus - PSFs 59
3.25 Simulation - Opposite Axial Motion - Plane Waves - CR Curves 60
3.26 Simulation - Opposite Axial Motion - Focused Waves - CR Curves 61
3.27 Simulation - Opposite Axial Motion - Off-Focus - CR Curves 62
3.28 Simulation - Opposite Axial Motion - Cystic Resolution 63
3.29 Experimental - Lateral Motion - Plane Waves - PSFs 65
3.30 Experimental - Lateral Motion - Focused Waves - PSFs 66
3.31 Experimental - Lateral Motion - Plane Waves - CR Curves 67
3.32 Experimental - Lateral Motion - Focused Waves - CR Curves 68
3.33 Experimental - Axial Motion - Plane Waves - PSFs 70
3.34 Experimental - Axial Motion - Focused Waves - PSFs 71
3.35 Experimental - Axial Motion - Plane Waves - CR Curves 72
3.36 Experimental - Lateral Motion - Axial Waves - CR Curves 73
3.37 Experimental - Lateral and Axial Motion - Cystic Resolution 74
3.38 Mixed Sequences - Control Images - Lateral 76
3.39 Mixed Sequences - Lateral - Contour Plots 77
3.40 Mixed Sequences - Lateral - CR Curves - Adding 79
3.41 Mixed Sequences - Lateral - CR Curves - Replacing 80

3.42 Mixed Sequences - Lateral - Cystic Resolution 81

3.43 Mixed Sequences - Axial - Control Images 82

3.44 Mixed Sequences - Axial - Contour Plots 83

3.45 Mixed Sequences - Axial - CR Curves - Adding 85

3.46 Mixed Sequences - Axial - CR Curves - Replacing 86

3.47 Mixed Sequences - Axial - Cystic Resolution 87

3.48 Speckle Phantom - Control Images 88

3.49 Speckle Phantom - Mixed Sequences 89

4.1 Middle 10 Focused Transmissions Added - Before and After 92

A.1 Plane and Focused Baseline PSFs - Virtual Source and REFoCUS 101

A.2 Mixed Sequence PSFs - Virtual Source and REFoCUS 102

B.1 Delay Matrices - Plane and Focused 103

B.2 Delay Matrices - ‘Adding’ Mixed Sequences 104

B.3 Delay Matrices - ‘Replacing’ Mixed Sequences 105

Chapter 1

Introduction

1.1 Importance of Ultrasound Imaging

Ultrasound imaging has become an indispensable tool across clinical settings over the course of the last 70 years. With high portability, high ease-of-use, and low cost, ultrasound is the default imaging modality for many rapid diagnoses. Ultrasound images of deep tissues can be produced with excellent spatial resolution and real time imaging allows ultrasound to be used to guide sensitive surgeries. Microbubbles can be used as contrast agents to further improve image quality and even to quantify tissue perfusion. Ultrasonic waves can also deposit energy locally for therapeutic purposes such as tissue ablation, blood-brain-barrier disruption, and targeted drug delivery. Overall, ultrasound is a vital imaging technique for modern medicine [17].

1.2 Cardiac Ultrasound

Cardiac ultrasound, often referred to as "echocardiography," is the primary tool for diagnosing and characterizing cardiovascular conditions such as ischemia, heart failure, and structural heart disease [9]. Although heart failure does not have a universally agreed upon definition, it was designated as an emerging epidemic in 1997 and remains one of the most important causes of morbidity and mortality in the world [11][30]. Heart failure is commonly an end-stage manifestation of heart disease and, as of 2021, is present in $\sim$1.8% of Americans, 1.5-1.9% of Canadians, and 1-2% of Europeans [30]. Echocardiography's applications are not limited, however, to heart failure. Given an incidence of 4-12 per 1,000 live births, congenital heart disease is also prevalent. As a

portable, non-invasive, and real-time imaging modality, ultrasound is the first choice for evaluating abnormalities in the hearts of newborns and adults alike [3].

The most widely implemented types of cardiac ultrasound, transthoracic echocardiography (TTE) and transesophageal echocardiography (TEE), offer different views of the heart based on the location of the ultrasound transducer. With TTE the heart can be imaged via the following standard views: the parasternal long axis, parasternal short axis, apical 4-chamber view, subxiphoid view, and the suprasternal view. With TEE, the heart can be imaged through the five chamber view, four chamber view, mitral chamber view, two chamber view, long axis view, and ascending aorta long axis view. Each view offers distinct advantages and disadvantages [2]. The standard mode of imaging, B-mode imaging (or, brightness mode), generates structural images based on emitted ultrasonic waves and the magnitude and timing of received echoes. Doppler-mode imaging, meanwhile, relies on phase shifts (i.e., doppler shifts) in received echoes caused by blood flow in order to evaluate complex blood flow dynamics in the heart [27].

Echocardiography can quantify cardiac function through a wide variety of metrics. As an example, left ventricular ejection fraction (LVEF) is a measure of left ventricular (LV) systolic function. LVEF gives the ratio of the volume of blood ejected from the LV during systole over the volume of blood in the LV at the end of diastole [18]. LVEF values less than 30% are considered abnormal and values over 50% are considered healthy, but values between 30-50% are inconclusive. Modern echocardiography, therefore, only has the resolution and reliability to identify LVEF physiologies that are clearly abnormal or clearly normal [30]. While other metrics for measuring heart health do exist, improved resolution in both **time** and **space** is required to diagnose heart disease with greater accuracy.

1.3 Modern Echocardiography Techniques

The relationship between temporal resolution, spatial resolution, and field of view is paramount for cardiac imaging. As an example, constructing a 2D cardiac image via conventional methods may involve 180 pulse-echo measurements (or, 180 transmissions) ranging across a 90°field of view.

The resulting line spacing is 0.5°, and a single image line is reconstructed from each transmission. Assuming an 18 cm round trip from thoracic wall to atrial roof and a speed of sound in soft tissue of 1540 m/s, a single transmission takes approximately 117 µs, or about 8,500 transmissions per second. With 180 transmissions per frame, a frame takes 21 ms to generate, giving a final frame-rate of ∼28 Hz. Since the location of the heart and the speed of sound in the body cannot be changed, the only way to increase frame-rate (temporal resolution) is to reduce the number of transmit events per frame. Two simple solutions exist: narrowing the range of the scan preserves spatial resolution while sacrificing field-of-view and reducing line density preserves field-of-view at the cost of spatial resolution [10].

State-of-the-art systems employ a variety of techniques to preserve both spatial resolution and field-of-view. Multiline acquisition (MLA) simultaneously "beamforms" (reconstructs) multiple neighboring lines using time delays to steer each line off-axis from the center of the transmission. "4MLA" systems for example reconstruct 4 lines in parallel in order to increase the system's frame-rate 4-fold. One requirement for MLA, however, is that the transmit beam must be broadened such that region of the image being reconstructed in each line is properly insonified. Broad beams, as opposed to focused beams, generally lead to reduced lateral resolution. Moreover, these broad beams are transmitted from only a portion of the transducer's aperture, limiting the amount of energy in each transmission, ultimately, reducing signal-to-noise ratio (SNR). Some systems fully embrace broad transmissions, utilizing plane and/or diverging waves. In this context, plane and diverging waves are transmitted from the transducer's full aperture. These unfocused beams allow multiple lines to be reconstructed in parallel while preserving energy penetration. In fact, entire images can be reconstructed from a single broad transmission and then combined with coherent compounding. Combination of these images can achieve an effective gain in frame-rate similar to that of 4MLA systems (∼130 Hz). Crucially, however, compounding plane wave transmissions in the presence of tissue motion can result in noticeable image artifacts [4][36].

One final alternative to MLA and plane/diverging waves is multiline transmit imaging (MLT). MLT systems transmit multiple focused beams simultaneously, distributed across the region being

imaged. Although MLT has received little acclaim, recent research indicates that MLT and MLA can be combined (e.g., 4MLT 4MLA) to achieve further frame-rate improvements [10]. The costs of increasing frame-rate, of course, are spatial resolution and SNR. In a study involving expert cardiac image readers, the majority of experts preferred 4MLT images over more aggressive MLT configurations with even higher frame-rates [34].

1.4 In-Vivo Challenges in Echocardiography

Motion in the field of view, particularly when imaging with broad waves, constitutes a significant challenge for ultrasound imaging. Recall that the successful compounding of plane waves requires the image to be temporally coherent; if tissue moves between transmissions, the summed images will no longer be phase-aligned [36]. Motion is a problem for conventional imaging modalities as well. Focused waves behave similarly to broad waves when targets are located away from the focal depth [19]. Therefore, focused transmissions are still susceptible to motion, but may be able to resolve it more effectively than broad transmission, particularly if motion is near to the focus.

During contraction, the heart exhibits a wide range of tissue velocities. A prominent feature of the heart, the myocardium, is commonly evaluated when considering heart health. By tracking the speckle pattern near and within the myocardium (or by using doppler imaging), the position of the myocardium can be tracked in order to calculate many metrics, including LVEF [5]. In-vivo measurements of myocardial motion suggest that the velocity of the myocardium can reach around $\sim$3-4 cm/s [33]. The annulus of the mitral valve, which regulates blood flow from the left atrium into the left ventricle, moves at a rate of ranging from $\sim$8-10 cm/s over systole and diastole. [8][32]. Also, the mitral valve leaflets move faster than perhaps any other tissue in the body with estimated peak opening velocities of $\sim$40 cm/s and peak diastolic closure rates of $\sim$25 cm/s [35]. At 40 cm/s, mitral valve leaflet velocity is an order of magnitude higher than myocardial velocity; resolving all magnitudes of motion in the heart is a significant challenge. Interestingly, mitral valve annulus velocity has been shown to differ significantly between healthy hearts and hearts with moderate to severe aortic valve stenosis, further reinforcing the notion that being able to resolve motion in the

heart is of great importance.

In addition to exhibiting significant tissue motion, the heart is also located in an acoustically challenging environment. The ribs, which are comprised of compact bone, almost completely attenuate the propagation of an ultrasound beam [31]. Thus, imaging between the ribs is a necessity. Aside from ribs, the thoracic wall also contains a significant amount of heterogenous muscle and fat. The differing speeds of sound in muscle, fat, and other tissues in the thoracic cavity cause aberration in ultrasonic beams. The result is that many patients cannot be imaged with TTE without the use of contrast agents, and some even require cardiac magnetic resonance [21]. As the incidence and prevalence of obesity rises, the percentage of patients that cannot be imaged with TTE will also increase. Ultrasonic penetration depth can be increased by transmitting lower frequency waves, however low frequency waves have reduced resolution. Again, echoes from deeper targets take longer to return to the transducer, reducing temporal resolution. Utilizing TEE can bypass some of these obstacles, but it can only offer a limited number of views of the heart; many diagnostic procedures require views of the heart offered by TTE [24]. Once again, improved spatial and temporal resolution in echocardiography is required at clinically relevant depths.

1.5 Beamforming Methods

The reconstruction of an image from any number of transmit and receive events is often referred to as beamforming. Specifically, beamforming involves (1) transmit beamforming: shaping the spatial distribution of the pressure field amplitude in the region of interest (ROI) and (2) receive beamforming: the consequent recombination of received ultrasound echo signals. In total, one must know the location of each element, the assumed speed of sound in the ROI, and the times at which each element transmits and receives. Even though a wide variety of beamforming methods exist, the goal remains the same: to focus received echoes and generate an accurate image of the ROI.

One important distinction to make when beamforming is between *linear* and *phased* arrays. On a linear array, elements are grouped into a sub-aperture. A sub-aperture is defined to transmit and receive a particular waveform in front of that sub-aperture; this transmit and receive process

produces an "A-line." Subsequently, the sub-aperture is linearly shifted over the width of the array in order to produce multiple A-lines, thereby producing an image line by line. Phased arrays, in contrast, use the entire aperture width for every transmission. Elements of a phased array can be adjusted to transmit with a unique phase (i.e., time shift) in order to transmit the desired wavefront. The differences between linear and phased arrays are illustrated in Figure 1.1 [12]. One advantage of a phased array is that transmissions can be steered beyond the extent of the transducer's aperture. This steering is advantageous in situations such as TTE, in which the transducer's physical access to the ROI is restricted (by the ribcage), but a wide field-of-view is still desired [12]. All transducers and beamforming techniques described in this work make use of phased arrays.

Many modern systems implement synthetic aperture (SA) beamforming, a highly versatile technique for improving contrast, frame rate, image uniformity, or a number of other parameters [26]. As opposed to defining a single aperture, SA synthesizes information from either multiple sub-apertures or multiple steered transmissions received on the full aperture in order to extend the *effective* aperture size [37]. Beamforming methods must be adjusted accordingly. Received signals are properly shifted in time by taking into account the geometric distance between each

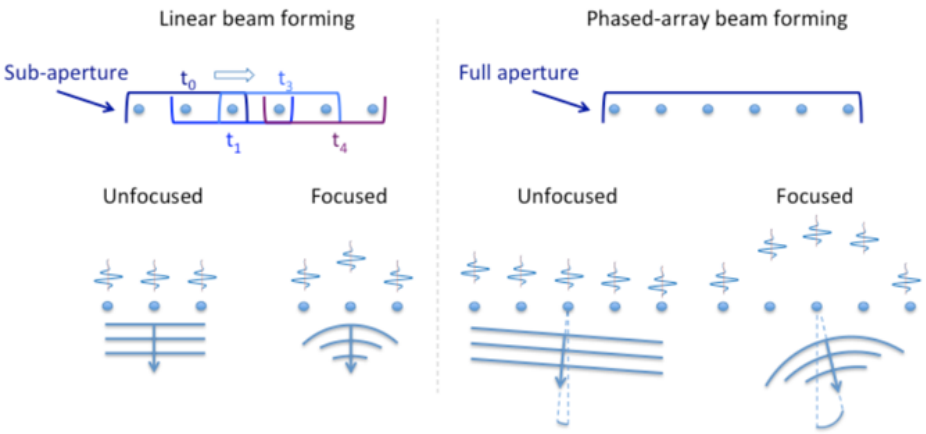

Figure 1.1: Comparison of linear and phased array beamforming. Unfocused and focused beams shown for both. Phased arrays can steer beams beyond the aperture extent © 2018 *Appl. Sci.* [12]

transmitting element and each receiving element. By assuming a constant speed of sound in the imaging volume, appropriate phase shifts are calculated for each element during each transmission, and all transmissions are combined into a final image [12]. The overlap between transmissions, when combined with these appropriate shifts, provides focusing throughout the image instead of at a single point.

The virtual source model, a type of SA beamforming, assumes that waves diverge spherically from an effective point source. The location of this point source depends on the desired waveform: in front of the array corresponds to focused waves, behind the array to diverging waves, and at infinity to plane waves (Figure 1.2). Path length differences are removed from received signals by calculating transmit time-of-flight according the distance between an element and the virtual source. With n transmissions and T elements, a given time delay τ_{nT} is calculated according to Equation 1.1 for focused waves, Equation 1.2 for plane waves, and Equation 1.3 for diverging waves. (x_f,z_f) gives the position of the virtual source, x_n gives the element position, c is the speed of sound, and θ is the steering angle used to direct plane waves [6].

$$\tau_{nT} = \frac{\sqrt{x_f^2 + z_f^2} - \sqrt{(x_f - x_n)^2 + z_f^2}}{c} \tag{1.1}$$

$$\tau_{nT} = \frac{x_n sin\theta}{c} \tag{1.2}$$

$$\tau_{nT} = \frac{\sqrt{(x_f - x_n)^2 + z_f^2} - \sqrt{x_f^2 + z_f^2}}{c} \tag{1.3}$$

Slightly different than virtual source beamforming is 'dynamic receive,' or 'dynamic focusing.' Dynamic receive beamforming is simpler than virtual source in that it applies a single set of delays upon transmitting a focused wave. On receive, however, different focusing delays are used for each depth. Compared to conventional methods, dynamic receive provides improved resolution away from the focal point [13]. The dynamic receive beamforming performed in this work also implemented parallel receive beamforming with weighting applied; receive lines located further

from the transmit line were given less weight than those near the transmit line.

Beamforming often includes the application of a geometric mask, outlining the shape of the transmitted waveform, in order to reduce side lobes and off-axis clutter. For a given transmission, only signals received from within the mask are recorded [12]. Masks for plane and diverging waves are fairly intuitive, whereas focused masks are more complex. The standard hourglass shape used to spatially mask focused waves is too narrow near the focal point. Assuming planar wave propagation near the focal point allows for the reconstruction of pixels between the focal points of neighboring beams [25]. The shapes of focused, plane, and diverging wave geometric masks are shown in Figure 1.2 [6]. Note that the planar region near the focal point of the focused transmission is not shown in this configuration. Mask width is the defining parameter for geometric masks. Focused waves and plane waves are the two key wave shapes utilized herein. Mask width for focused waves describes the width of the planar region near the focus, and mask width for plane waves describes the uniform width of the planar mask.

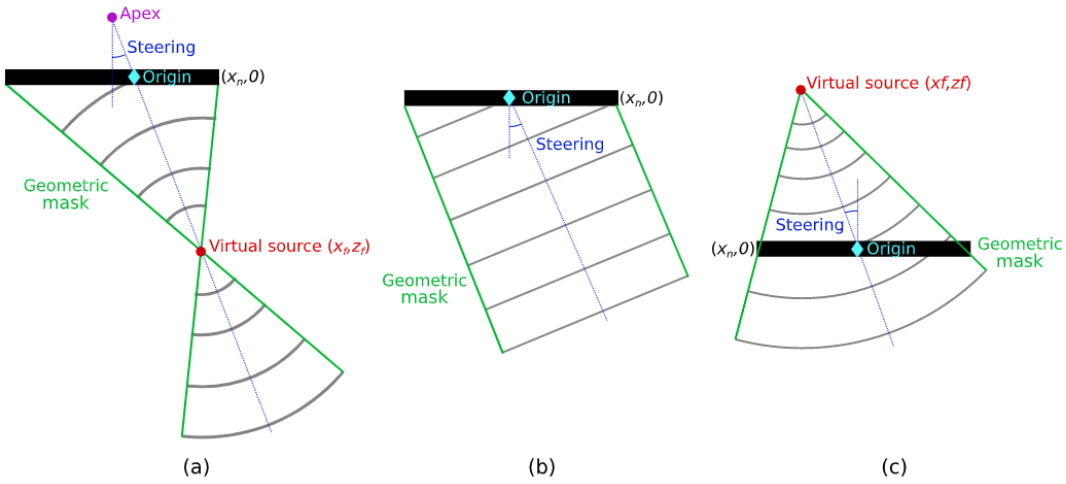

Figure 1.2: Geometric masks applied to (a) focused wave, (b) plane wave, and (c) diverging wave transmissions © 2018 IEEE [6]

1.6 REFoCUS Beamforming

Retrospective encoding for conventional ultrasound sequences (REFoCUS) was developed as an alternative to virtual source, synthetic aperture beamforming. Rather than assuming a spatial relationship between each element and the point source, REFoCUS isolates the contributions of individual transmit elements by phase shifting the transmitted signals according to applied transmit delays. In essence, an element's contribution to any given pixel in an image can be described as a diverging wave time shifted by the appropriate amount. By removing the delays that were applied during transmit (to generate the desired wave shape) with a frequency-domain linear decoding process, the complete data set can be recovered [7].

Focusing the transmit pressure field in the frequency domain both enables key pseudoinversion techniques and improves computational efficiency . In the frequency domain, a time shift can be described as a function of ω. For each transmission, n, and each element, T, time delays can be written as exponentials, as shown in Equation 1.4. The columns of the encoding matrix, $\boldsymbol{H}$, represent transmissions, and the rows represent elements. Furthermore, $\boldsymbol{S}$ is a vector of the Fourier transform of the recorded backscattered responses from the transmissions, and $\boldsymbol{U}$ is a vector of the Fourier transform of the backscattered response from individual elements, which is the intended output of REFoCUS. The linear system in Equation 1.5 illustrates the relationship between $\boldsymbol{H}$, $\boldsymbol{S}$, and $\boldsymbol{U}$. The conjugate transpose matrix $\boldsymbol{H^*}$, Equation 1.6, applies the opposite phase shift of the applied transmit delay, note that the signs of the exponentials are opposite to those of $\boldsymbol{H}$. [7]. Ideally, ($\boldsymbol{HH^*}$) would give the identity matrix, but the conjugate transpose (or 'adjoint' method) is not a perfect pseudoinversion method. A more robust method, Tikhonov Regularization, is introduced in Equation 1.7, giving $\boldsymbol{H^\dagger}$, according to the regularization parameter $\boldsymbol{\Gamma}$ [1]. Finally, an approximation of $\boldsymbol{U}$, $\boldsymbol{\hat{U}}$, is obtained, as shown in Equation 1.8.

$$\boldsymbol{H} = \begin{bmatrix} e^{-j\omega\tau_{1,1}} & e^{-j\omega\tau_{2,1}} & \dots & e^{-j\omega\tau_{N,1}} \\ e^{-j\omega\tau_{1,2}} & e^{-j\omega\tau_{2,2}} & \dots & e^{-j\omega\tau_{N,2}} \\ \vdots & \vdots & \ddots & \vdots \\ e^{-j\omega\tau_{1,M}} & e^{-j\omega\tau_{2,M}} & \dots & e^{-j\omega\tau_{N,M}} \end{bmatrix} \tag{1.4}$$

$$\boldsymbol{S} = \boldsymbol{U}\boldsymbol{H} \tag{1.5}$$

$$\boldsymbol{H}^* = \begin{bmatrix} e^{j\omega\tau_{1,1}} & e^{j\omega\tau_{1,2}} & \dots & e^{j\omega\tau_{1,M}} \\ e^{j\omega\tau_{2,1}} & e^{j\omega\tau_{2,2}} & \dots & e^{j\omega\tau_{2,M}} \\ \vdots & \vdots & \ddots & \vdots \\ e^{j\omega\tau_{N,1}} & e^{j\omega\tau_{N,2}} & \dots & e^{j\omega\tau_{N,M}} \end{bmatrix} \tag{1.6}$$

$$\boldsymbol{H}^{\dagger} = (\boldsymbol{H}^*\boldsymbol{H} + \boldsymbol{\Gamma}^*\boldsymbol{\Gamma})^{-1}\boldsymbol{H}^* \tag{1.7}$$

$$\hat{\boldsymbol{U}} = \boldsymbol{S}\boldsymbol{H}^{\dagger} = \boldsymbol{U}(\boldsymbol{H}\boldsymbol{H}^{\dagger}) \tag{1.8}$$

Interestingly, since REFoCUS utilizes applied transmit delays rather than assuming a spatial relationship between elements and a virtual source, the technique can be applied to any focused transmission; geometric masks are not required. Standard beamformers apply the same physical assumptions to every transmission when reconstructing an image, so a mixture of wave shapes cannot be used to generate a single frame. Meanwhile, REFoCUS presents a generalized beamforming technique that can reconstruct images from any mixture of focused, plane, and diverging wave transmissions, and even others. REFoCUS presents a new flexibility for echocardiography sequence design. The proper combination of plane waves, which improve temporal resolution at the cost of spatial resolution, and focused waves, which improve spatial resolution at the cost of temporal resolution, may allow for the localized resolution of motion in the heart without compromising clinically relevant frame-rates.

Herein, I hypothesize that a mixed transmit sequence, with focused and plane waves will improve spatiotemporal resolution when imaging the heart by better resolving cardiac motion. The specific aims of this work are as follows: (1) to characterize motion sensitivity of the REFoCUS beamforming method as compared to virtual source beamforming across various beam geometries, and (2) to develop a novel ultrasound imaging sequence to improve spatiotemporal resolution in volumes of interest that contain both static and dynamic targets.

Chapter 2

Methods

2.1 Experimental Setup

In order to evaluate the motion sensitivity of REFoCUS beamforming, images of a point target were beamformed with REFoCUS and compared to those with virtual source **plane** and virtual source **focused** beamforming. Imaging a point target provides a system's response to a point source, also known as a point-spread function (PSF). The size of the PSF is indicative of the resolution of a given imaging sequence. Imaging a moving point target and considering the resultant PSF, therefore, enabled the determination of a system's effective resolution in the presence of motion.

For simplicity, point target motion was synthesized by holding a point target fixed in space and moving the ultrasound transducer. The Aims III Scan Tank (Onda Corporation, Sunnyvale, CA), Figure 2.1a, offered both an environment in which to image and a precise translation stage for controlling the position of the transducer. The Aims III Scan Tank had a positioning repeatability of less than 5 μm, a step size in all three dimensions of 5.5 μm, and was compatible with Soniq: the companion software of the Aims III scan tank. External control of Soniq was made possible with a library of Matlab commands. Nylon wire with a 0.1 mm diameter was strung between two supports and placed between the ultrasound transducer and a viscoelastic urethane sheet (Sorbothane, Kent, OH) on the bottom of the tank, as shown in Figure 2.1b. The transducer used in this setup was a Verasonics P4-2V, a 64-element phased array transducer with center frequency 3 MHz. 3 MHz is a common center frequency for echocardiography applications [22]; the wavelength of this center

frequency is about 0.51 mm. The ethylene sheet improved the final image by reducing the severity of backscattered echoes from the bottom of the scan tank. In this configuration, the point target itself did not move, rather, the ultrasound transducer moved a specified distance between transmissions. Based on the imaging depth (50 mm), speed of sound (1540 m/s), and number of transmissions (128), motion between transmissions could be described as a constant velocity during the generation of a single frame.

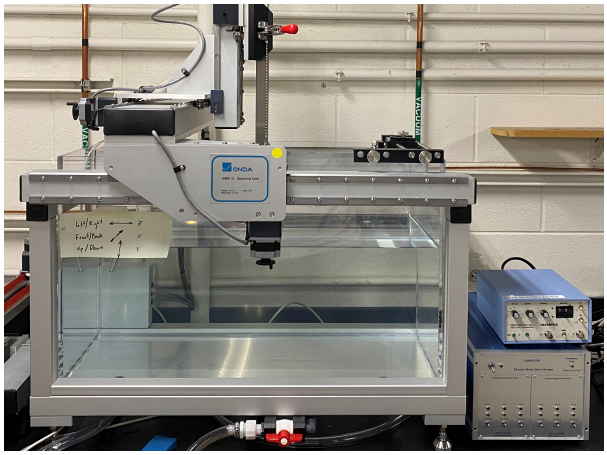

(a) Onda Aims III Scan Tank

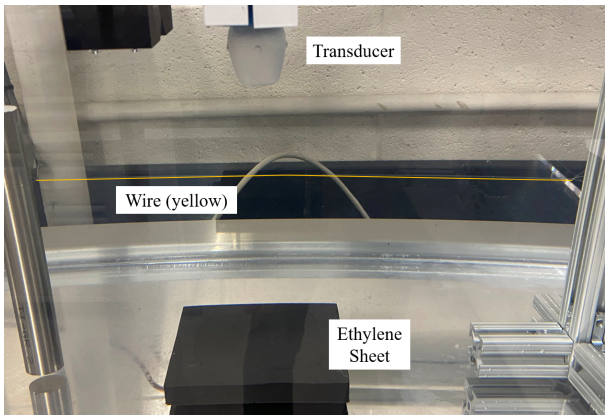

(b) Fixed point target in scan tank

Figure 2.1: Experimental setup for imaging a moving point target - Note that the wire is labelled in yellow for visual clarity

The Verasonics Vantage 256 Research Scanner, used to program and record imaging sequences, was connected to Soniq in order to move the scan tank's translation stage between transmissions, essentially alternating (1) transmit/receive events and (2) motion by a set increment. Before use, the motion stage was initialized: moving the stage to its default position, setting translation speeds to the default value, and orienting all axes correctly.

Once compiled, motion-interleaved sequences were run in Matlab. Accordingly, control of Soniq (and thereby, the Aims III Scan Tank) via Matlab was incorporated into the Vantage imaging sequence. Matlab commands that control the position of the translation stage were tied to controls on the GUI in order to position the target before initiating a sequence. Furthermore,

user-defined Matlab functions that moved the translation stage a specified distance on a specified axis were placed after transmit/receive events, ensuring that the translation stage moved between transmissions. Since Soniq did not return control to Matlab until it finished moving the translation stage, all movements were guaranteed to finish before another transmission began. Further verification of coordination between Soniq and Matlab was achieved by placing a 'sync' function after the translation stage was moved. The sync function synchronized the hardware and software sequencers on the Vantage system such that the next event could not begin before the current event finished. For each transmit and receive event, RF data from individual channels were saved.

The data from a Verasonics scan are processed in Matlab are beamformed with either virtual source methods or REFoCUS and compared. In all cases, images were plotted with a dynamic range of -50 to 0 dB and their sampling was verified by visualizing the frequency content of each PSF in K-space. Dynamic receive beamforming was also implemented for the focused sequences to introduce another comparison with a standard beamforming method.

Overall, this experimental setup enabled the characterization of REFoCUS' motion sensitivity with a real data set, as well as the quantification of resolution degradation as velocity increased. Future sections will describe both processes in detail, as well as the specific sequences investigated.

2.2 Simulation Setup

Imaging a point target experimentally provided real pulse-echo data, but it also introduced imperfect imaging conditions and added complexity when iterating many motion profiles. Simulating a moving point target was made possible by Field II, a program first developed in the 1990s for simulating ultrasound scans [14][15]. Imaging sequences simulated in Field II were processed in the same manner as data from the Vantage system, allowing for comparisons between REFoCUS and virtual source beamforming techniques in the presence of motion.

The first step in simulating an ultrasound scan was to generate a virtual transducer. The following general properties were set: speed of sound (1,540 m/s), center frequency (3 MHz), sampling frequency (120 MHz), and fractional bandwidth (0.8). Center frequency was set to 3

MHz to match echocardiography. Lateral dimension geometric properties were also set: number or elements (128), kerf (0.01 mm), pitch (0.2567 mm), element width (0.2467 mm), number of sub-elements (1), and lateral focus (50 mm). Given that this is not a simulated array, the number of elements in the elevational dimensions was set to 1. The final components of a simulated transducer were its impulse response and excitation. In order to generate a simulated phantom, the location of point targets, cysts, or lesions was provided, along with the location of any speckle patterns. Although speckle makes simulations more similar to *in vivo* images, processing speckle can be quite computationally intensive. For this reason, the simulations presented herein did not include speckle.

After a transducer and phantom were generated, Field II simulated one transmission at a time, for a user-defined n transmissions. In this setup, each transmission had a unique phantom. In the same way that the experimental setup moved the transducer by a set increment between transmissions, the simulated point target was located in a new location for every transmission, separated by the desired motion increment. After every transmission was simulated, they were stitched together into a single data set and saved in a format compatible with both virtual source and REFoCUS beamforming in Matlab.

2.3 Motion Sensitivity - Virtual Source vs. REFoCUS

2.3.1 Moving Point Target - Simulation

Simulations were designed in Field II in order to compare virtual source and REFoCUS beamforming in the presence of motion and evaluate the performance of broad waves and focused waves. Ten motion cases were considered for both **lateral** and **axial** motion. Beginning with a stationary target, lateral motions range from 0.5 mm/frame to 10 mm frame and axial motions range from 0.1 mm/frame to 1.5 mm/frame (Table 2.1). The stationary case served as a baseline for each PSF, and motion cases for both directions spanned approximately one order of magnitude. The increments for axial motion were smaller than those for lateral motion because ultrasound is more sensitive

to axial motions than it is to lateral motions since axial resolution is directly tied wavelength (i.e., frequency). Spatial frequency in the axial direction is higher than the lateral direction, therefore requiring higher phase coherence; even small axial motions can produce significant phase shifts in the backscattered signal [36]. Total motions of 10 wavelengths (10λ) across the generation of a single frame have been shown to degrade image quality. This distance corresponds to approximately a tenth of a wavelength of motion (0.1λ) between transmissions [16]. Again, the simulated transducer had a center frequency of 3 MHz and a corresponding wavelength of $\sim$0.5 mm. Table 2.1 also shows each motion case in units of wavelengths/frame. Recall that motion in the mitral valve leaflets can reach velocities of approximately 40 cm/s. Lateral simulated velocities were designed to eclipse this 40 cm/s mark, but axial velocities of this magnitude produced significant degradation. Heightened sensitivity to motion in the axial direction confirmed the importance of designing sequences that can resolve motion and also highlighted axial motion as a focus for future experiments.

With the simulated point target positioned 50 mm below the transducer, the focal depth for the focused transmission was set to 50 mm and delays were calculated accordingly. all motion cases were designed such that the point target was positioned at (0,0,50) [mm] halfway through the sequence. Furthermore, every motion case was imaged with three sequences: (1) plane waves, (2) focused waves, and (3) off-focus waves. The 'off-focus' case made use of focused waves, but with the focal depth set to 40 mm. This sequence enabled comparisons between plane and focused transmit geometries even when motion is not isolated to the focal point. Each simulated sequence consisted of 128 transmissions, resulting in a line spacing of 0.4724°. Furthermore, mask width was set to 1 mm in the focused cases and to 30 mm in the plane case. Mask width for a focused wave refers to the width of the planar region around the focus and for a plane wave it refers to the width of the uniform plane shape (Figure 1.2). A Tukey window was applied to the focused mask.

Note that the primary difference between the plane and focused sequences was the shape of the transmit waveform. For a plane wave *without* steering, the transducer elements all fired at the same time, leading to a planar propagating wavefront. For an un-steered focused wave, the outermost transducer elements fired first, with increasing delays moving towards the inner elements.

The result of these delays was a focused acoustic wavefront. When steering was introduced, delays were adjusted to direct a wavefront with the same shape at the desired angle.

Table 2.1: Observed Velocities from Simulated Point Target Motion

Lateral			**Axial**		
[mm/frame]	*[λ/trans]*	*Velocity [cm/s]*	*[mm/frame]*	*[λ/trans]*	*Velocity [cm/s]*
0	0	**0**	0	0	**0**
0.5	0.008	**3.3**	0.1	0.002	**0.7**
1.0	0.015	**6.7**	0.2	0.003	**1.3**
1.5	0.023	**10.0**	0.3	0.005	**2.0**
2.0	0.030	**13.4**	0.4	0.006	**2.7**
3.0	0.046	**20.1**	0.5	0.008	**3.3**
4.0	0.061	**26.7**	0.75	0.011	**5.0**
5.0	0.076	**33.4**	1.0	0.015	**6.7**
7.5	0.114	**50.1**	1.25	0.019	**8.4**
10	0.152	**66.8**	1.5	0.023	**10**

Images were reconstructed over a 10 x 8 [mm] field of view around the point target in order to better quantify the differing effects of motion. In addition to zooming in on each PSF, contours were drawn at -30, -24, and -18 dB intensities [29]. These contours helped to highlight significant side lobes and demonstrate how centralized the energy in each PSF was.

The image quality of each motion case and its associated contour plot was quantified by the metric of cystic contrast, known also as relative intensity. Cystic contrast gives the ratio of energy oustide of a cyst, or any region of interest (ROI), to total energy in an image. The energy of a given region, and therefore cystic contrast, was calculated according to Equation 2.1 [28]. *P(x)* describes the PSF itself and *M(x)* describes the spatial mask used to differentiate between inside

and outside the ROI. Essentially, total energy is given by the sum of squares of intensity measurements in a given region. Plotting cystic contrast against an increasing radius (defining a ROI increasing in size) provided a contrast vs. radius curve (**CR curve**). CR curves are helpful for visualizing how dense a PSF's energy is, as well as how quickly its side lobes taper off. Both a sample contour plot and a sample CR curve for a stationary point target imaged by a planewave sequence are shown in Figure 2.2. Notice that as the radius of the ROI increases, cystic contrast decreases. The reason for this is that as the ROI gets larger, the total energy outside the ROI decreases, but the total energy in the image stays the same. The CR-curve for a well-resolved point target should be quite steep. The CR curve of a PSF that exhibits significant artifacting will drop more slowly, and portions of the curve that drop suddenly may indicate the edges of side lobes.

$$C_{t_o} = \sqrt{\frac{\int_{-\infty}^{\infty} P_{t_o}^2(\vec{x}) M^2(\vec{x})\, d\vec{x}}{\int_{-\infty}^{\infty} P_{t_o}^2(\vec{x})\, d\vec{x}}} = \sqrt{\frac{E_{t_o}^{out}}{E_{t_o}^{tot}}} = \sqrt{1 - \frac{E_{t_o}^{in}}{E_{t_o}^{tot}}} \tag{2.1}$$

Extending from the idea of a CR curve is the notion of **cystic resolution**. Cystic resolution, obtained from a CR curve, represents the radius of the largest target that can be resolved at a certain contrast under given imaging conditions. Here, the cutoff contrast was set at -20 dB such that the ROI radius at which cystic contrast equals -20 dB is the cystic resolution. The dotted black line in Figure 2.2b illustrates the determination of cystic resolution from a CR curve; the cystic resolution in this sample case is 0.66 mm. A low cystic resolution value corresponds with a steep CR curve, both of which correspond to a better-resolved image.

Contour plots were generated for every movement case listed in Table 2.1. CR curves were then generated for every movement case and cystic resolution was calculated accordingly. Note that the fidelity of cystic resolution is limited to 0.01 mm since cystic contrast was calculated for ROIs of radii increasing by 0.01 mm, ranging from 0 to 4 mm. Again, CR curves and cystic

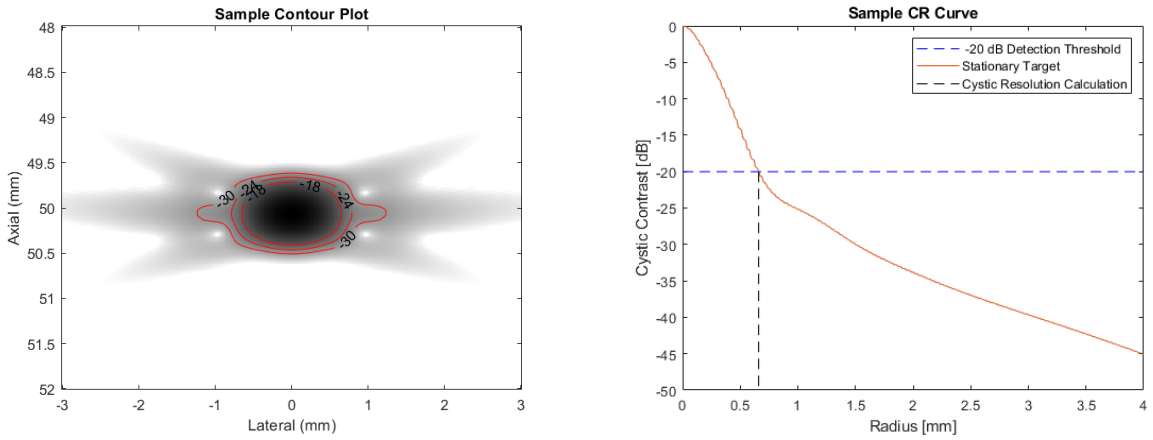

(a) Contour plot: contours at -30, -24, and -18 dB

(b) CR curve with cystic resolution 0.66 mm

Figure 2.2: Contour plot and CR curve for stationary point target imaged with plane waves

resolution values for every movement case helped to quantify resolution and degradation in the presence of motion. CR curve shapes were compared across transmit geometries and beamforming techniques. Cystic resolution was also plotted as a function of movement per frame, thus quantifying resolution in presence of motion for virtual source and REFoCUS beamforming. Sequences types (plane, focused, off-focus) were grouped on the same plots by direction of motion in order to better demonstrate the relative performance of each imaging type.

Since steered sequences have inherent directionality, all quantifications (contour plot, CR curve, cystic resolution) were repeated for lateral and axial motions in the opposite direction, for planewave, focused wave, and off-focus sequences. A scenario in which a point target is moving in the *same* direction as the transmit sweep insonifies the target much more than a scenario in which the point target is moving in the *opposite* direction as the transmit sweep. In the previous section, the point target moved from left to right and down to up, respectively. Similar simulations were designed with the point target moving laterally, from right to left, and axially, up to down. Each metric was compared to its opposite direction counterpart in order to evaluate the directional sensitivity of each imaging sequence and beamforming technique.

2.3.2 Moving Point Target - Experimental Validation

In order to verify results from simulated point target quantifications, the same lateral and axial motion cases (Table 2.1) were implemented experimentally. Imaging conditions were matched to simulations such that the point target was located at a depth of 50 mm and sequences consisted of 128 transmissions with 0.4724° spacing. Transmit voltage was set to 5 Volts so that the point target was clearly visible but no background noise was present. For brevity, only the primary direction of motion was considered in this experimental validation and the off-focus case was not considered. The same metrics - contour plots, CR curves, and cystic resolution - were utilized to quantify the degree of artifacting in each motion case. In this way, direct and quantitative comparisons between simulated and experimental data sets were established.

2.4 Mixed Sequences

2.4.1 Data Combination

The relationship between *spatial resolution* and *frame rate* is paramount when considering mixed sequences; both are crucial for imaging motion. Broad waves offer high frame-rate at the cost of increased sensitivity to motion, whereas focused waves provide reduced sensitivity to motion at the cost of reduced frame-rate. Broad waves and focused waves behave differently because broad wave transmissions have to be coherently combined to achieve adequate resolution. As such, broad waves are mostly helpful when imaging uniform volumes. The heart, which displays a wide range of tissue velocities, requires an ultrasound sequence that balances frame rate and resolution. Properly combining plane waves and focused waves may balance the high frame-rate afforded by plane wave transmissions and the reduced sensitivity to motion associated with focused waves.

Consequently, a number of questions were considered with REFoCUS in mind, including: how well mixed sequences could improve resolution in the presence of motion, whether or not beamforming a mixed set of transmissions would affect speckle, if the resolution of static targets away from the focal depth was reduced, and how effective weighting particular transmissions within

a sequence could be. In order to answer these questions, data from more robust Field II simulations were again combined in Matlab. Field II simulation was chosen in order to efficiently iterate sequences and determine the best method of combining **plane** and **focused** waves. Note that designing a mixed sequence, experimentally, is relatively easy with the Verasonics' programming structure. Transmit/receive events are explicitly specified, so plane and focused transmissions can be listed in the desired order.

Both virtual source and REFoCUS can be used to create images from mixed sequences. That said, data combination with virtual source beamforming took place after beamforming but before envelope detection. Therefore, transmit geometry specific beamforming was a requirement and each data set also had to be manually normalized. With REFoCUS, data sets could be combined *before* beamforming. In the context of REFoCUS, neither beamforming nor data combination were dependent on transmit type. In order to evaluate the simplicity of mixing sequences with REFoCUS, a simulation of 1 mm of axial motion (6.7 cm/s, Table 2.1) was devised in Field II and the resulting data sets were combined.

The first step in combining data sets for REFoCUS was to ensure compatibility in fast time. The number of samples in each transmission differed due to the fact that different transmit geometries required different delays. The first element firing in a focused wave emits sound earlier than that of a plane wave, even when steered at the same angle. To mitigate this difference in fast time, both time vectors were interpolated onto a single time vector. The target time vector spanned the earliest of both starting points and the latest of both end points. Following interpolation, both data sets had the same initial time. Note that even though differing transmit geometries can result in different time vectors, the interpolation method used here is applicable for any transmit geometry.

Swapping transmissions between data sets with the same initial time, then, was as simple as setting data from the chosen plane transmissions equal to the corresponding focused transmissions. Delay matrices were also adjusted accordingly. The delay matrix contained the delays for every element during every transmissions. Rows (transmissions) of the plane delay matrix were replaced

by the corresponding rows from the focused delay matrix. In addition to **replacing** plane transmissions with focused transmissions, focused transmissions were **added** to full plane wave sequences. Following proper data combination, mixed sequence images were beamformed with REFoCUS.

2.4.2 Moving Point Target - Mixed Sequences - Simulation

The simulations performed in Field II offered quantitative outputs describing the efficacy of mixing plane and focused waves; for consistency and ease of comparison, 128 transmissions comprised a single frame. For both sequences, *lateral* motion of 5 mm per frame and *axial* motion of 1 mm per frame was considered. These values correspond to observed velocities of 33.4 cm/s and 6.7 cm/s, respectively (Table 2.1). These motion cases demonstrated improved resolution when imaging with focused waves as opposed to plane waves. Moreover, both motion cases generated noticeable artifacts when imaged exclusively with plane waves, making them the ideal candidates for mixing the reduced motion sensitivity of focused waves with a high frame-rate plane sequence.

The controls for this test were the unmixed simulated data sets. Virtual source and REFoCUS beamforming were used to reconstruct images of lateral and axial motion imaged with plane and focused waves. Therefore, 4 virtual source control images were produced and 4 REFoCUS control images were produced: 2 with lateral motion and 2 with axial motion. Since the unmixed images were highly similar across beamforming methods, future mixed sequence were compared to only the REFoCUS control images. While mixed sequence images could be beamformed with both virtual source and REFoCUS, mixing sequences with REFoCUS was much simpler since data could be mixed pre-beamforming and no manual normalization was required.

The first type of mixed sequence investigated was 'adding' focused transmissions to full plane sequences. Adding transmissions increased the total number of transmissions required to generate an image, which would affect frame-rate negatively. 'Adding' cases included adding all focused transmissions (n = 256), adding the middle 10 focused transmissions to the beginning of the plane sequence (n = 138), adding the middle 10 focused transmissions to the end of the plane sequence (n = 138), adding every fourth focused transmission (n = 160), and adding every third focused

transmission (n = 171). The middle 10 focused transmissions were added to both ends of the plane wave sequence to evaluate whether or not transmission order played a role in beamforming.

The next type of mixed sequence was 'replacing' plane transmissions with the corresponding focused transmissions. The number of transmissions in each case remained constant (n = 128). The replacing cases would, theoretically, maintain the frame-rate of a plane wave sequence with locally improved resolution. Cases here included replacing the middle 10 transmissions, replacing the middle 20 transmissions, replacing the middle 30 transmissions, replacing every fourth transmission, and replacing every third transmission.

In both cases, adding and replacing, PSFs were compared to the control images. Qualitative estimations were made as to where each case fell between the focused and plane control images. Quantification of each PSF was performed in the same way as before (Section 2.3.1). Contour plots were generated for each PSF, CR curves were developed for each mixed sequence, and cystic resolution was calculated. Each of these metrics were produced for the REFoCUS control images as well. Beyond the quantification of each PSF, the delay matrix in each case was plotted with transmissions on the y-axis and elements on the x-axis. The delays that were added or replaced needed to correspond to the transmission that were added or replaced, otherwise, beamforming would not have been successful. Plotting the delay matrix more easily visualized which transmissions had been added or replaced.

2.4.3 Moving Point Target - Weighted Mixed Sequences - Simulation

Since focused waves showed improved resolution in the presence of motion, a technique for weighting focused transmissions more heavily than plane transmissions was devised. Weighting makes use of 'weighted least squares,' a linear regression method that weights data points according to variance. Points with less variance are assigned more weight and points with more variance are given less weight [23]. The same idea was applied to transmissions by incorporating weighted least squares in the pseudoinversion process. The weighting matrix, $\boldsymbol{W}$, a diagonal matrix of weight values, modified the conjugate transpose matrix $\boldsymbol{H}^*$. Since values in $\boldsymbol{W}$ needed to weight

individual transmissions, the dimensions of $\boldsymbol{W}$ were [n x n], given n transmissions. The final expression for the pseudoinverse, $\boldsymbol{H}^{\dagger}$, is given in Equation 2.2.

$$\boldsymbol{H}^{\dagger} = (\boldsymbol{H}^{*}\boldsymbol{W}\boldsymbol{H} + \boldsymbol{\Gamma}^{*}\boldsymbol{\Gamma})^{-1}\boldsymbol{H}^{*}\boldsymbol{W} \tag{2.2}$$

The default weighting for a transmission was **1**. If a transmission was weighted to **0** then it would not contribute to the final image. Transmissions did not need to be weighted between **0** and **1**, however; transmissions with weights larger than **1** influenced the final image more strongly than other transmissions. This behavior was confirmed by simulating plane and focused wave sequences of a point target moving 1 mm axially. This amount of motion corresponded to an observed velocity of 6.7 cm/s, enough to degrade an image if observed axially (Table 2.1). A control image beamformed with only plane transmissions was compared to an image generated from 100 plane transmissions weighted to **1** and 100 focused transmissions weighted to **0**. The delay matrices of both images were plotted to verify that the final images were the product of different data sets. Before designing a more robust weighting scheme for a simulated speckle phantom, the mixed sequence "middle 10 plane transmissions replaced by focused" was used to image the same point target moving 1 mm axially. The following weights were applied: plane transmissions at **0.5** and focused transmissions at **3**. Once again, the delay matrix for this mixed sequence was plotted. The resulting PSF served as guidance for future weighting schemes.

To better characterize the efficacy of applying weighted least squares, each of the mixed sequence cases presented in Section 2.4.2 were repeated with plane transmissions weighted at **0.5** and focused transmissions weighted at **3**. The same quantifications were then applied such that contour plots, CR curves, and cystic resolution values were available for all mixing cases in both weighted and unweighted contexts. Plotting cystic resolution values as pairs on a bar chart illustrated the effects induced by weighting and also compared each case to the controls of purely plane waves or purely focused waves.

2.4.4 Speckle Phantom - Weighted Mixed Sequences - Image Uniformity

Ultrasound scans of an ATS 539 multipurpose imaging phantom (CIRS, Norfolk, VA) were taken with the Verasonics Vantage 256 Research Scanner, combined in Matlab per Section 2.4.1, and beamformed with REFoCUS. The Verasonics P4-2V was held in place during image acquisition, transmit voltage was set to 5 V, and each acquisition involved 121 transmissions. The primary goal of this experiment was to determine if weighting mixed sequences had a significant impact on image uniformity. Previous experiments evaluated the ways in which weighted, mixed sequences may better resolve motion, but mixed sequences also needed to resolve stationary tissue across the entire field of view.

Cyst targets were imaged with the focal depth set to 60 mm for the focused transmissions. After beamforming with REFoCUS, the resulting control images were the unweighted swept plane wave sequence and swept focused wave sequence. Six mixture cases of interest were chosen: the middle 20 focused transmissions added to the full plane sequence, the middle 20 focused transmissions replacing plane transmissions, full combination, the middle 30 focused transmissions replacing plane transmissions, every fourth focused transmission added to the full plane sequence, and every fourth focused transmission replacing corresponding plane transmissions. The same weighting scheme was applied as before.

The resultant images of a phantom, rather than a single point target, illustrated the effects of mixed sequences away from the focus or on the edges of a scan. Delay matrices were also plotted to ensure that transmissions were added or replaced correctly. Since image uniformity is relatively subjective, no quantifications were applied to the phantom images.

Chapter 3

Results

3.1 Motion Sensitivity - Virtual Source vs. REFoCUS

3.1.1 Moving Point Target - Simulation

First, results are presented from the Field II simulation evaluating lateral and axial motion sensitivity in the context of virtual source and REFoCUS beamforming. This test also considered three transmit waveforms: plane waves, focused waves, and off-focus (target located 10 mm below the focus). The contour plots of the resultant PSF when imaging **lateral** motion with plane waves are shown in Figure 3.1. Even though ten motion cases were imaged, including stationary, three representative contour plots are shown for both virtual source (left) and REFoCUS (right). The way in which the shape of the PSF changes as velocity increases is consistent, so the three contour plots shown are from the stationary case, the 3 mm/frame case, and the 10 mm/frame motion case in order to represent how each PSF changes as velocity increases. The three cases correspond to observed velocities of 0, 20.1, and 66.8 cm/s (Table 2.1). In this way, the lowest and highest amounts of motion are shown, as well as an intermediate case. Notice that as the point target moves faster, from left to right, energy is more dispersed and side lobes are more significant and curve upwards. Virtual source and REFoCUS beamforming perform very comparably: slightly longer side lobes can be observed with REFoCUS, but axial ringing is reduced. Overall, the location of the central energy in each PSF is similar for both beamforming techniques.

Next, Figure 3.2 shows the PSFs from the same amounts of lateral motion, imaged with

focused waves. Here, the PSF is largely unaffected as velocity increases. The primary difference between virtual source and REFoCUS beamforming, here, is the texture of the side lobes. The texture observed in the virtual source case is a product of the aggressive masking implemented during beamforming. REFoCUS, which does not rely on spatial masks, produces a PSF with similarly size, smooth side lobes. Regardless of beamforming method, focused waves show potential to maintain high resolution in the presence of lateral motion.

With the same three lateral motion cases, PSFs from the off-focus case are shown in Figure 3.3. As expected, the behavior of the PSF in the off-focus case is between that of plane and focused waves. More lateral degradation and side lobe production is observed as velocity increases, but not to same extent as when imaging with plane waves. Interestingly, side lobes bend away from the transducer in this case, which is the opposite behavior of plane waves. Some differences in side lobe shape are evident here. Once again, these differences are likely the produce of the spatial mask used during virtual source beamforming. Consider the hourglass shape of the mask applied for focused waves. Side lobes on the top of a PSF from a point target located below the focus are going to be closer to the mask, so they are going to be affected more than side lobes below the PSF. Note that this does not explain the direction of side lobe curvature, just the difference in side lobe *shape* across virtual source and REFoCUS beamforming. These results suggest that even though focused waves do not resolve motion away from the focus as well as they do at the focus, they still show potential to resolve lateral motion better than plane waves.

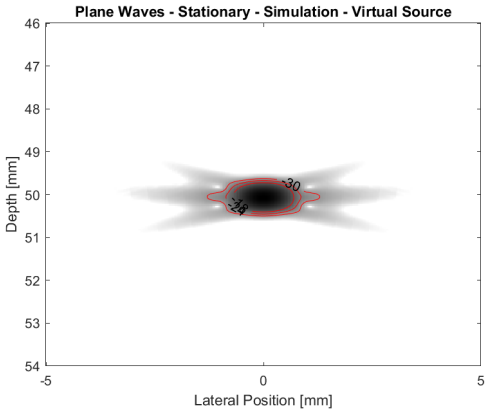

(a) Stationary - VS

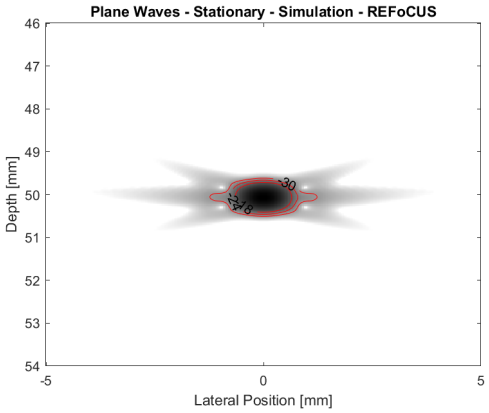

(b) Stationary - REFoCUS

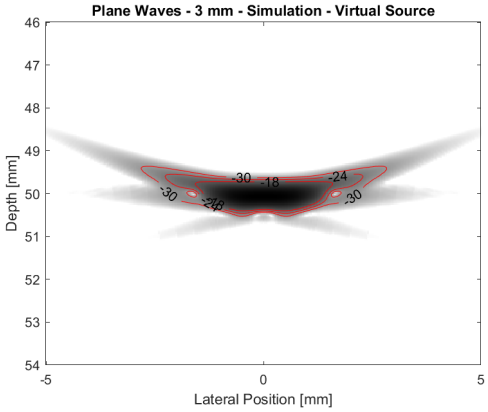

(c) 3 mm/frame - VS

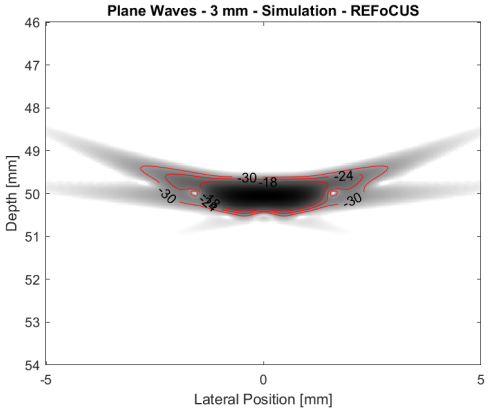

(d) 3 mm/frame - REFoCUS

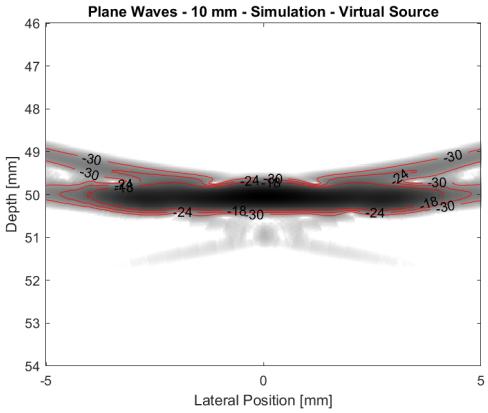

(e) 10 mm/frame - VS

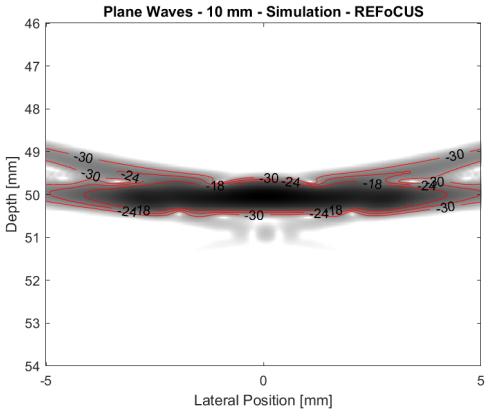

(f) 10 mm/frame - REFoCUS

Figure 3.1: Simulation - Lateral Motion (LR) - Plane Waves - PSFs

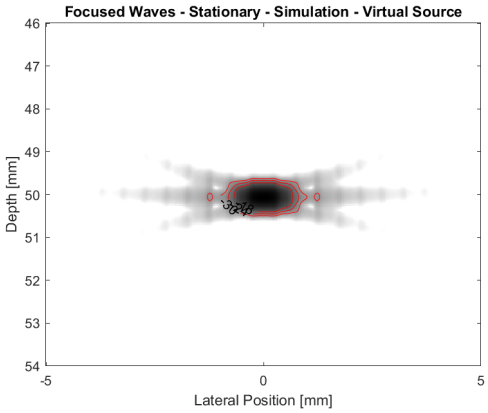

(a) Stationary - VS

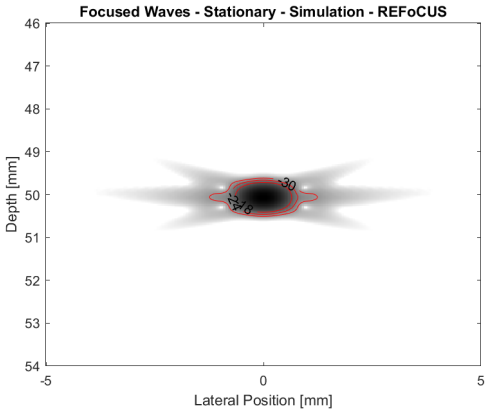

(b) Stationary - REFoCUS

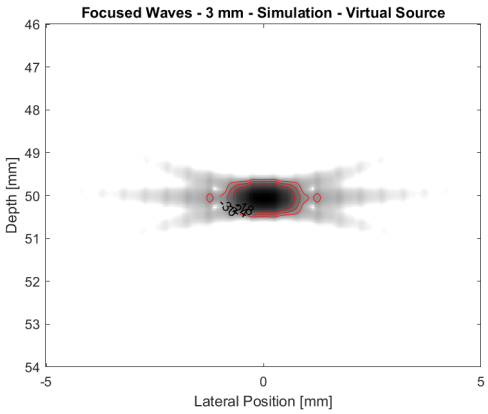

(c) 3 mm/frame - VS

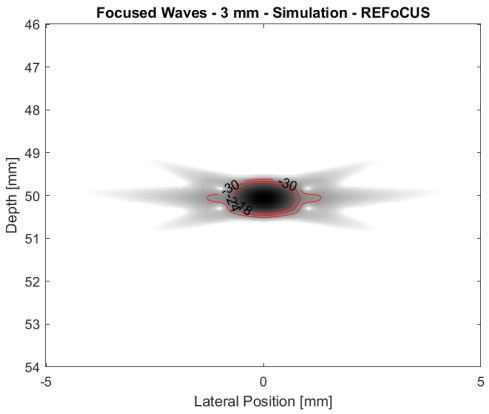

(d) 3 mm/frame - REFoCUS

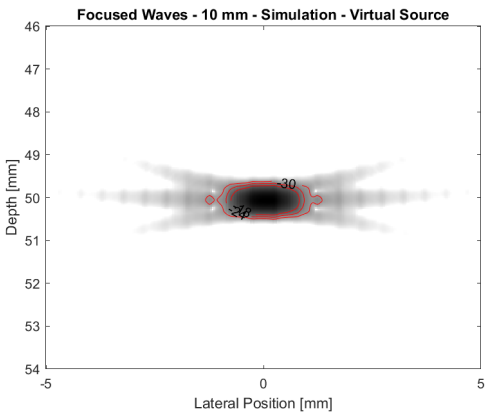

(e) 10 mm/frame - VS

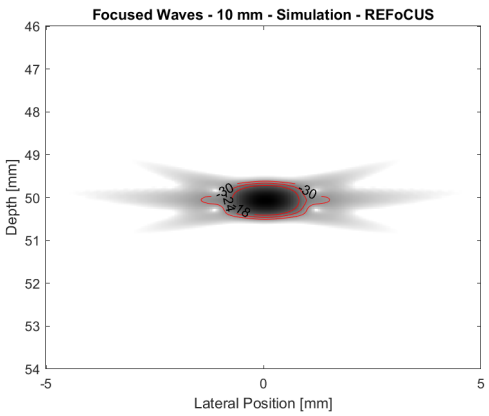

(f) 10 mm/frame - REFoCUS

Figure 3.2: Simulation - Lateral Motion (LR) - Focused Waves - PSFs

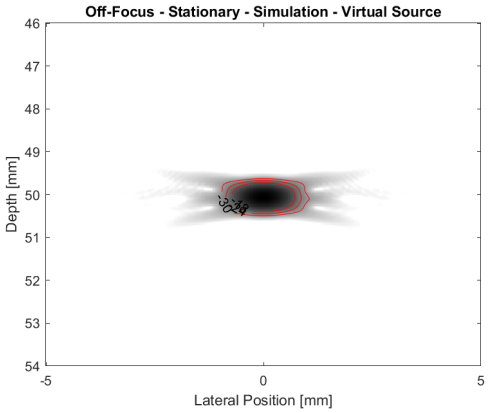

(a) Stationary - VS

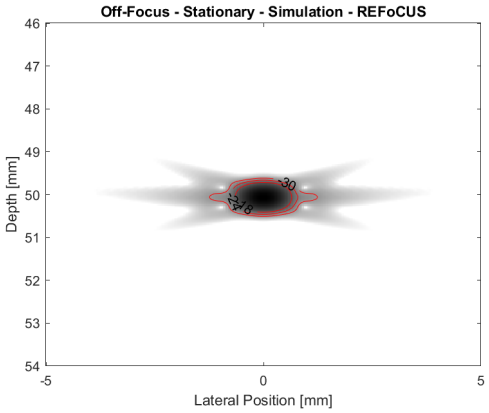

(b) Stationary - REFoCUS

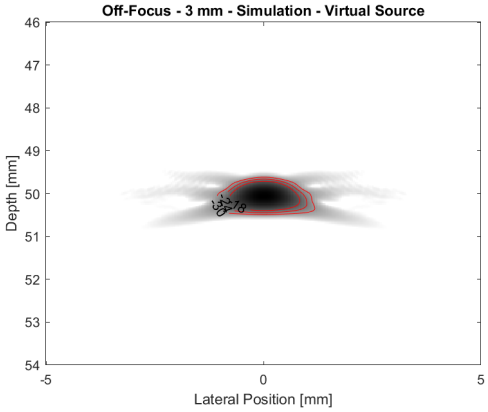

(c) 3 mm/frame - VS

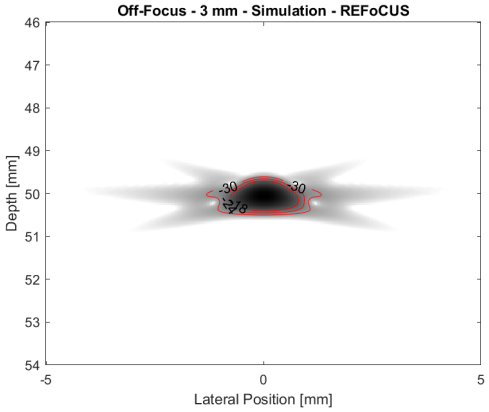

(d) 3 mm/frame - REFoCUS

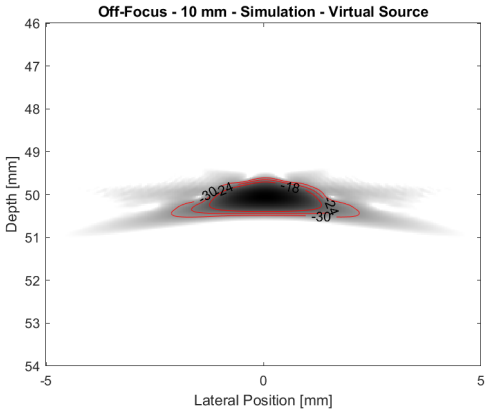

(e) 10 mm/frame - VS

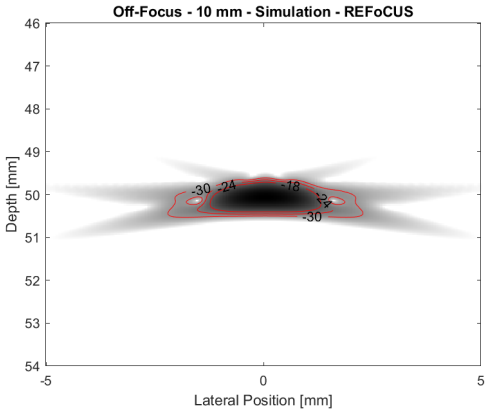

(f) 10 mm/frame - REFoCUS

Figure 3.3: Simulation - Lateral Motion (LR) - Off-Focus - PSFs

After considering the contour plots from key lateral motion cases, cystic contrast vs. radius curves (CR curves) are shown. Figure 3.4 gives the CR curves for all lateral motion cases imaged with plane waves for (a) virtual source and (b) REFoCUS beamforming. Recall that cystic contrast measures the amount of energy contained within a ROI relative to the amount of total energy in an image; the x-axis of a CR curve represents the radius of that ROI. A CR curve that drops more quickly corresponds to a PSF with more centralized energy. Also plotted on these figures is a blue dotted line at - 20 dB. The radius at which a CR curve crosses this dotted line describes the size of a cyst that would be detectable at a level of -20 dB. This metric is known as cystic resolution and is calculated for every curve. Here, CR curves become less steep as lateral motion increases. Regions of a CR curve that become suddenly steeper (such as the 10 mm/frame CR curve on the top right of both sub-figures) may indicate that side lobes or axial ringing begin at that radius from the center of the PSF. These plots are particularly useful for comparing virtual source and REFoCUS beamforming. While the shapes of the curves are largely similar, REFoCUS beamforming shows lower contrast values at a radius of 4 mm. This may suggest that more side lobes are present with REFoCUS, or simply that energy is distributed more laterally than axially, since the lateral side lobes are larger than 4 mm in the larger motion cases, whereas axial ringing is generally smaller.

Figure 3.5 shows the CR curves for all lateral motion cases imaged with focused waves. As anticipated, all CR curves are tightly grouped and show the same overall shape. These similarities confirm the notion that focused waves may be able to better resolve lateral motion. The slight "bump" in each CR curve around 1.2 mm likely corresponds to the transition from main lobe to side lobe in the PSF. Once again, virtual source and REFoCUS beamforming exhibit the same performance. This consistency lends credence to the argument that REFoCUS is a viable beamforming method, even in the presence of motion.

As an intermediate between plane and focused waves, CR curves from the off-focus case are shown (Figure 3.6). These CR curves, once again, confirm observations from the off-focus contour plots. CR curves are more spread out (as velocity increases) than the focused case, but less spread

out than the plane wave case. The "bump" in each CR curve is still visible when beamforming with REFoCUS. The lack of a "bump" with virtual source may correspond to the reduced side lobes from being near to the edges of the hourglass shaped mask, matching the focused case. The difference in contrast at 4 mm is also observed, which matches the plane wave case. Overall, these CR curves confirm that focused waves perform the best at the focus and begin to behave like plane waves away from the focus.

Cystic resolution was determined for every motion case as a final metric for the efficacy of each imaging sequence and beamforming method in the presence of motion. Cystic resolution as a function of lateral movement/frame is are plotted in Figure 3.7 for all three imaging sequences and for both virtual source (blue) and REFoCUS (red) beamforming. This plot provides final confirmation that focused sequence are least sensitive to motion, followed closely by focused waves away from the focus, followed by plane waves. These results also show that virtual source and REFoCUS beamforming perform comparably, particularly in the focused and off-focus cases. The two beamforming methods even perform similarly for plane waves, with the exception of significant observed velocity. According to Table 2.1, movements of 7.5 mm/frame correspond to an observed velocity of 50.1 mm/frame, which is above velocities exhibited *in-vivo*. In total, the results from both beamforming methods match quite well.

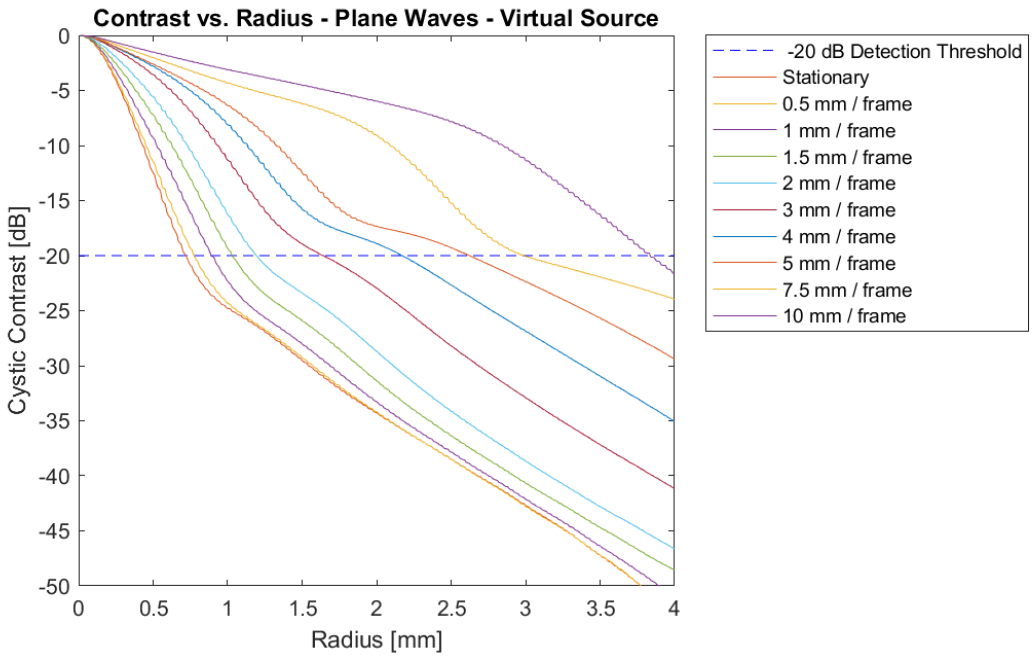

(a) Cystic Contrast vs. Radius - CR Curve - Virtual Source

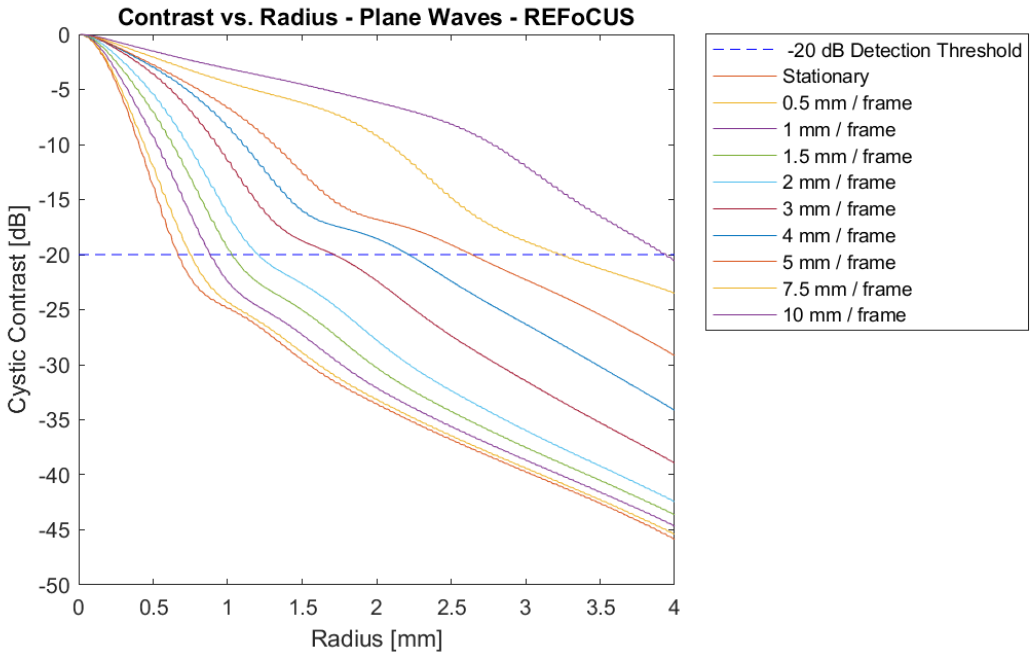

(b) Cystic Contrast vs. Radius - CR Curve - REFoCUS

Figure 3.4: Simulation - Lateral Motion (LR) - Plane Waves - CR Curves

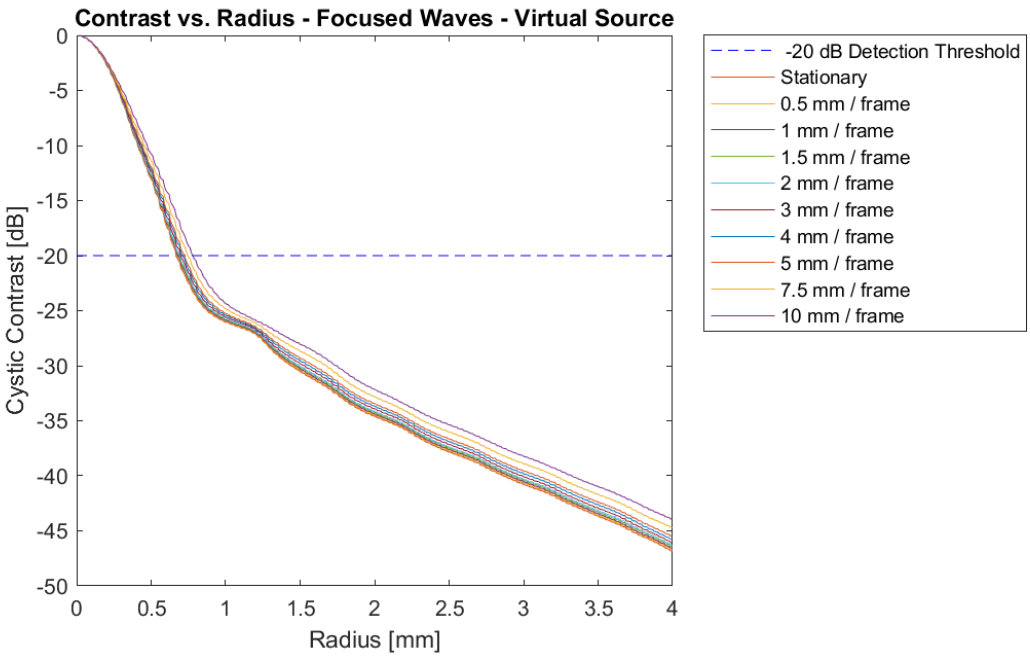

(a) Cystic Contrast vs. Radius - CR Curve - Virtual Source

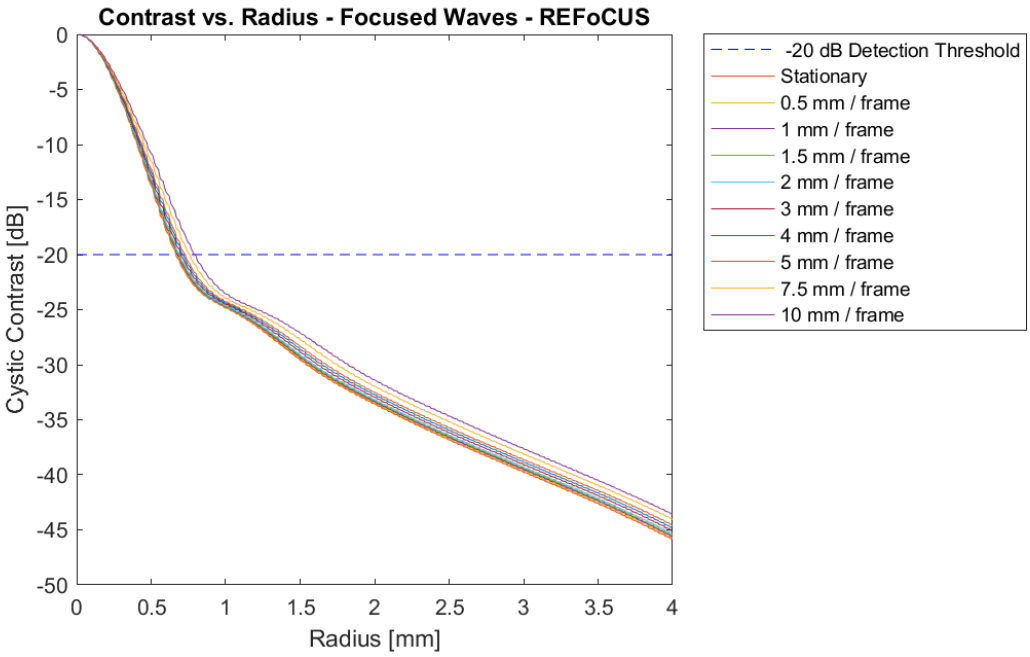

(b) Cystic Contrast vs. Radius - CR Curve - REFoCUS

Figure 3.5: Simulation - Lateral Motion (LR) - Focused Waves - CR Curves

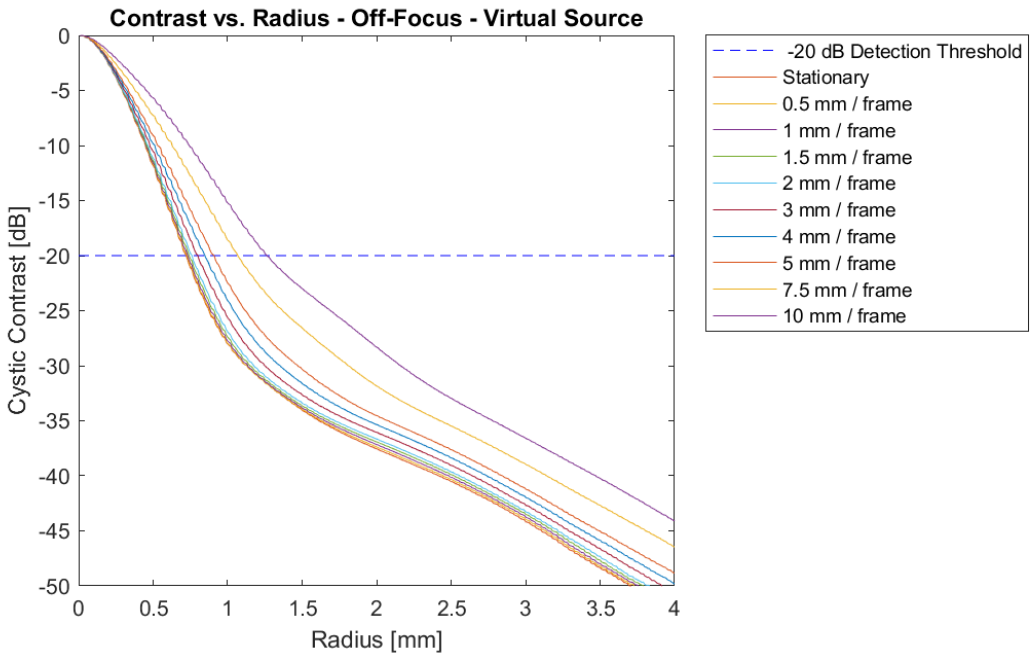

(a) Cystic Contrast vs. Radius - CR Curve - Virtual Source

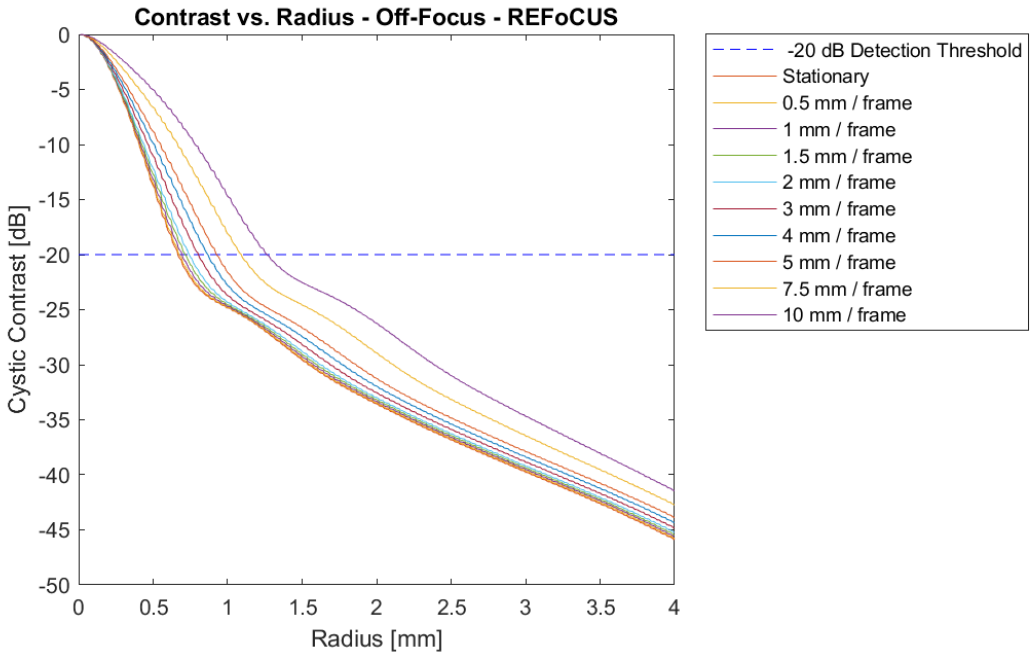

(b) Cystic Contrast vs. Radius - CR Curve - REFoCUS

Figure 3.6: Simulation - Lateral Motion (LR) - Off-Focus - CR Curves

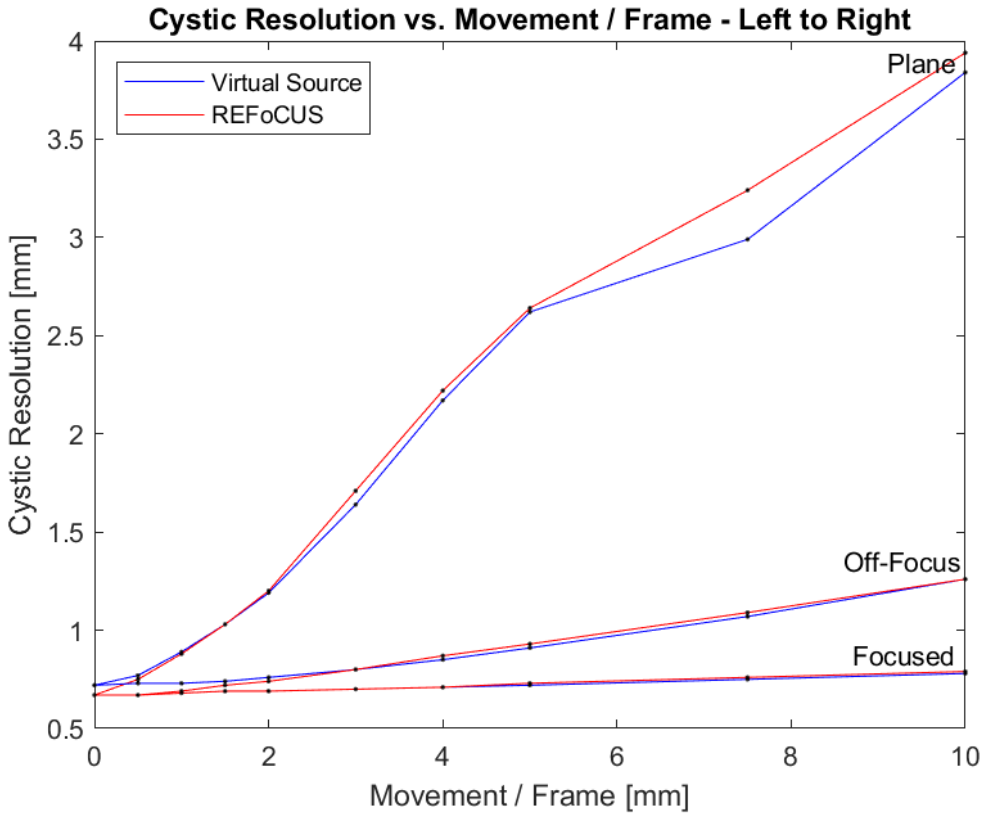

Figure 3.7: Simulation - Lateral Motion - Cystic Resolution vs. Movement/Frame - Initial Direction (LR)

Since ultrasound is more sensitive to axial motion than lateral motion, contour plots, CR curves, and cystic resolution plots are also produced for axial motion. The contour plots of PSFs from three motion cases are shown for plane waves, focused waves, and the off-focus case in Figure 3.8, Figure 3.9, and Figure 3.10, respectively. The three motion cases shown are stationary, 0.5 mm/frame, and 1.5 mm/frame, representing the a target imaged with no motion, an intermediate amount of motion, and a significant amount of motion. These axial motions correspond to 0, 3.3, and 10 cm/s (Table 2.1). Figure 3.8 illustrates interesting behavior: axial motion produces lateral degradation. This phenomenon has been previously reported [36], and these results match. As axial velocity from "down" to "up" increases, the PSF has more lateral degradation to the left. Axial motions of as little as 1.5 mm/frame (10 cm/s, Table 2.1) produce drastic side lobes, and even

begin to distribute large amounts of energy away from the center of the PSF. Again, REFoCUS produces slightly more pronounced side lobes, but the central energy of each PSF is highly similar.

The trends in the focused case match the lateral motion tests. As shown in Figure 3.9, each PSF remains largely unchanged as point target velocity increases. Similarly to before, REFoCUS PSFs have smoother side lobes than those produced by virtual source, likely due to the narrow spatial mask near the focal point. In the off-focus case (Figure 3.10), axial motion affects the PSF less than lateral motion. Although the largest amount of motion does begin to degrade the PSF, each PSF remains largely intact as motion increases. Interestingly, whereas axial motion from down to up produced degradation to the left of the PSF when imaged with plane waves, axial motion from down to up produces degradation to the right of the PSF when imaged below the focal point of focused waves.

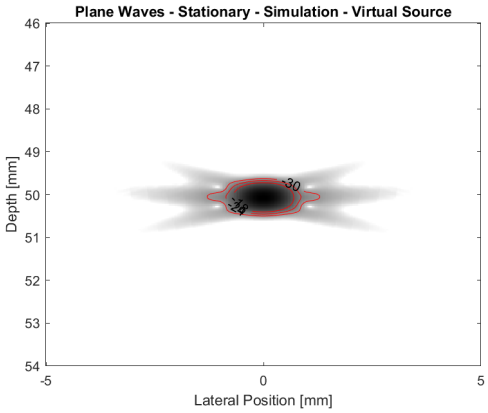

(a) Stationary - VS

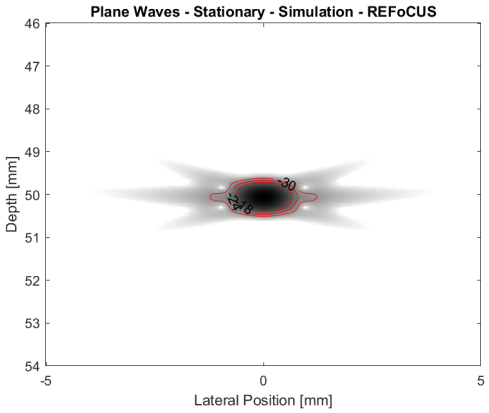

(b) Stationary - REFoCUS

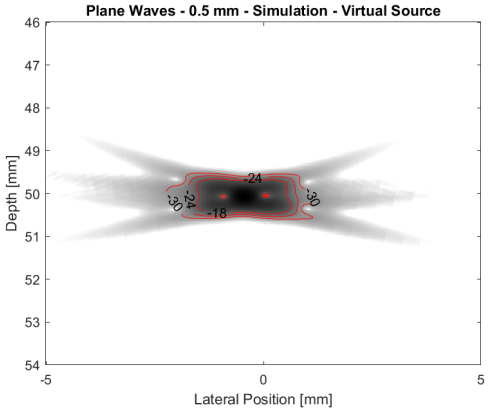

(c) 0.5 mm/frame - VS

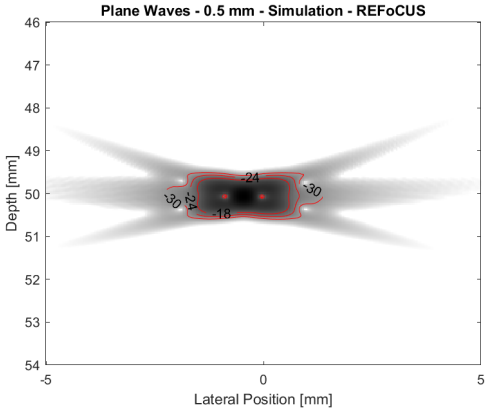

(d) 0.5 mm/frame - REFoCUS

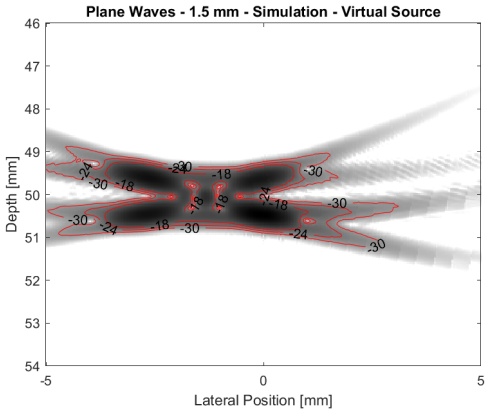

(e) 1.5 mm/frame - VS

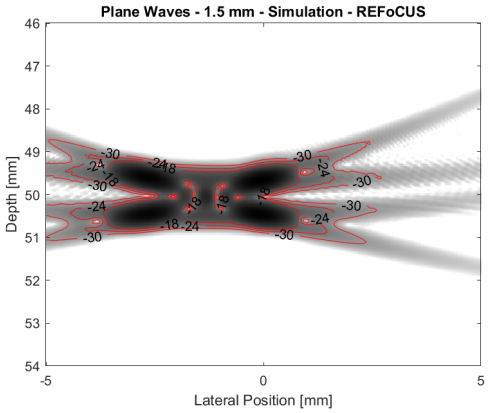

(f) 1.5 mm/frame - REFoCUS

Figure 3.8: Simulation - Axial Motion (DU) - Plane Waves - PSFs

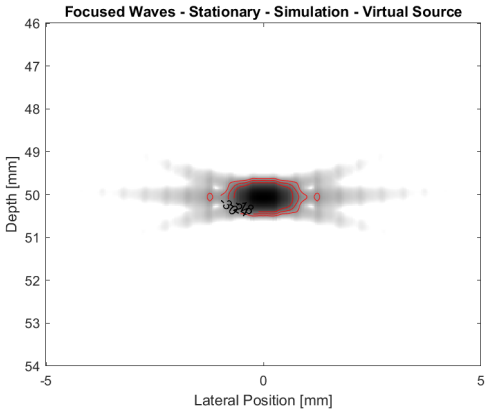

(a) Stationary - VS

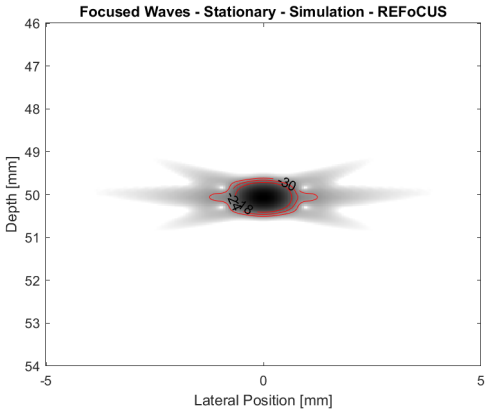

(b) Stationary - REFoCUS

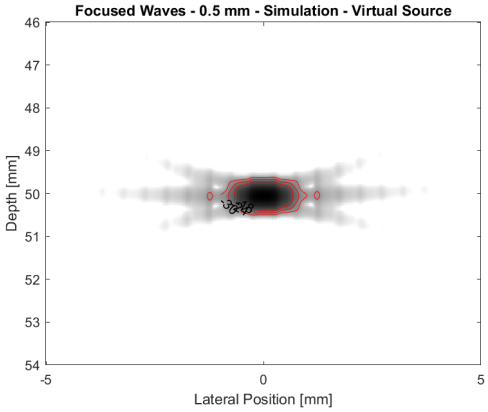

(c) 0.5 mm/frame - VS

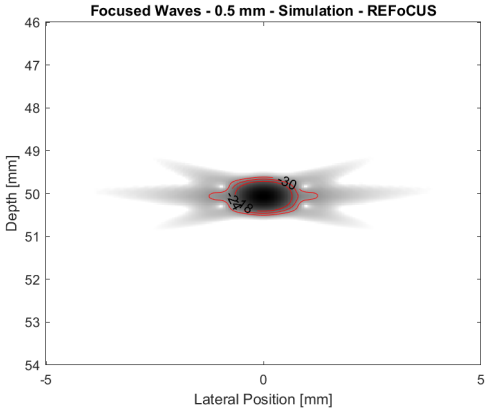

(d) 0.5 mm/frame - REFoCUS

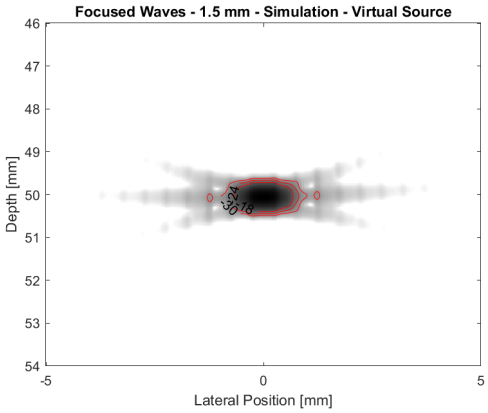

(e) 1.5 mm/frame - VS

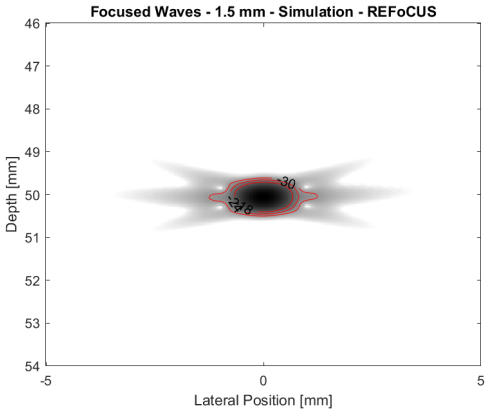

(f) 1.5 mm/frame - REFoCUS

Figure 3.9: Simulation - Axial Motion (DU) - Focused Waves - PSFs

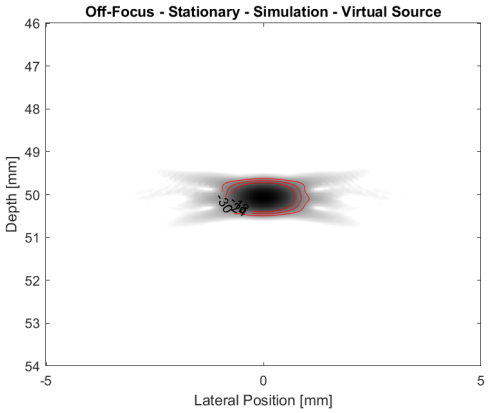

(a) Stationary - VS

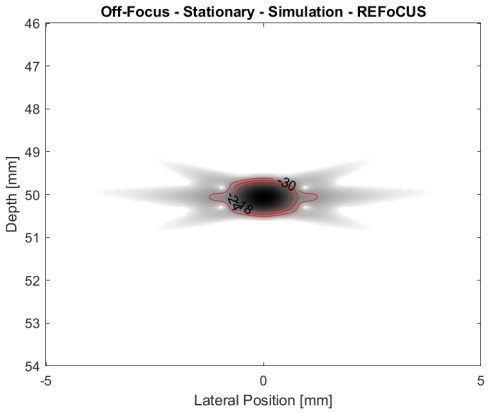

(b) Stationary - REFoCUS

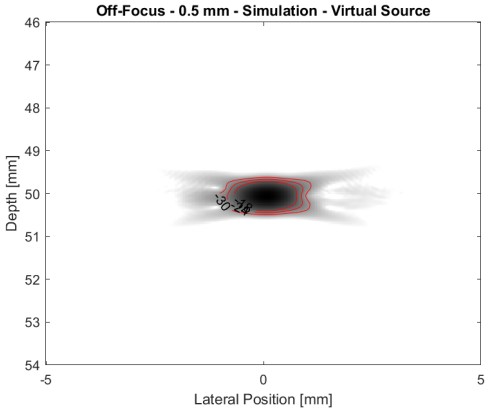

(c) 0.5 mm/frame - VS

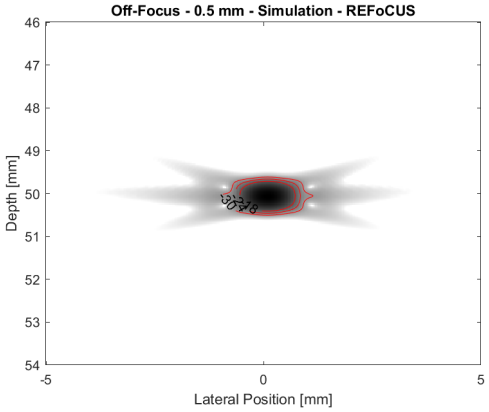

(d) 0.5 mm/frame - REFoCUS

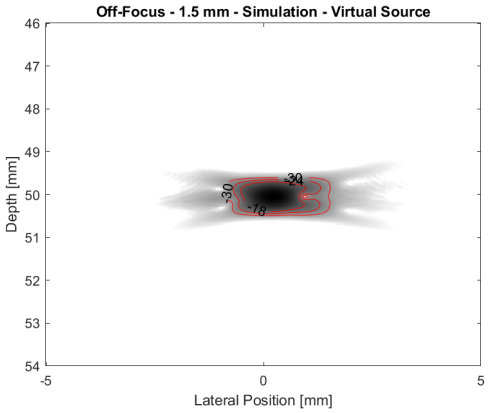

(e) 1.5 mm/frame - VS

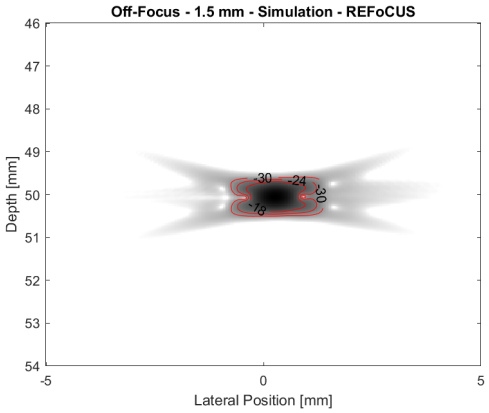

(f) 1.5 mm/frame - REFoCUS

Figure 3.10: Simulation - Axial Motion (DU) - Off-Focus - PSFs

Cystic contrast vs. radius curves (CR curves) are also developed for every axial motion case. The CR curves for axial motion imaged with plane waves are shown in Figure 3.11. Again, CR curves become less steep as velocity increases. In fact, some curves corresponding to higher velocities remain above -5 dB for several mm, suggesting that the PSF has become very enlarged and the energy has become quite dispersed. The shape of each curve also remains fairly consistent across beamforming methods. As in the case of lateral motion, virtual source offers slight improvements in contrast at radii of 4 mm, implying that REFoCUS has slightly more significant side lobes. Despite having lower contrast values, however, REFoCUS CR curves are more tightly packed in the 0-0.3 mm/frame movement cases than virtual source. This consistency suggests that REFoCUS may perform more consistently than virtual source in the presence of small axial motions.

The CR curves for axial motion imaged with focused waves are very telling (Figure 3.12). The CR curves for all motion cases, beamformed with virtual source, are identical. The reason for this extreme consistency is likely that a focused sequence sweeping from left to right will always insonify a point target moving from down to up at a very similar position. Moreover, thanks to the narrow mask used with focused waves, a focused transmission sequence will only "see" the target for a brief moment. The reason that all of these CR curves match is also the reason that focused waves are better able to resolve motion. Despite not implementing spatial masking, REFoCUS beamforming performs very similarly, suggesting that some kind of effective masking is taking place. In both the plane and focused case, small axial motion increments have slightly reduced contrast compared to the stationary target. This reduced contrast suggests that side lobes are reduced for small motion cases, but the reason for this remains unclear.

Lastly, Figure 3.13 shows the CR curves for axial motion imaged off-focus. Again, these CR curves exhibit characteristics from both the plane and focused CR curves. Generally speaking, the curves are more tightly grouped (matching focused) but do begin to spread out as velocity increases and do show a decrease in contrast at 4 mm with REFoCUS (matching plane). While CR curves can be difficult to interpret, cystic resolution is much easier to understand. Cystic resolution is plotted as a function of axial movement per frame in Figure 3.14. This figure shows that virtual source

and REFoCUS behave the same in the presence of axial motion. Even though the differences are quite small, cystic contrast is smaller (improved) for nearly every motion case when beamforming with REFoCUS. Further inferences are that plane waves resolve axial motion poorly, while focused waves resolve axial motion well.

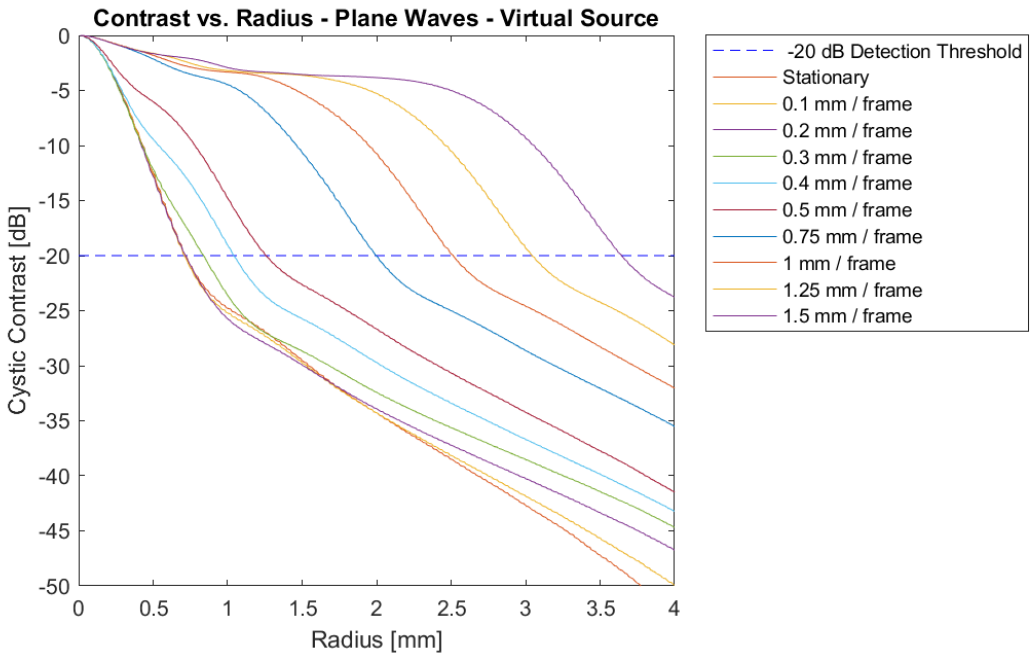

(a) Cystic Contrast vs. Radius - CR Curve - Virtual Source

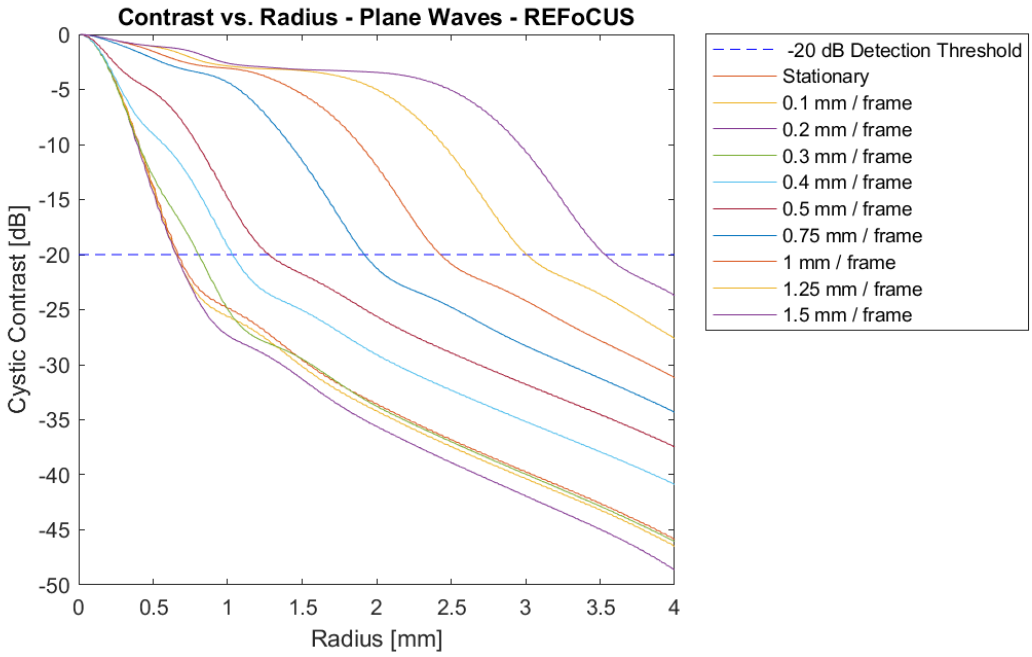

(b) Cystic Contrast vs. Radius - CR Curve - REFoCUS

Figure 3.11: Simulation - Axial Motion (DU) - Plane Waves - CR Curves

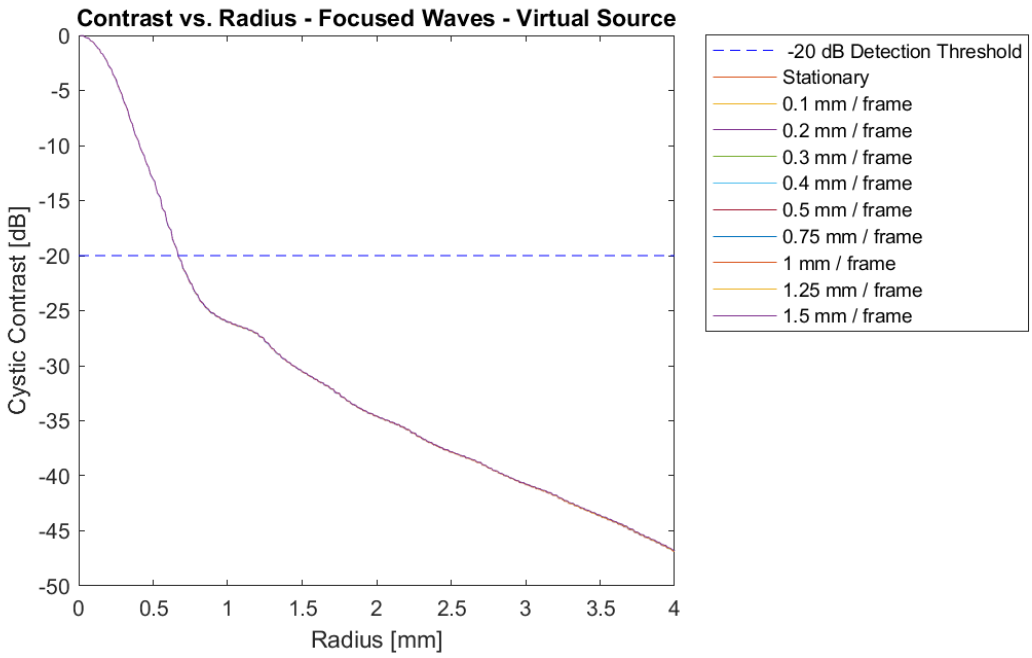

(a) Cystic Contrast vs. Radius - CR Curve - Virtual Source

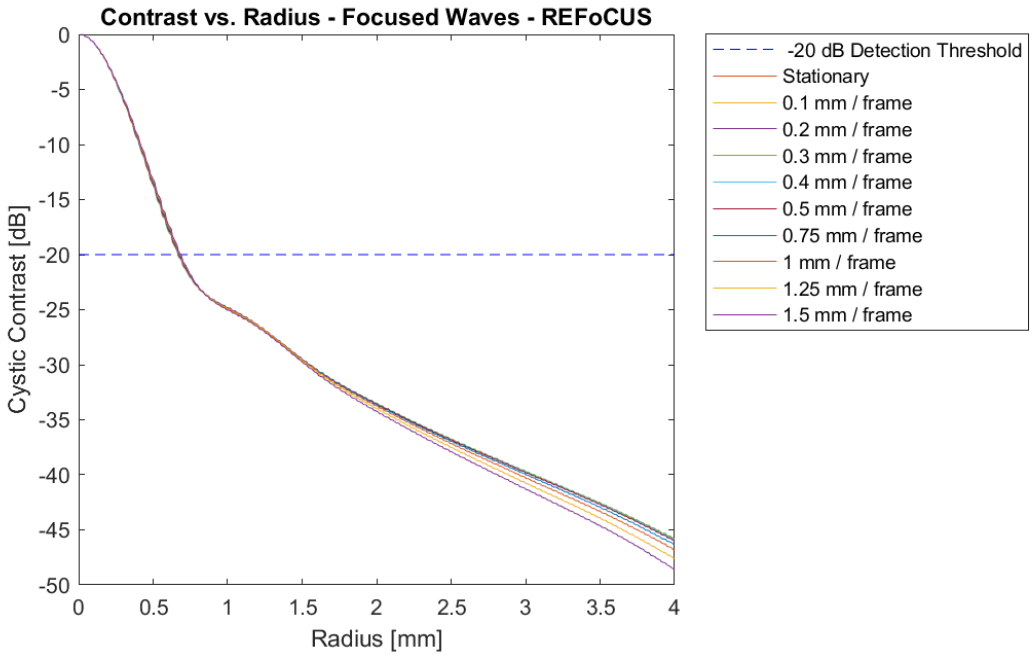

(b) Cystic Contrast vs. Radius - CR Curve - REFoCUS

Figure 3.12: Simulation - Axial Motion (DU) - Focused Waves - CR Curves

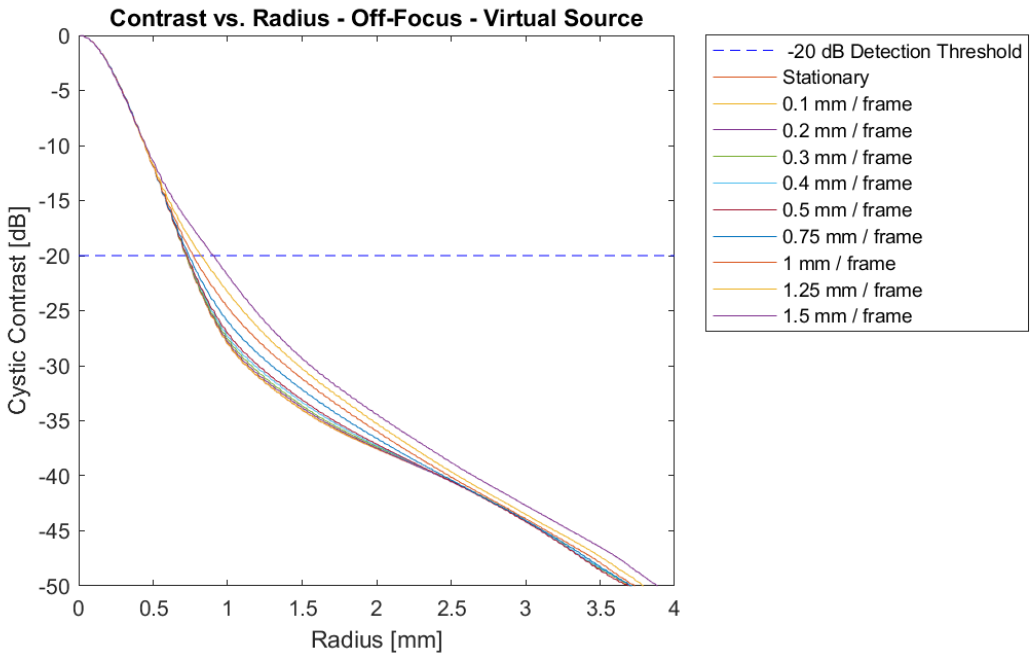

(a) Cystic Contrast vs. Radius - CR Curve - Virtual Source

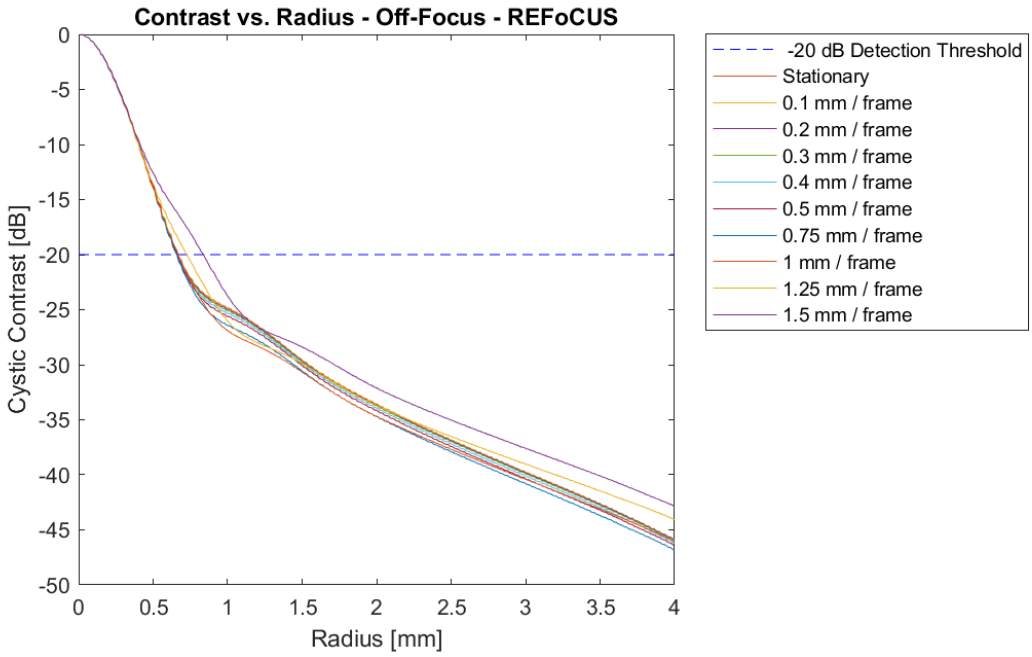

(b) Cystic Contrast vs. Radius - CR Curve - REFoCUS

Figure 3.13: Simulation - Axial Motion (DU) - Off-Focus - CR Curves

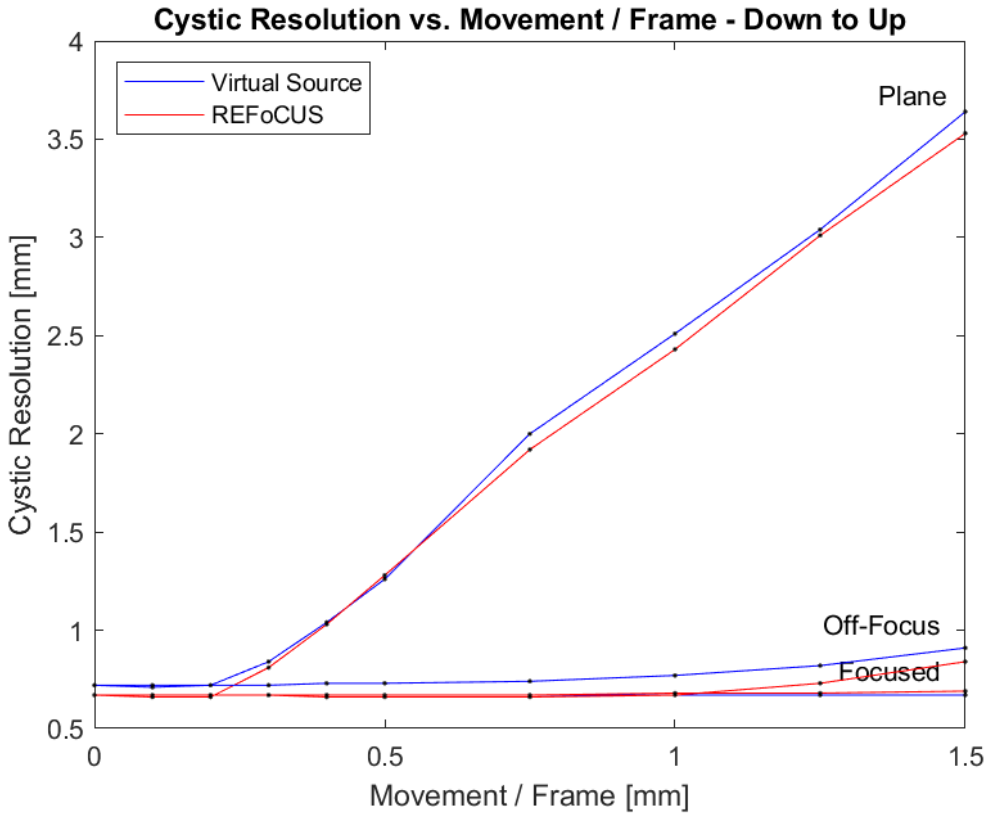

Figure 3.14: Simulation - Axial Motion - Cystic Resolution vs. Movement/Frame - Initial Direction (DU)

3.1.2 Moving Point Target - Simulation - Opposite Direction

Since ultrasound scans both in Field II and on the Verasonics were taken from left to right, when viewing the final image, direction of motion relative to the direction of scan could potentially influence sensitivity to motion. Initial simulations of moving point targets were conducted with the target moving left to right, laterally, and down to up, axially. Identical simulations were run with one key change: right to left motion, laterally, and up to down motion, axially.

First, the PSFs and contour plots for right to left lateral motion are shown for plane waves (Figure 3.15), focused waves (Figure 3.16), and the off-focus case (Figure 3.17). The same three motion cases are shown: stationary, 3 mm/frame, and 10 mm/frame. The general trends observed

for initial direction simulations hold true for these opposite direction simulations. Lateral motion imaged with plane waves produced lateral degradation that increased with velocity (Figure 3.15). Virtual source and REFoCUS also performed largely the same, with REFoCUS showing slightly increased lobes above the PSF. Whereas left to right motion caused side lobes to curve towards the transducer, right to left motion produces side lobes that curve *away* from the transducer.

Imaging lateral motion in the opposite direction with focused waves produced nearly the same results as before (Figure 3.16). Since focused waves are less sensitive to motion, it makes sense that direction of motion would have less influence on PSFs produced by a focused sequence of transmissions. Once again, PSFs remain consistent in shape as velocity increases, with the only tangible difference being between the smoothness of side lobes produced by virtual source and REFoCUS. The off-focus contour plots, once again, combine the characteristics of plane and focused wave contour plots, as shown in Figure 3.17. Lateral degradation once again increases with velocity, but to a lesser extent than in the plane wave case. These side lobes, however, bend towards the transducer, which is the opposite behavior of the side lobes produced with plane waves. Crucially, the off-focus case remains less sensitive to motion than the plane waves, but more sensitive to motion than focused waves.

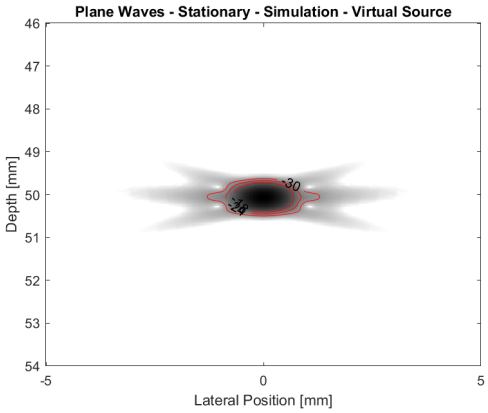

(a) Stationary - VS

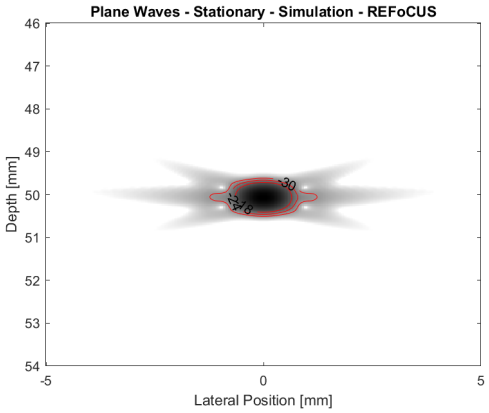

(b) Stationary - REFoCUS

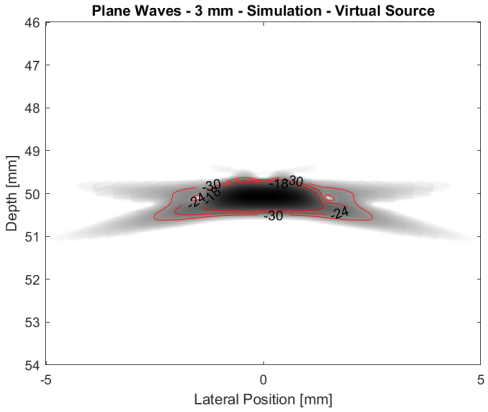

(c) 3 mm/frame - VS

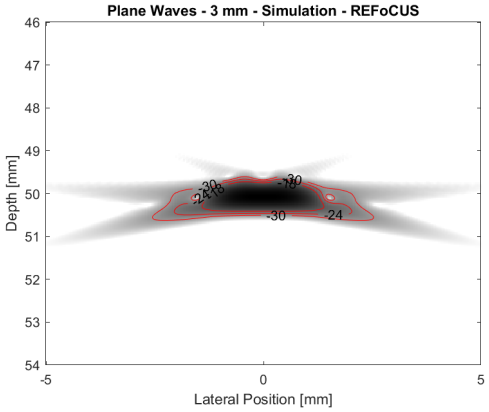

(d) 3 mm/frame - REFoCUS

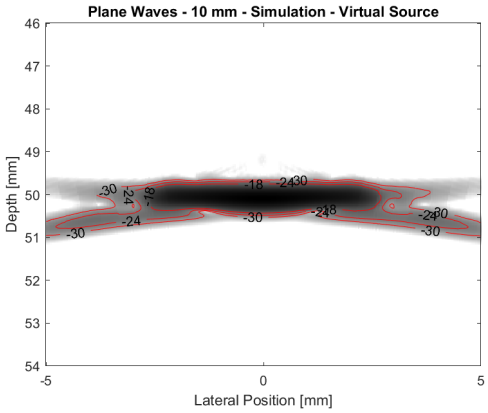

(e) 10 mm/frame - VS

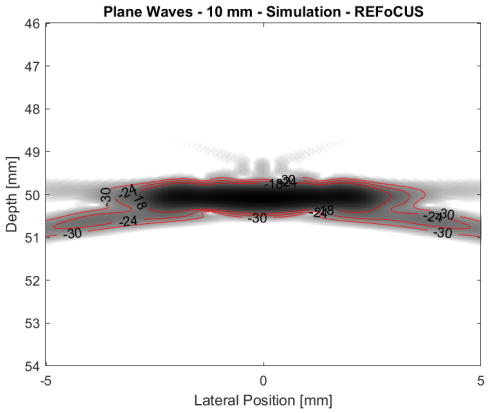

(f) 10 mm/frame - REFoCUS

Figure 3.15: Simulation - Opposite Lateral Motion (RL) - Plane Waves - PSFs

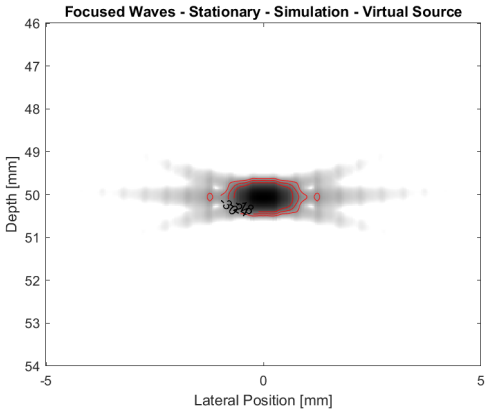

(a) Stationary - VS

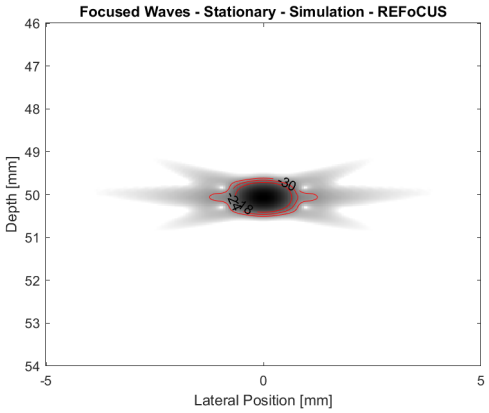

(b) Stationary - REFoCUS

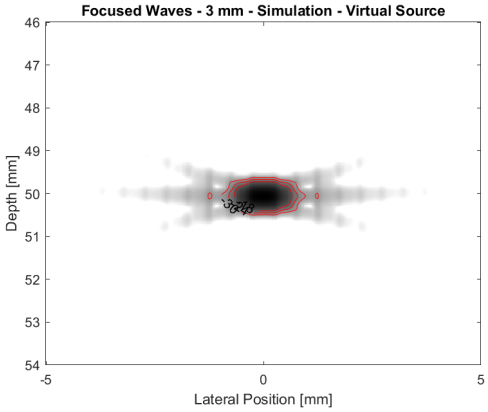

(c) 3 mm/frame - VS

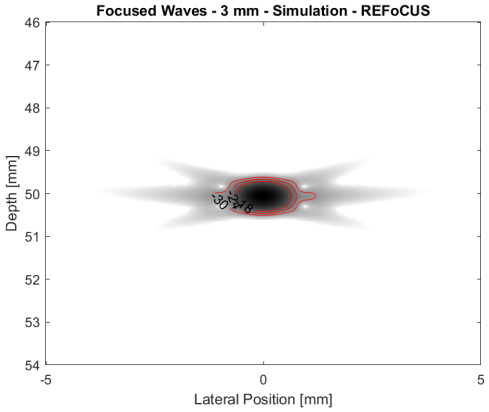

(d) 3 mm/frame - REFoCUS

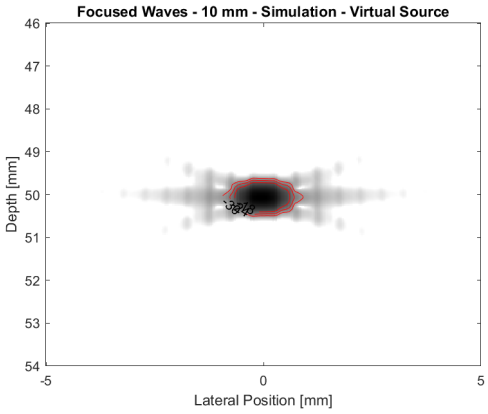

(e) 10 mm/frame - VS

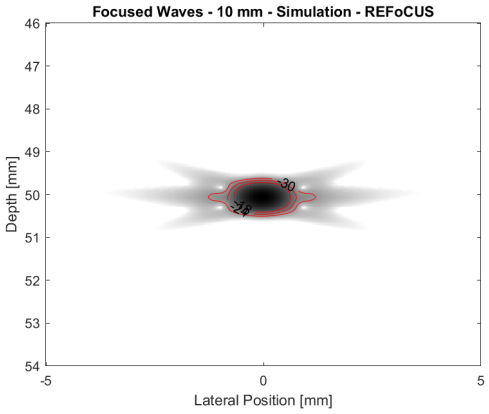

(f) 10 mm/frame - REFoCUS

Figure 3.16: Simulation - Opposite Lateral Motion (RL) - Focused Waves - PSFs

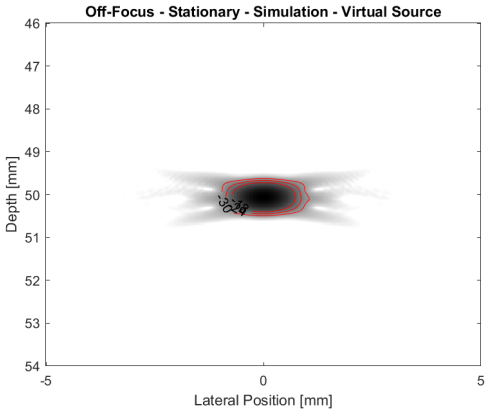

(a) Stationary - VS

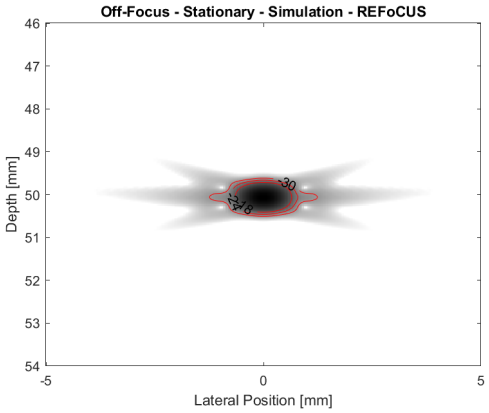

(b) Stationary - REFoCUS

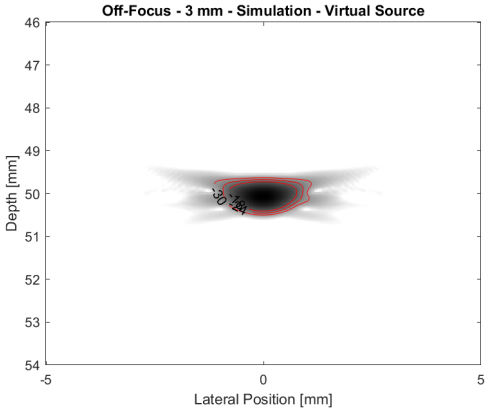

(c) 3 mm/frame - VS

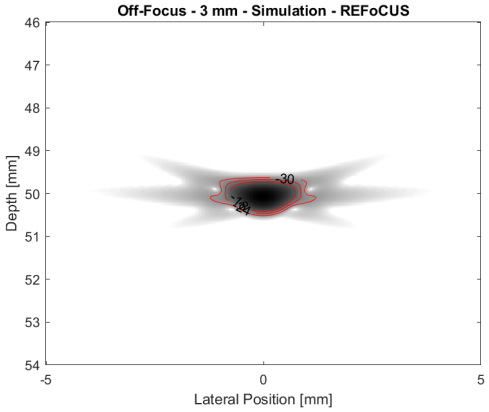

(d) 3 mm/frame - REFoCUS

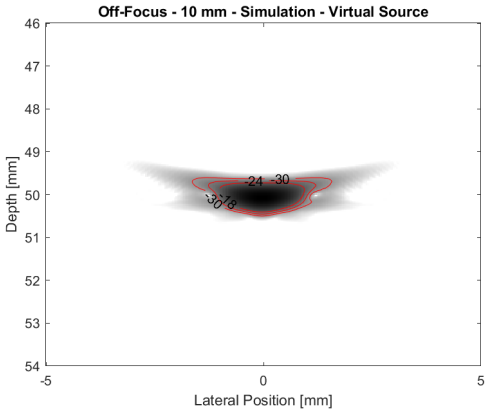

(e) 10 mm/frame - VS

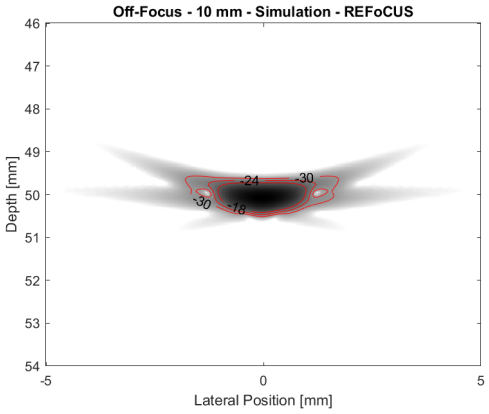

(f) 10 mm/frame - REFoCUS

Figure 3.17: Simulation - Opposite Lateral Motion (RL) - Off-Focus - PSFs

CR curves were developed from each contour plot for lateral motion from right to left and same trends observed when moving from left to right are observed. Figure 3.18 shows that plane waves are sensitive to increasing velocity and that REFoCUS, again, produces slightly reduced contrast at large radius values. Figure 3.19 shows the CR curves for all motion cases imaged with focused waves. It also confirms that focused waves are less sensitive to motion and that virtual source and REFoCUS beamforming perform comparable. Similarly, Figure 3.20 illustrates that imaging a point target away from the focal point of a focused transmission is less sensitive to motion than plane waves. That being said, these CR curves still possess a number of plane characteristics, such as reduced contrast at large radii when beamforming with REFoCUS.

Perhaps the most useful output from these CR curves is the cystic resolution value for each movement case. The cystic resolution values for right to left lateral motion are plotted in Figure 3.21b and are compared to cystic resolution from left to right lateral motion (Figure 3.21a). All values obtained from virtual source are plotted in blue and values obtained from REFoCUS are plotted in red. This figure confirms that focused waves are the least sensitive to motion, followed by off-focus and plane waves (in order). Note that cystic resolution values for focused waves are not influenced by direction of motion, but cystic resolution values for plane waves and off-focus targets are influenced by direction of motion; both of the latter two cases produce consistently lower cystic resolution values. This difference in resolution is the related to the amount of time the point target is insonified. When the scan and the point target are moving in opposite directions, the target is captured by fewer transmissions, meaning that fewer transmissions will have phase shifts caused by motion. Lastly, virtual source beamforming displays very slight improvements in resolution over REFoCUS in the focused and off-focus cases, which is likely tied to the extremely narrow spatial mask used during beamforming.

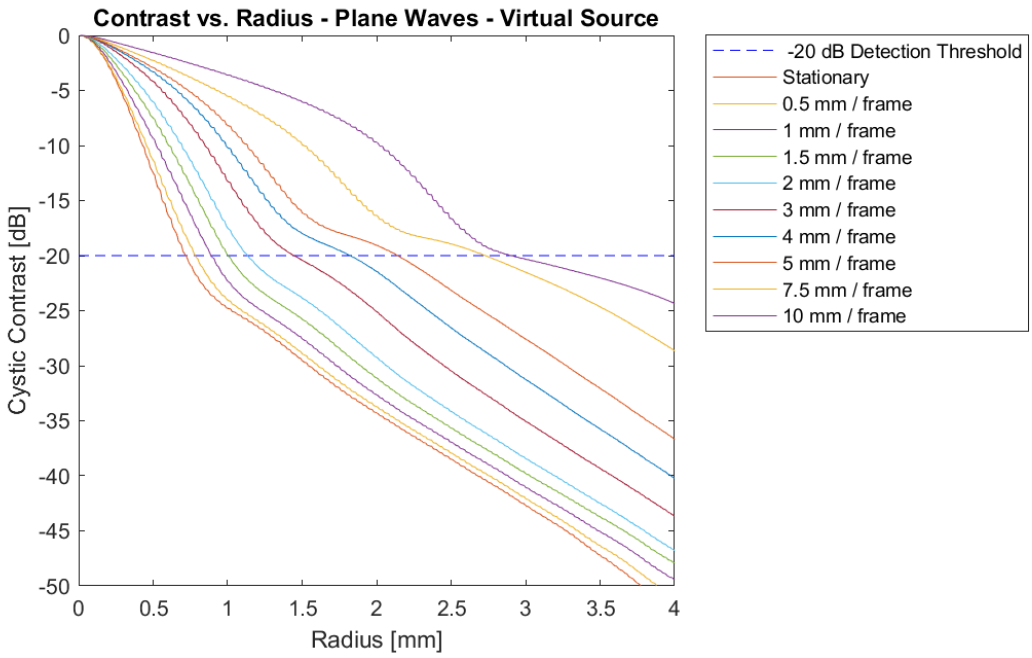

(a) Cystic Contrast vs. Radius - CR Curve - Virtual Source

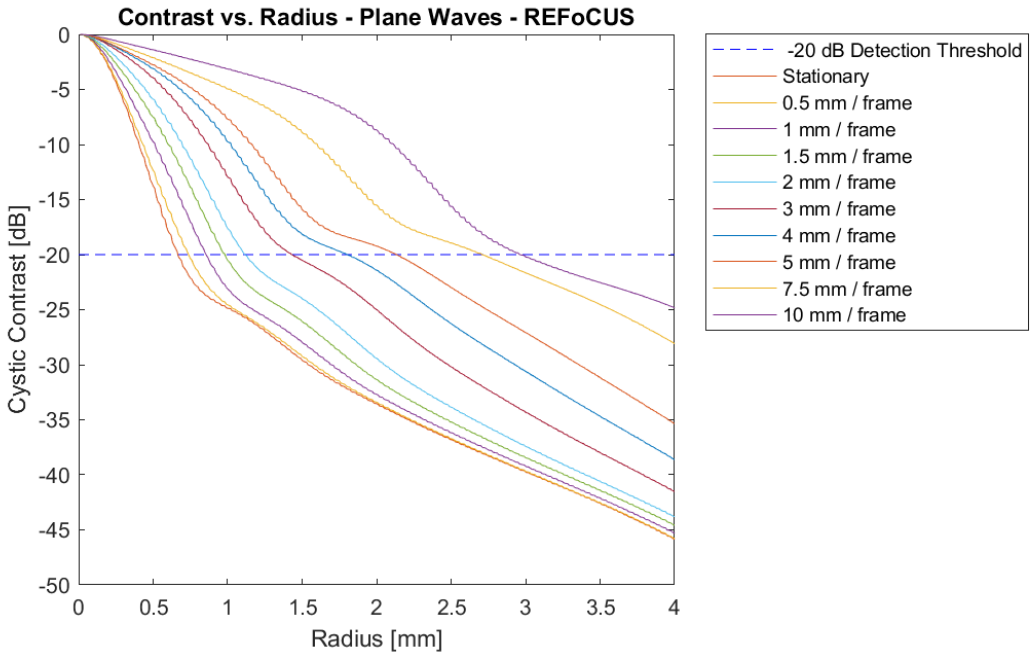

(b) Cystic Contrast vs. Radius - CR Curve - REFoCUS

Figure 3.18: Simulation - Opposite Lateral Motion (RL) - Plane Waves - CR Curves

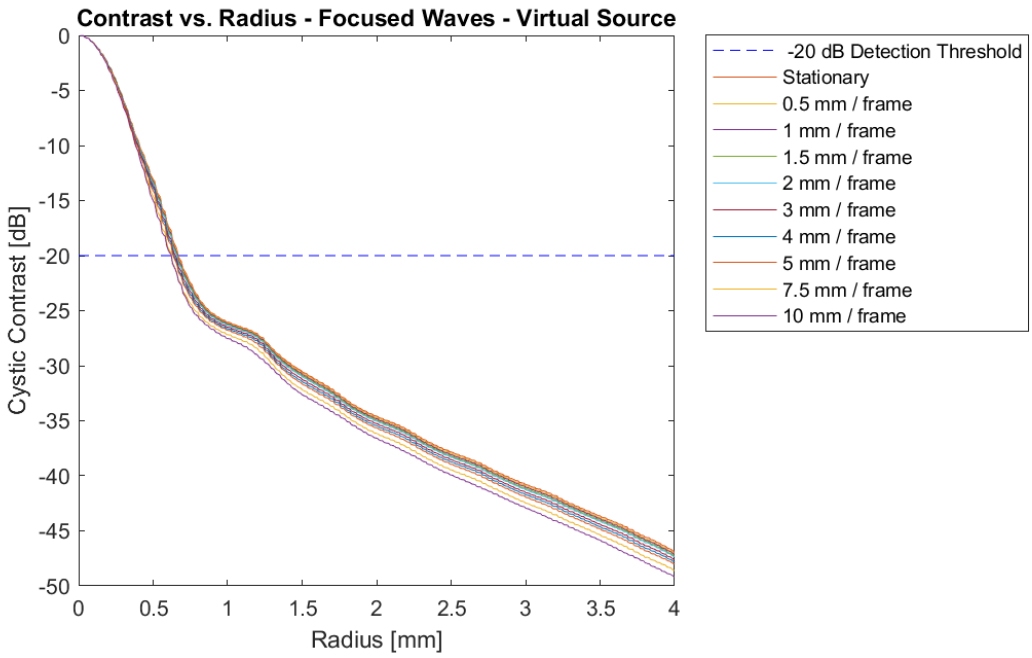

(a) Cystic Contrast vs. Radius - CR Curve - Virtual Source

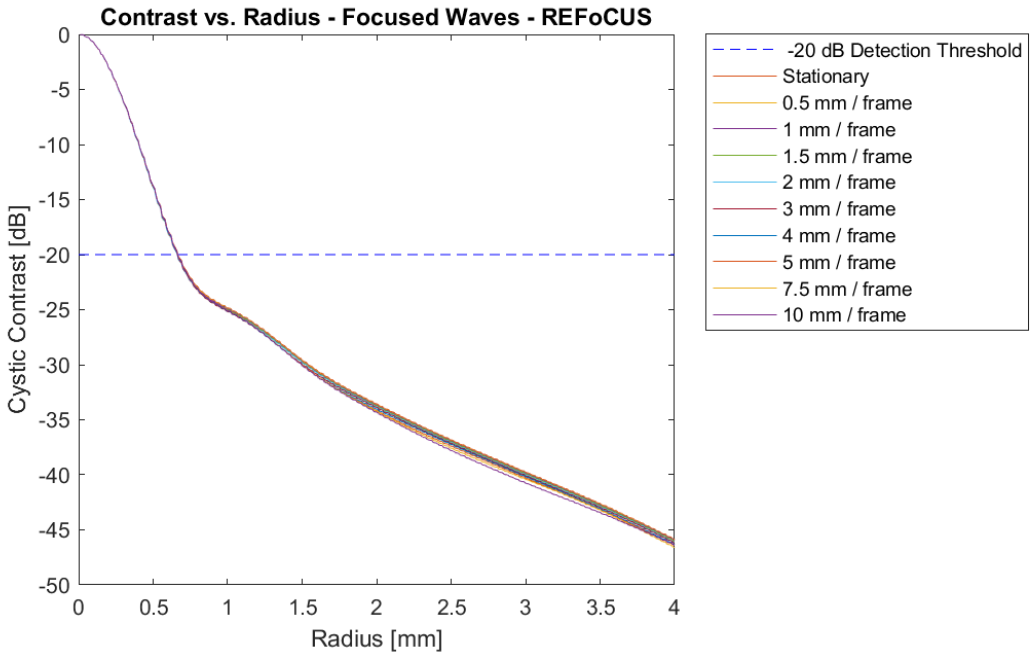

(b) Cystic Contrast vs. Radius - CR Curve - REFoCUS

Figure 3.19: Simulation - Opposite Lateral Motion (RL) - Focused Waves - CR Curves

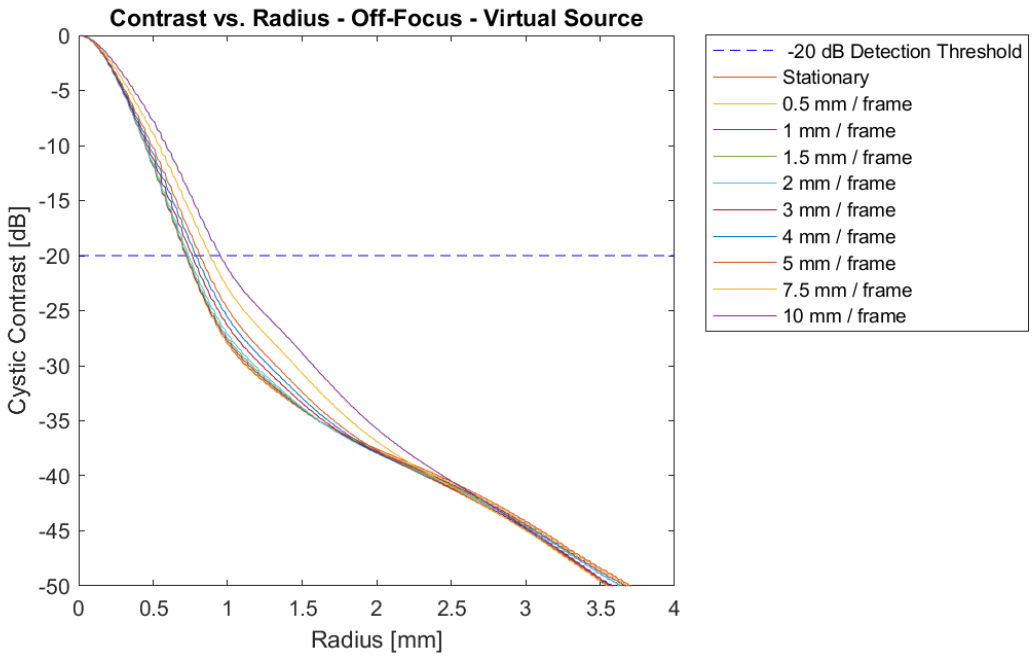

(a) Cystic Contrast vs. Radius - CR Curve - Virtual Source

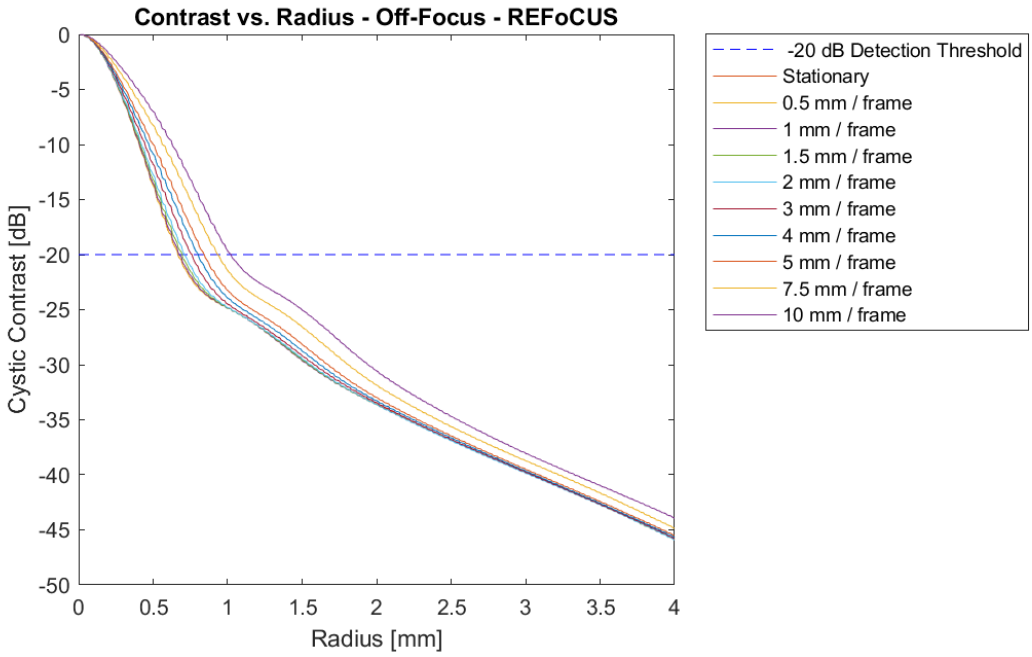

(b) Cystic Contrast vs. Radius - CR Curve - REFoCUS

Figure 3.20: Simulation - Opposite Lateral Motion (RL) - Off-Focus Waves - CR Curves

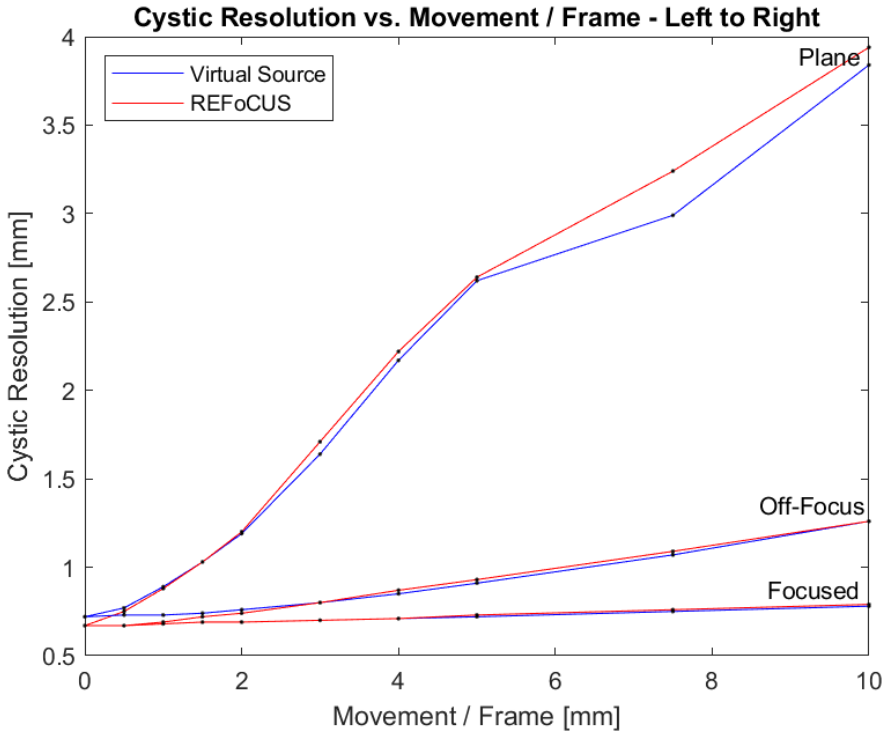

(a) Lateral Motion - Cystic Resolution vs. Movement/Frame - Initial Direction (LR)

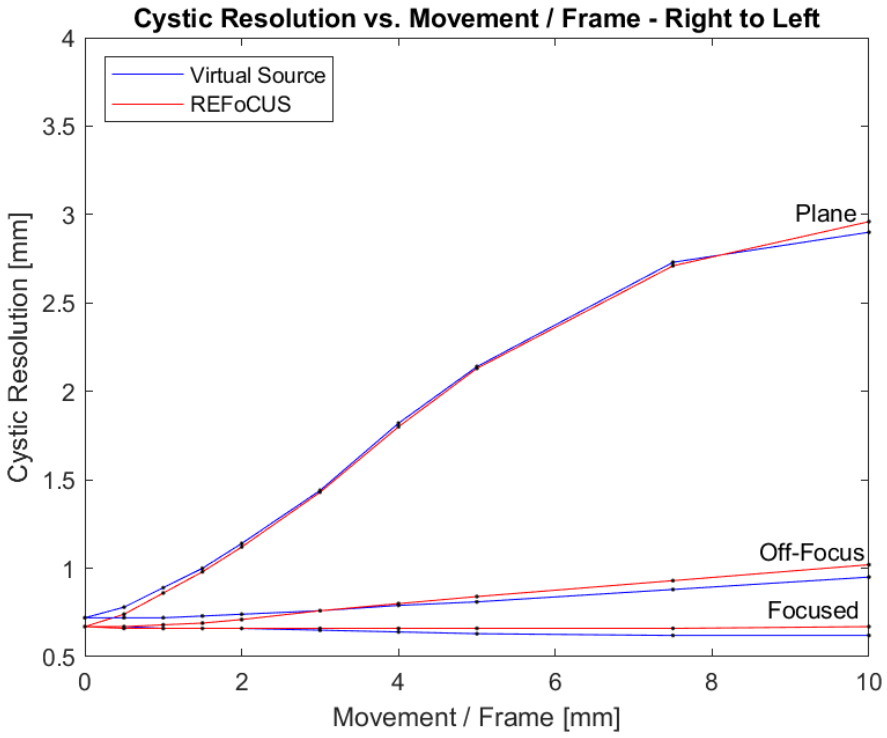

(b) Lateral Motion - Cystic Resolution vs. Movement/Frame - Opposite Direction (RL)

Figure 3.21: Simulation - Lateral Motion - Cystic Resolution vs. Movement/Frame - Plane, focused, and off-focus sequences labelled - Virtual source shown in blue and REFoCUS shown in red

Axial motion in the opposite direction was also considered, meaning that the point target moved from up to down, rather than down to up. The PSFs and contour plots from this opposite direction test match those from the initial direction test very closely. Figure 3.22 shows the same three motion cases as before (stationary, 0.5 mm/frame, and 1.5 mm/frame) imaged with plane waves. Once again, axial motion produces lateral degradation. The degree of degradation increases with velocity as before, but the direction of degradation is now flipped. Imaging up to down axial motion produces lateral degradation to the right of the PSF. Previously imagine down to up axial motion produced lateral degradation to the left of the PSF.

Imaging axial motion with focused waves produces a PSF that is unaffected by increasing velocity (Figure 3.23). Accordingly, Figure 3.24 shows the PSFs resulting from the same motion cases imaged away from the focus. These PSFs are influenced very little by increasing velocity, but some amount of lateral degradation to the left of the PSF is detectable in the 1.5 mm/frame case. These results confirm the inverse behavior of direction of degradation between plane waves and the off-focus case.

Next, CR curves were developed for every motion case. Figure 3.25 shows these CR curves for up to down axial motion imaged by plane waves. The shapes of these curves are consistent with all previous trends observed and match the CR curves from down to up axial motion imaged with plane waves (Figure 3.11). The same conclusions hold true for the CR curves developed for focused waves and the off-focus case, Figures 3.26 and 3.27, respectively.

Lastly, cystic resolution was plotted against axial movement per frame in the up to down direction (Figure 3.28b) and compared to previously reported cystic resolution values for axial movement per frame in the down to up direction (Figure 3.28a). The two sub-figures presented in Figure 3.28 are nearly identical, suggesting that sensitivity to axial motion is **not** dependent on direction of motion.

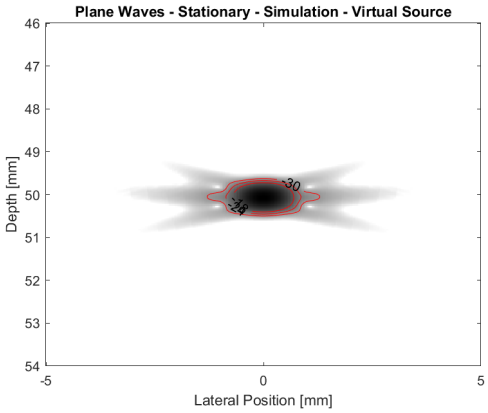

(a) Stationary - VS

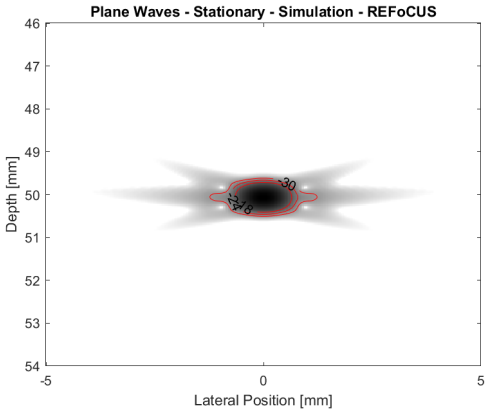

(b) Stationary - REFoCUS

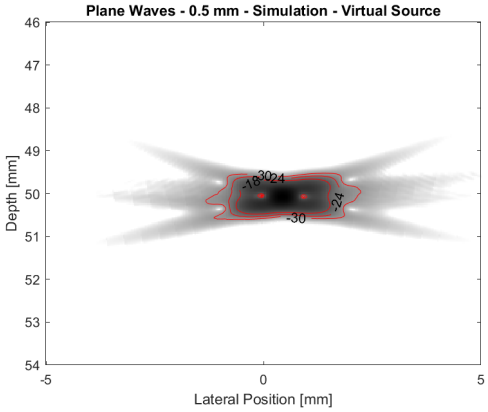

(c) 0.5 mm/frame - VS

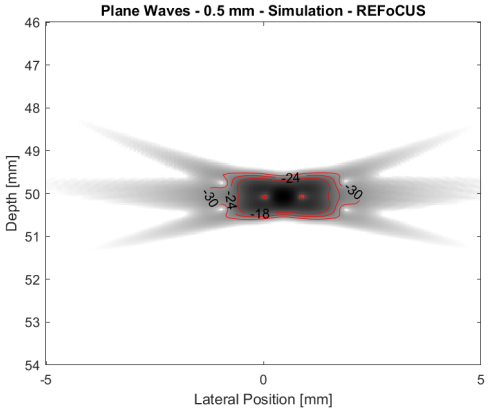

(d) 0.5 mm/frame - REFoCUS

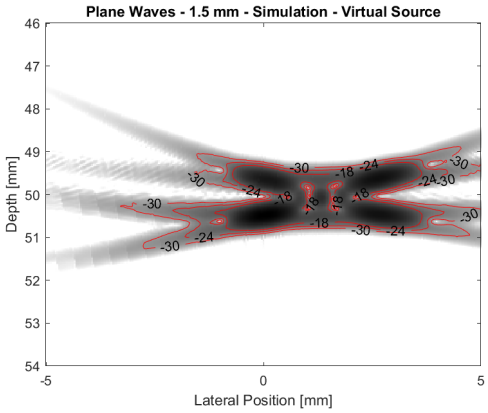

(e) 1.5 mm/frame - VS

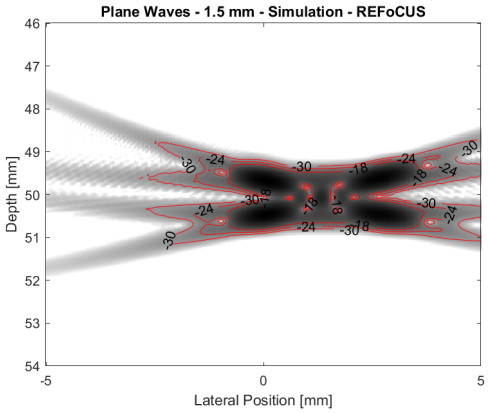

(f) 1.5 mm/frame - REFoCUS

Figure 3.22: Simulation - Opposite Axial Motion (UD) - Plane Waves - PSFs

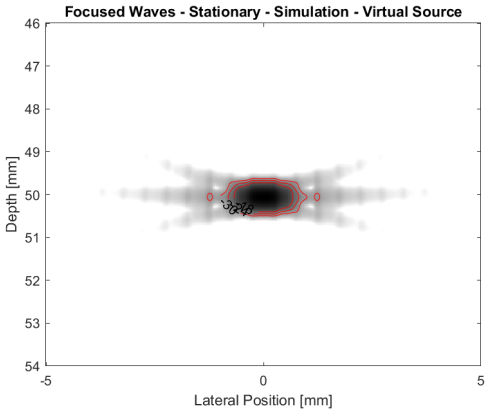

(a) Stationary - VS

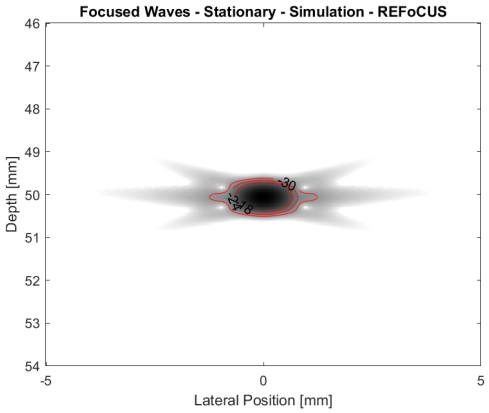

(b) Stationary - REFoCUS

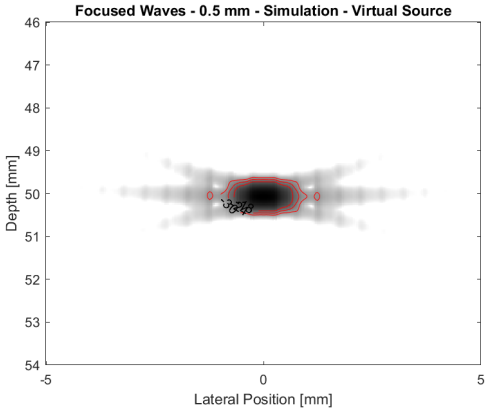

(c) 0.5 mm/frame - VS

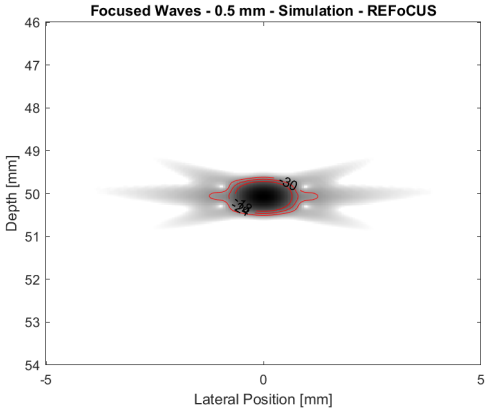

(d) 0.5 mm/frame - REFoCUS

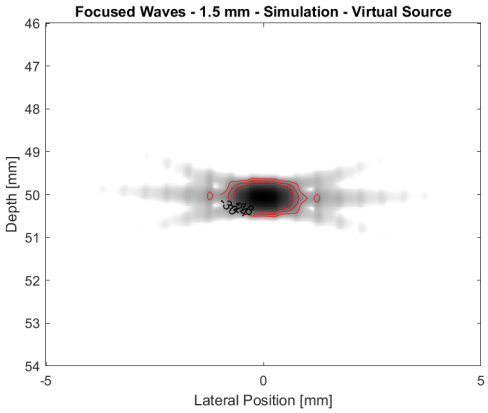

(e) 1.5 mm/frame - VS

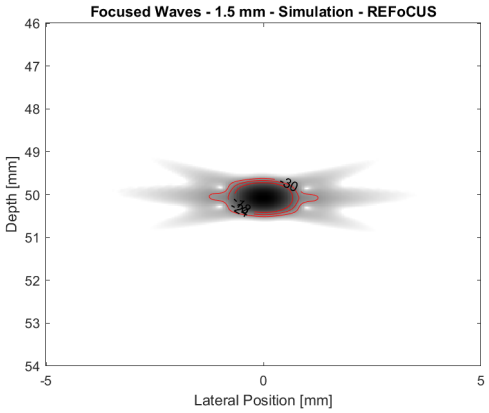

(f) 1.5 mm/frame - REFoCUS

Figure 3.23: Simulation - Opposite Axial Motion (UD) - Focused Waves - PSFs

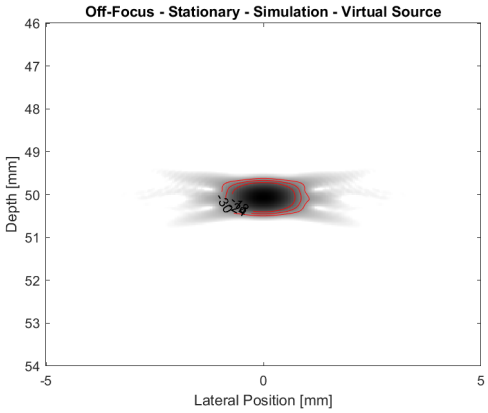

(a) Stationary - VS

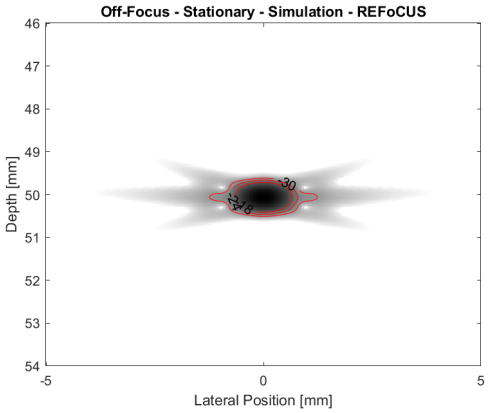

(b) Stationary - REFoCUS

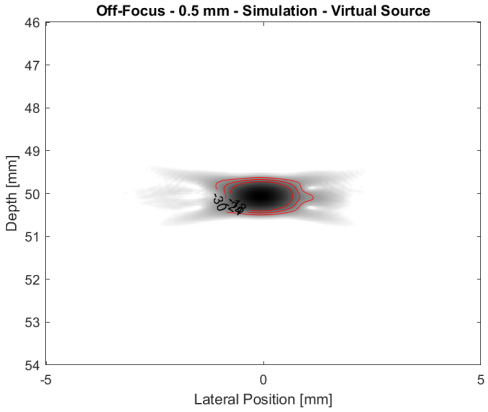

(c) 0.5 mm/frame - VS

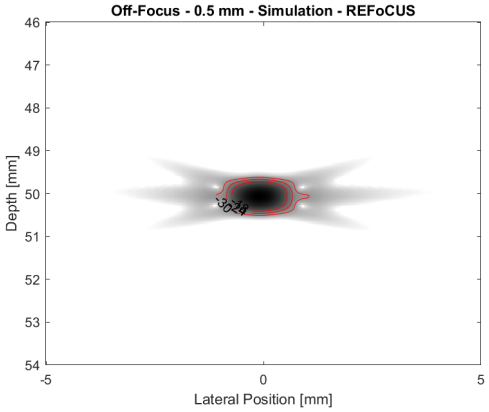

(d) 0.5 mm/frame - REFoCUS

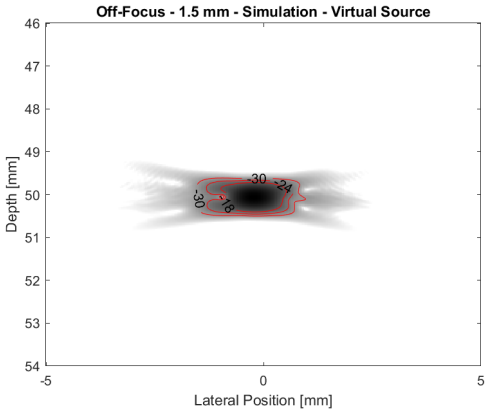

(e) 1.5 mm/frame - VS

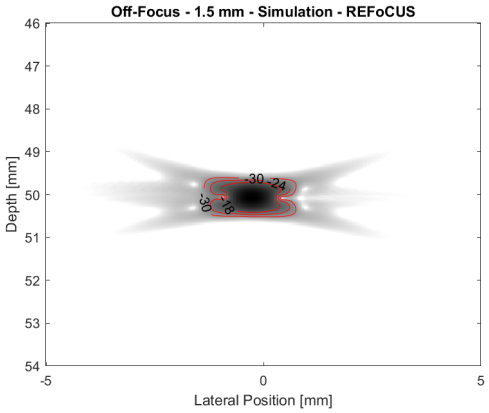

(f) 1.5 mm/frame - REFoCUS

Figure 3.24: Simulation - Opposite Axial Motion (UD) - Off-Focus - PSFs

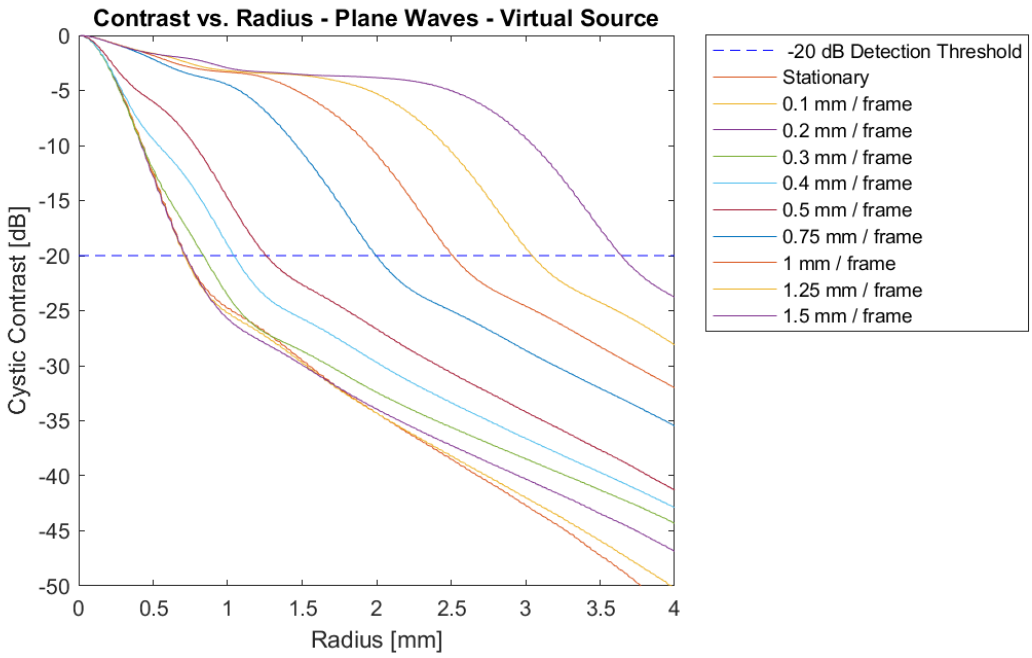

(a) Cystic Contrast vs. Radius - CR Curve - Virtual Source

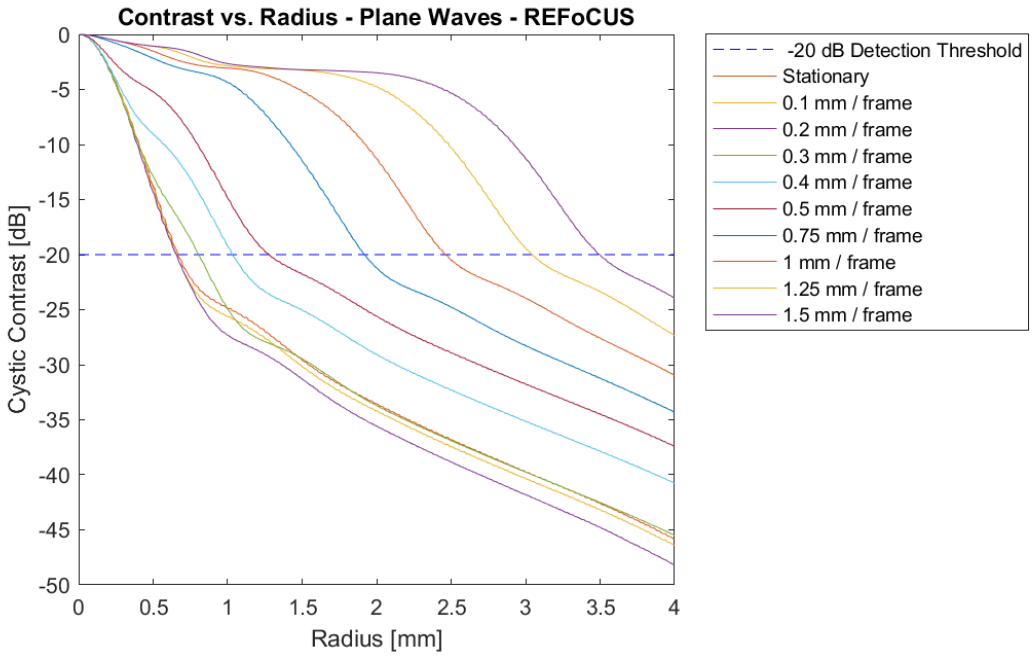

(b) Cystic Contrast vs. Radius - CR Curve - REFoCUS

Figure 3.25: Simulation - Opposite Axial Motion (UD) - Plane Waves - CR Curves

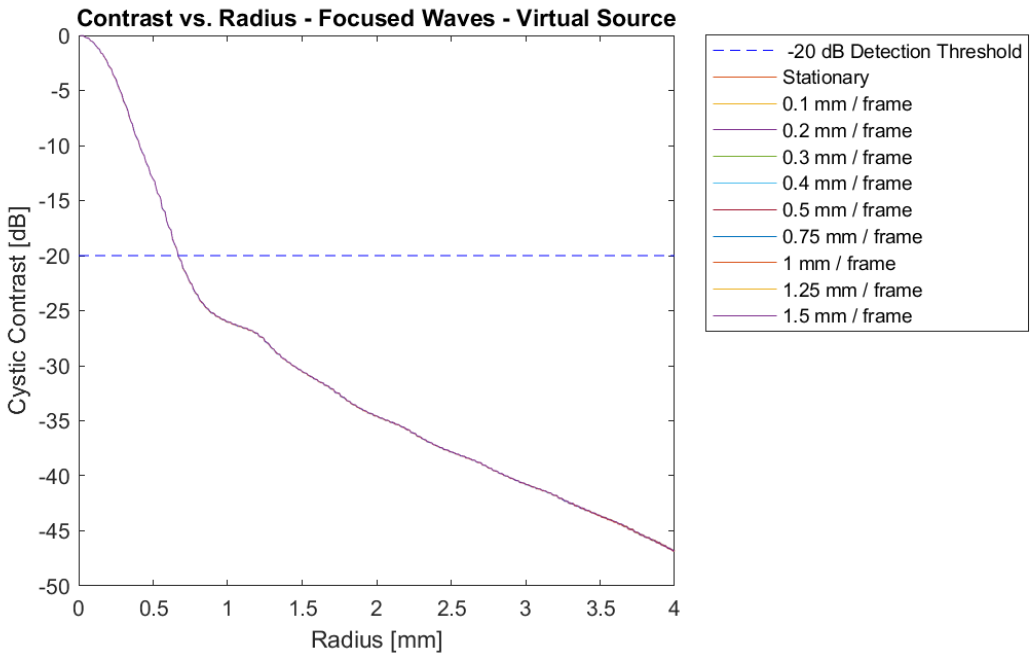

(a) Cystic Contrast vs. Radius - CR Curve - Virtual Source

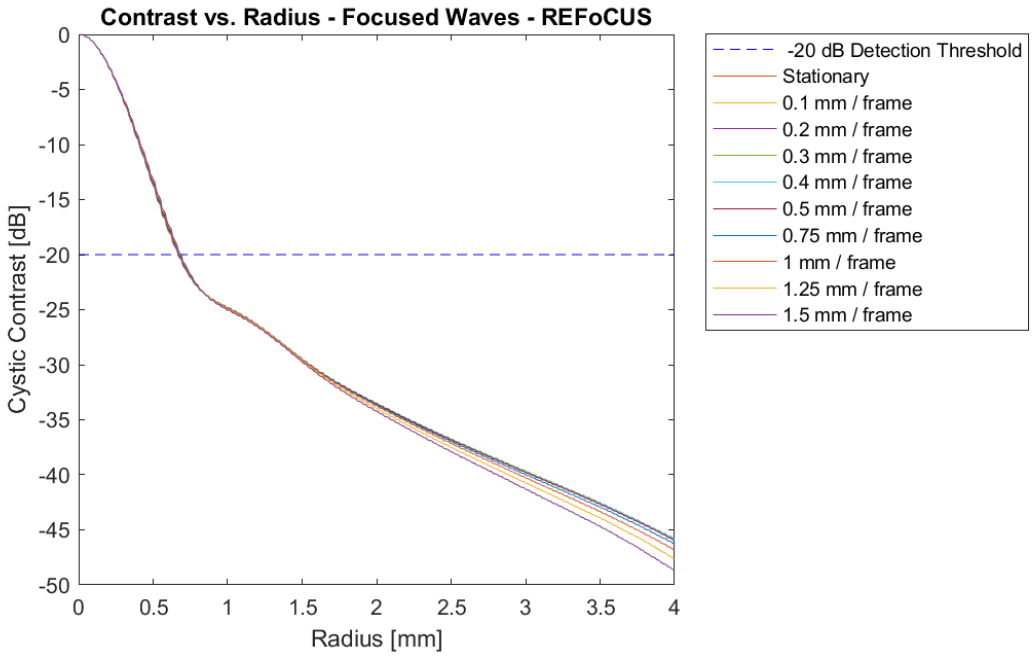

(b) Cystic Contrast vs. Radius - CR Curve - REFoCUS

Figure 3.26: Simulation - Opposite Axial Motion (UD) - Focused Waves - CR Curves

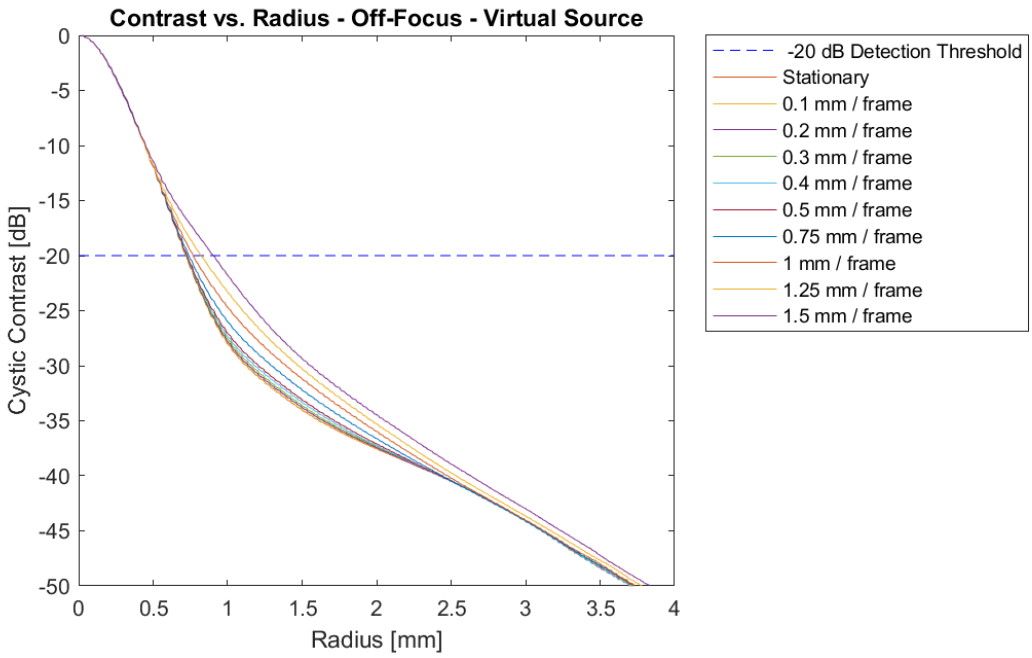

(a) Cystic Contrast vs. Radius - CR Curve - Virtual Source

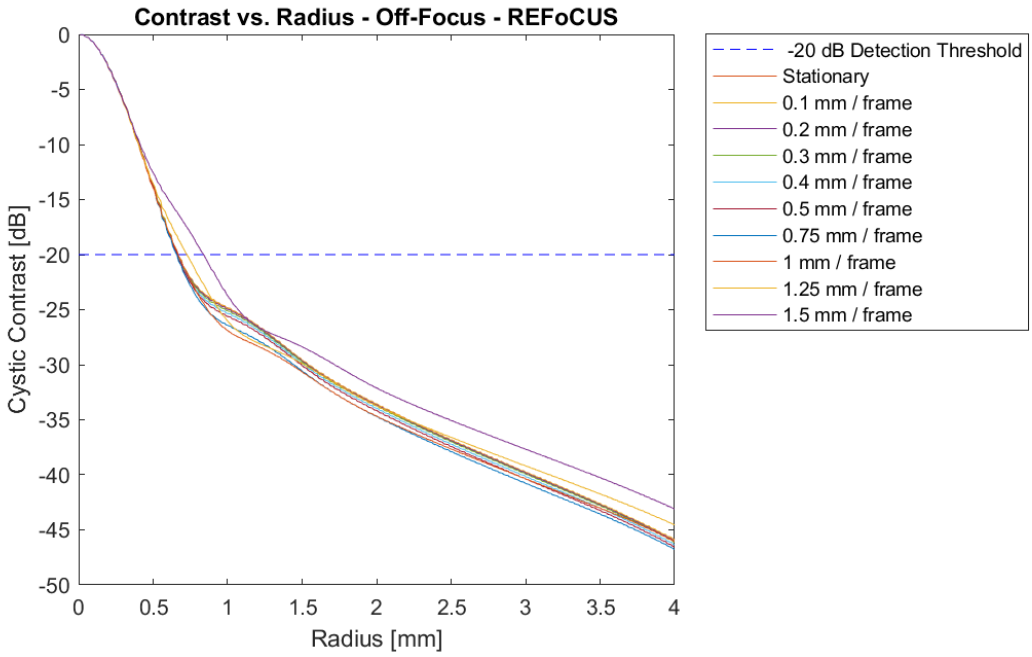

(b) Cystic Contrast vs. Radius - CR Curve - REFoCUS

Figure 3.27: Simulation - Opposite Axial Motion (UD) - Off-Focus - CR Curves

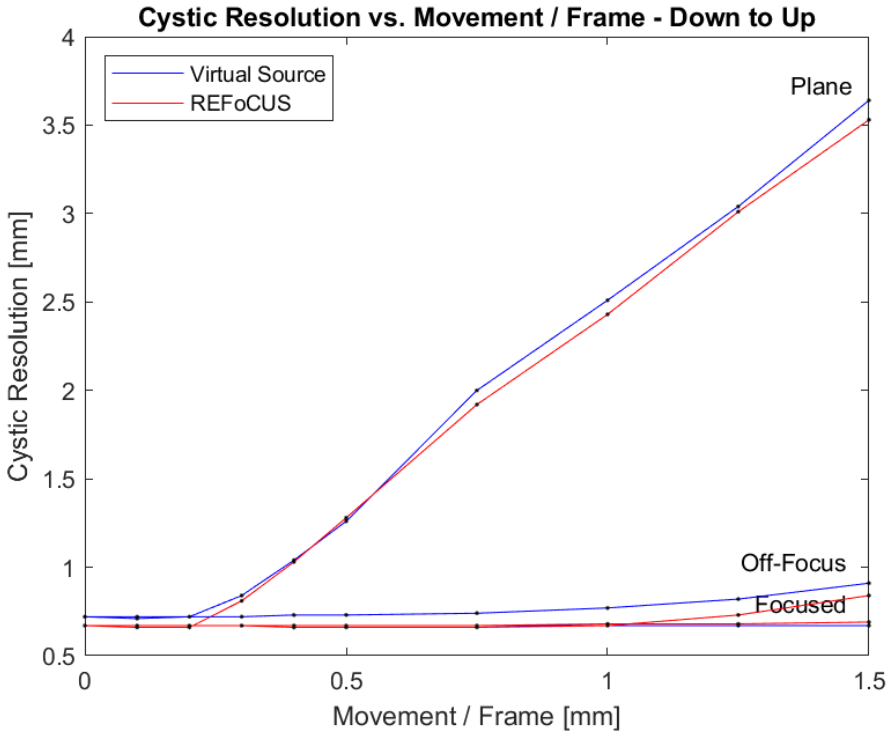

(a) Axial Motion - Cystic Resolution vs. Movement/Frame - Initial Direction (DU)

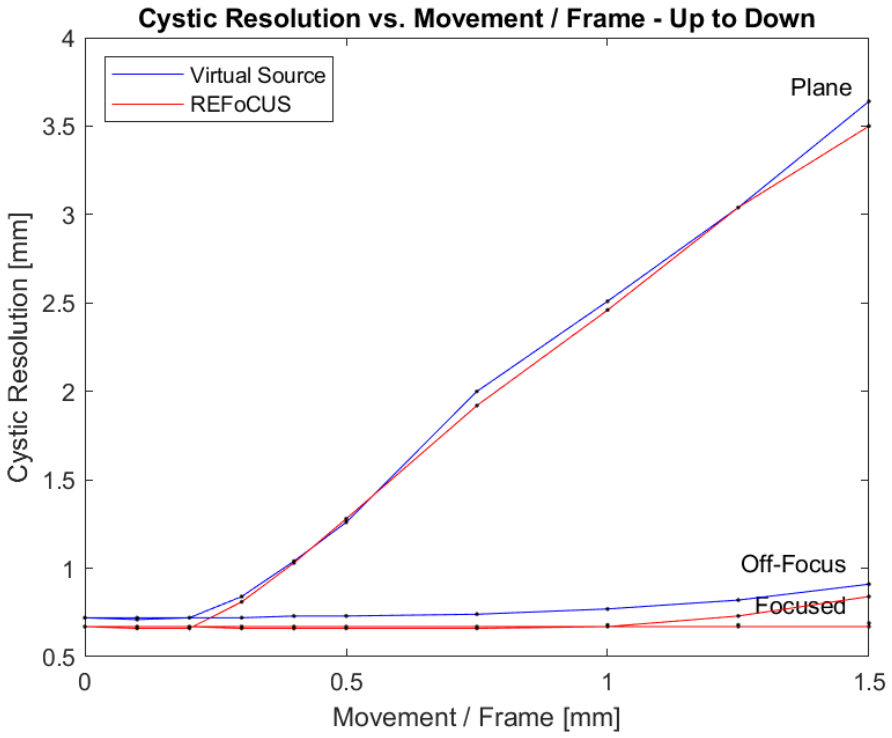

(b) Axial Motion - Cystic Resolution vs. Movement/Frame - Opposite Direction (UD)

Figure 3.28: Simulation - Axial Motion - Cystic Resolution vs. Movement/Frame - Plane, focused, and off-focus sequences labelled - Virtual source shown in blue and REFoCUS shown in red

3.1.3 Moving Point Target - Experimental Validation

Following the quantification of simulated PSFs, Verasonics scans were taken of a moving point target in order to experimentally validate the results shown above. For simplicity, the off-focus case was excluded, as was the opposite direction test. Otherwise, imaging conditions, motion cases, and sequence types were matched completely.

Contour plots from imaging lateral motion with a plane wave sequence are shown in Figure 3.29. The same three lateral motion conditions are shown as before: stationary, 3 mm/frame, and 10 mm/frame. Even the stationary baseline, experimentally, is less ideal than the PSF obtained from simulation. This is no surprise, as experimental imaging conditions are imperfect. Beyond this, the trends observed experimentally match those observed in simulation. As lateral velocity increases, lateral degradation increases and axial ringing, while stretched laterally, is largely unaffected. Experimentally, virtual source and REFoCUS beamforming match quite well.

Figure 3.30 shows the contour plots from imaging a laterally moving point target with focused waves. Here, each PSF is very similar, confirming that focused waves resolve lateral motion of a point target. Furthermore, differences in side lobe consistency are more similar across beamforming techniques.

After each contour plot is shown, corresponding CR curves are displayed for plane waves (Figure 3.31) and focused waves (3.32). Since the side lobes of these PSFs are more prominent than those produced in simulation, the magnitudes of cystic contrast values are lower experimentally. With more prominent side lobes, an ROI of equivalent size will incorporate less of an image's total energy. The spacing of CR curves in Figure 3.31 is indicative of a plane wave sequence's sensitivity to motion. That being said, the CR curves for lateral motion imaged with plane waves match very well between virtual source and REFoCUS. The CR curves for focused waves are less consistent between beamforming methods, but still show that all motion cases are better resolved by focused waves.

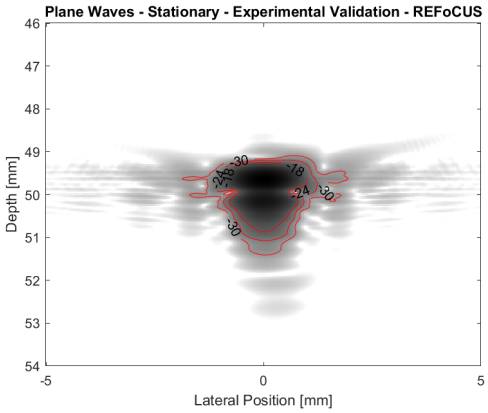

(a) Stationary - VS

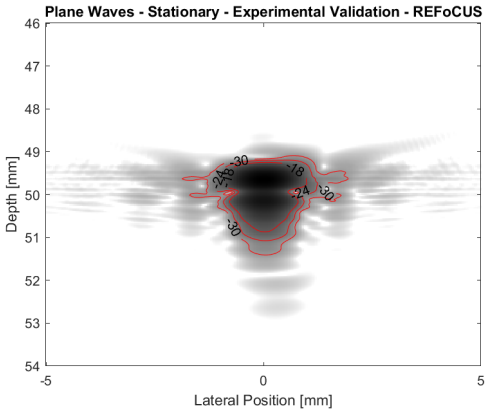

(b) Stationary - REFoCUS

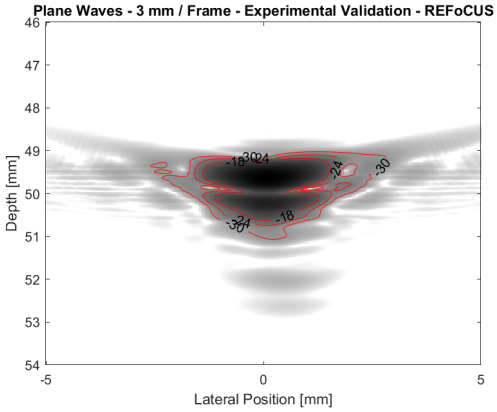

(c) 3 mm/frame - VS

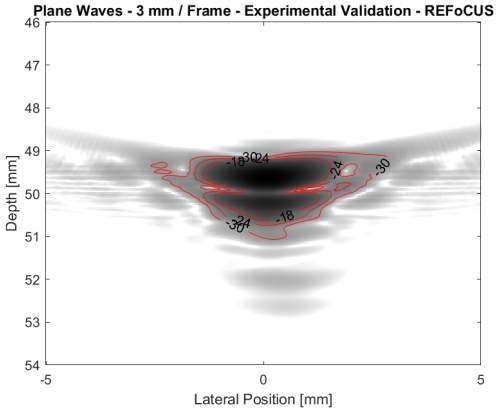

(d) 3 mm/frame - REFoCUS

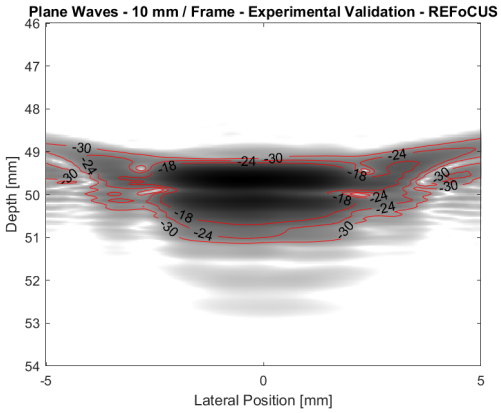

(e) 10 mm/frame - VS

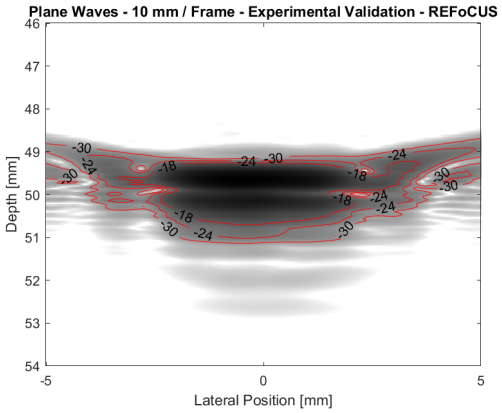

(f) 10 mm/frame - REFoCUS

Figure 3.29: Experimental - Lateral Motion - Plane Waves - PSFs

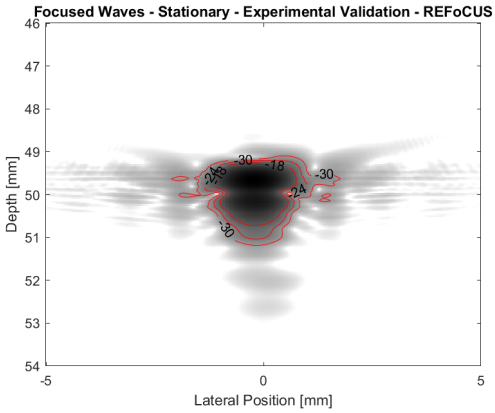

(a) Stationary - VS

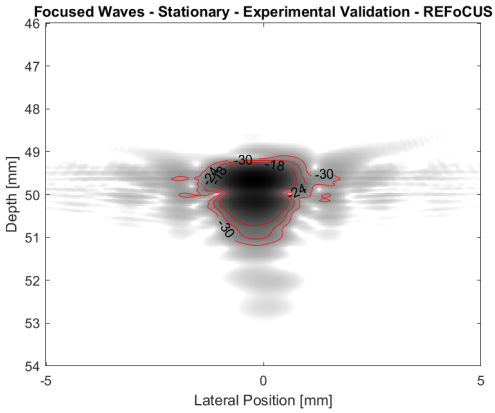

(b) Stationary - REFoCUS

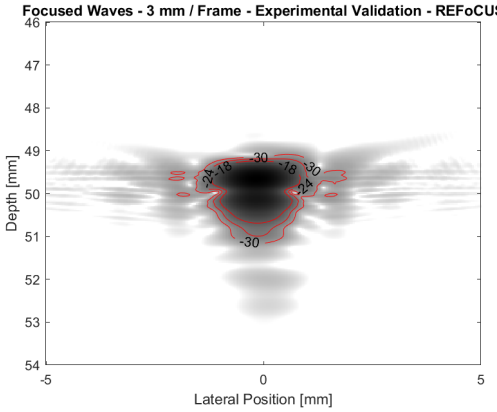

(c) 3 mm/frame - VS

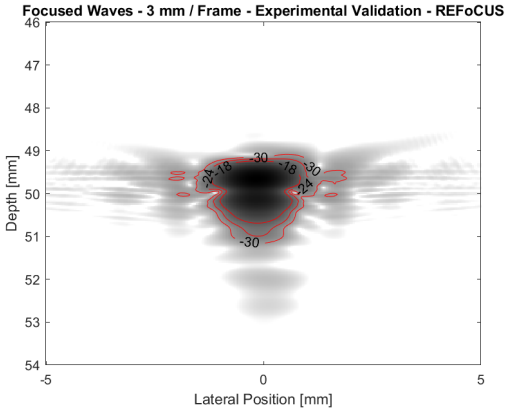

(d) 3 mm/frame - REFoCUS

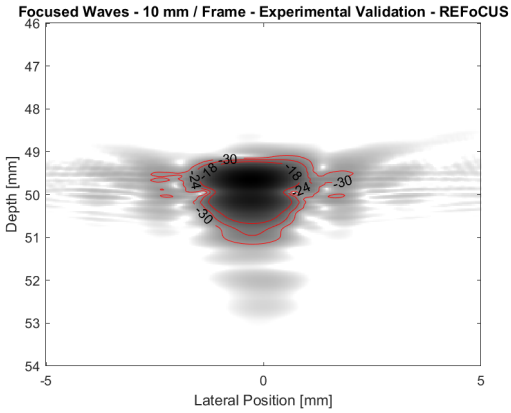

(e) 10 mm/frame - VS

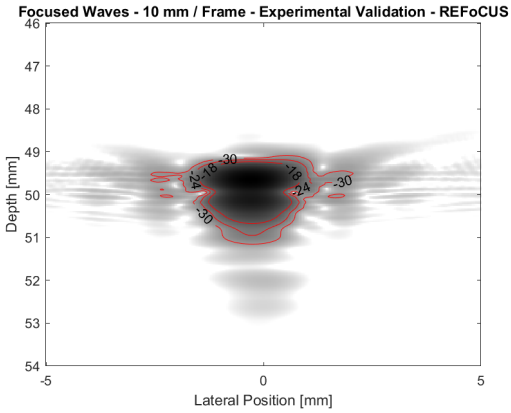

(f) 10 mm/frame - REFoCUS

Figure 3.30: Experimental - Lateral Motion - Focused Waves - PSFs

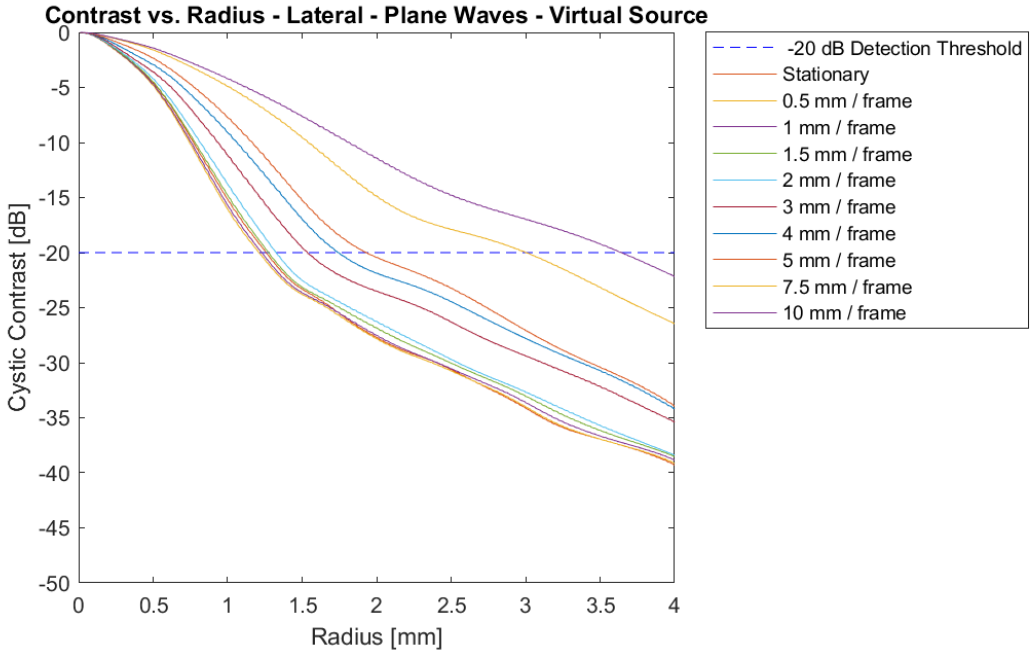

(a) Cystic Contrast vs. Radius - CR Curve - Virtual Source

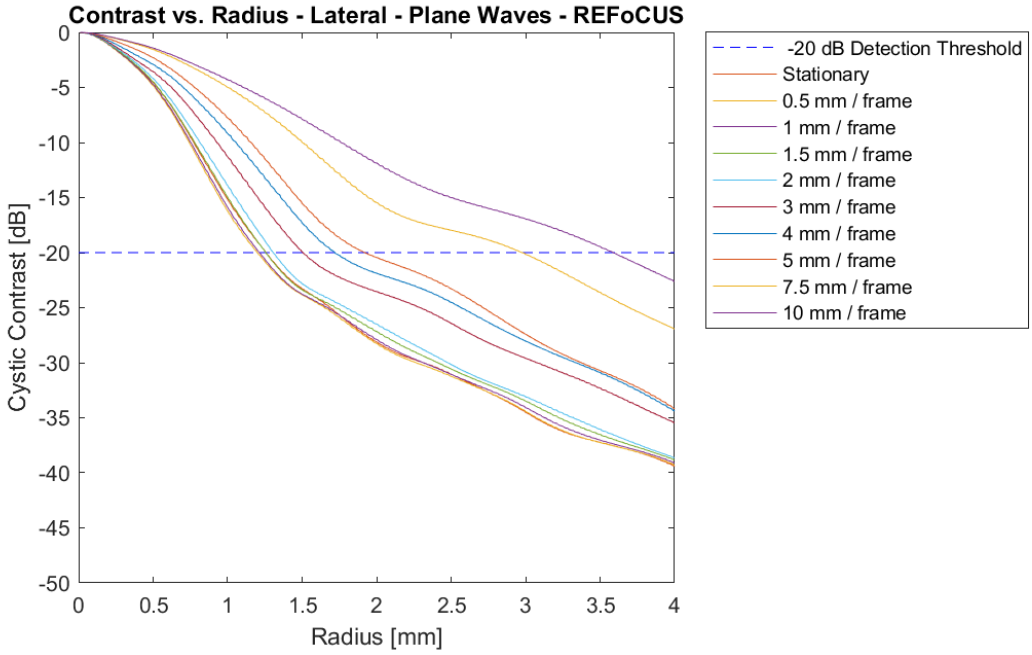

(b) Cystic Contrast vs. Radius - CR Curve - REFoCUS

Figure 3.31: Experimental - Lateral Motion - Plane Waves - CR Curves

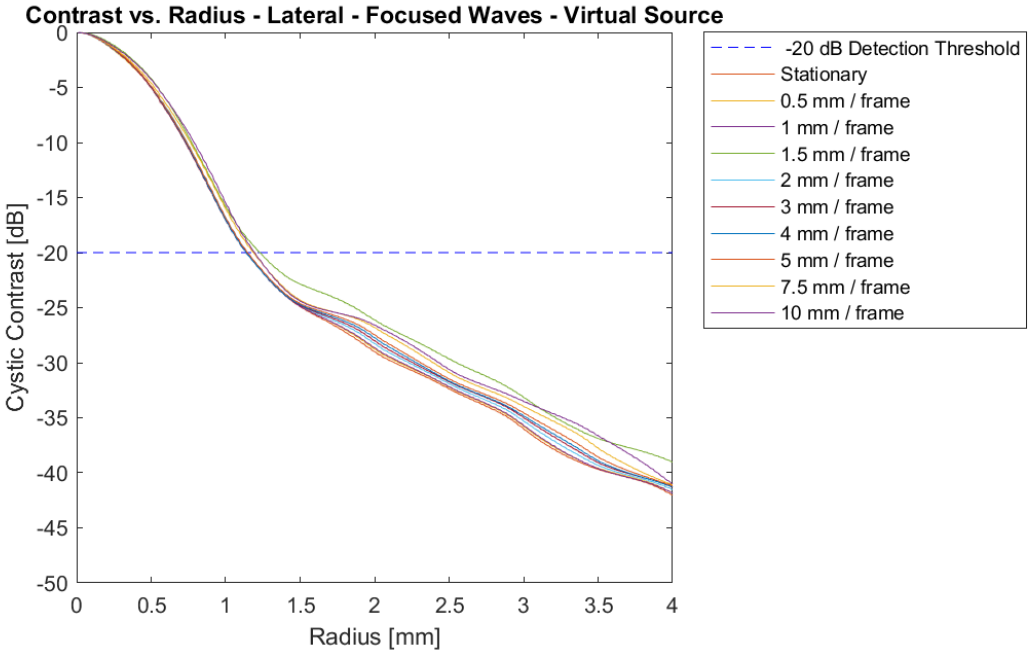

(a) Cystic Contrast vs. Radius - CR Curve - Virtual Source

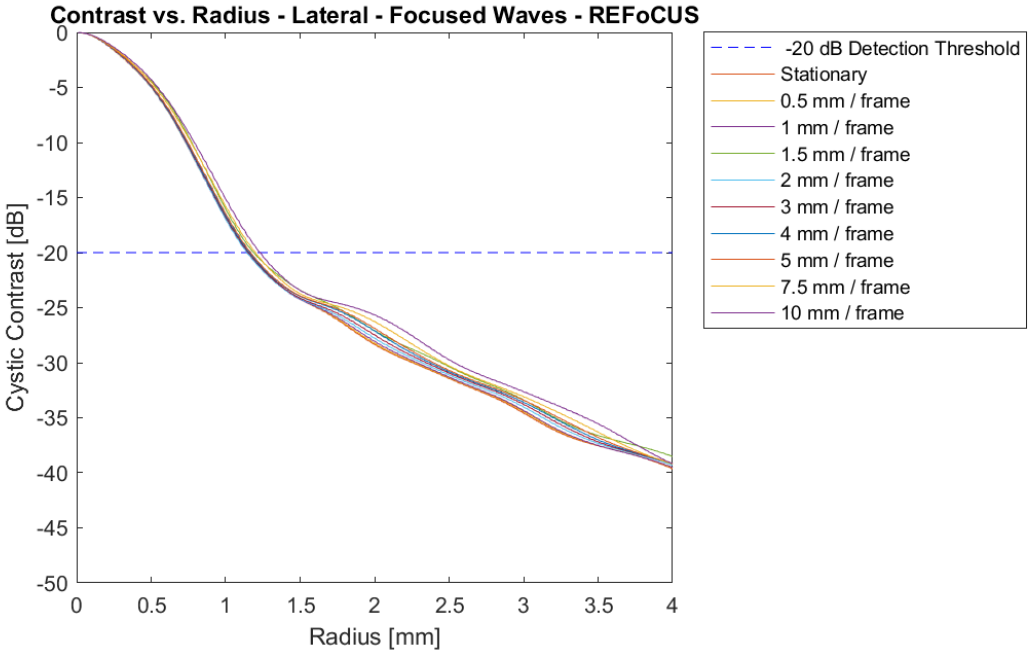

(b) Cystic Contrast vs. Radius - CR Curve - REFoCUS

Figure 3.32: Experimental - Lateral Motion - Focused Waves - CR Curves

Accordingly, experimental scans were taken of axial motion. The contour plots of axial motion imaged with plane waves are shown in Figure 3.33. Again, the same three axial motion cases are shown as before: stationary, 0.5 mm/frame, and 1.5 mm/frame. Despite imperfect experimental imaging conditions, the same trends observed in simulation hold true for axial motion. As axial velocity increases, lateral degradation increases. The 0.5 mm/frame axial motion case is somewhat similar to the stationary PSF, but the 1.5 mm/frame axial motion case exhibits severe degradation to the left of the center axis. In these images, there are no discernable differences between virtual source and REFoCUS beamforming.

Contour plots from imaging axial motion with focused waves, then, are presented in Figure 3.30. As expected, the shape of each PSF matches quite well, even in the presence of significant axial motion. Interestingly, the location of the PSF in the 1.5 mm/frame axial motion case appears to be shifted slightly to the left. Despite being the same shape as the stationary PSF, this subtle shifting may be a form of motion-induced degradation.

Figure 3.35 shows the CR curves for all axial motion cases, imaged with plane waves. Once again, the separation of these curves indicates that plane waves are unable to resolve axial motion. Overall, the CR curves match across beamforming methods, with the exception of the largest three motion cases. REFoCUS resolved the 1 mm/frame and 1.5 mm/frame axial motion cases better than virtual source, but resolved the 1.25 mm/frame axial motion case worse than virtual source. Although the reasons for these difference are unclear, it is worth noting that all three of these cases exhibit drastic degradation. When considering the CR curves from focused sequences (Figure 3.36), all motion cases are resolved similarly, regardless of motion or beamforming technique.

Lastly, the cystic resolution of each CR curve was determined and plotted against motion per frame. Lateral motion results are shown in Figure 3.37a and axial motion results are shown in Figure 3.37b. Note that the x-axes for these two plots differ by nearly an order of magnitude. Focused waves, however, clearly outperform plane waves in the presence of any type of motion.

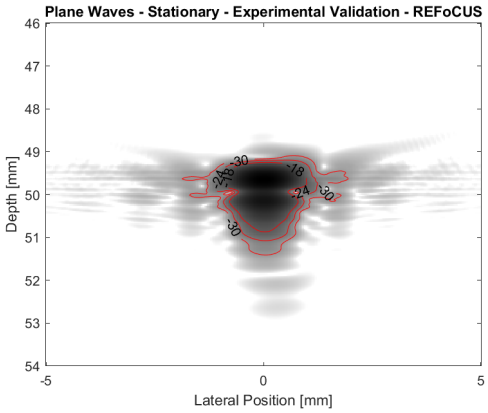

(a) Stationary - VS

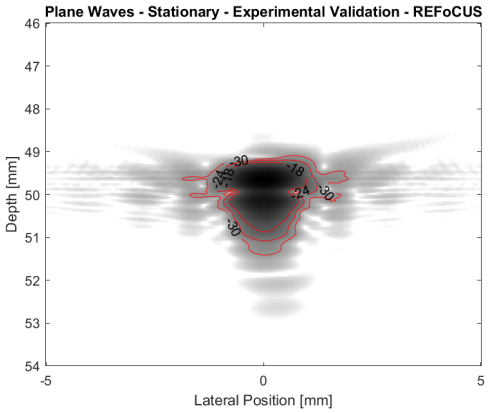

(b) Stationary - REFoCUS

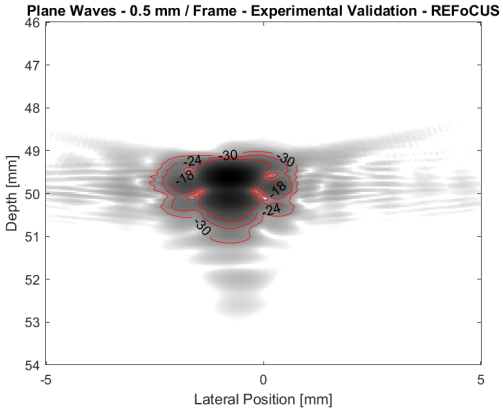

(c) 0.5 mm/frame - VS

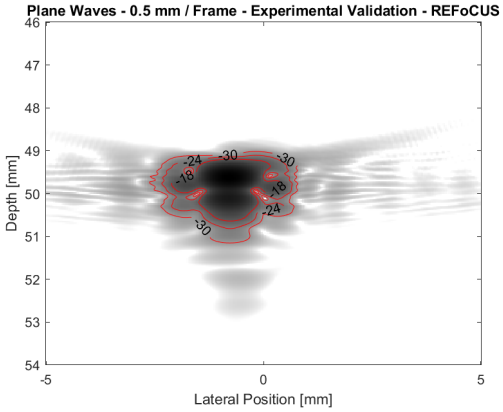

(d) 0.5 mm/frame - REFoCUS

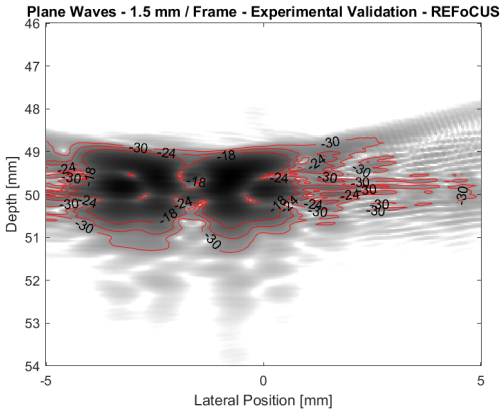

(e) 1.5 mm/frame - VS

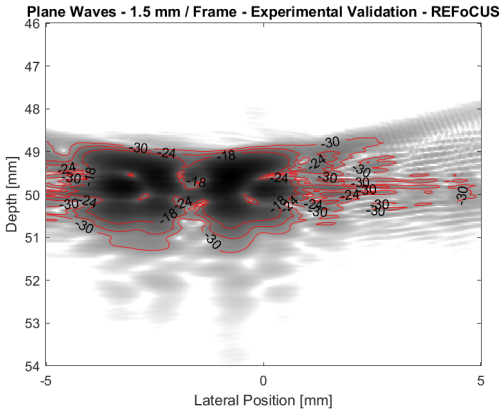

(f) 1.5 mm/frame - REFoCUS

Figure 3.33: Experimental - Axial Motion - Plane Waves - PSFs

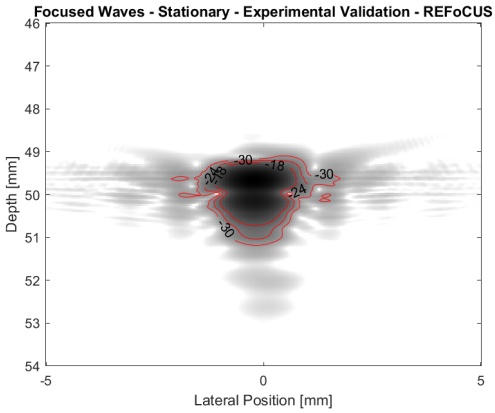

(a) Stationary - VS

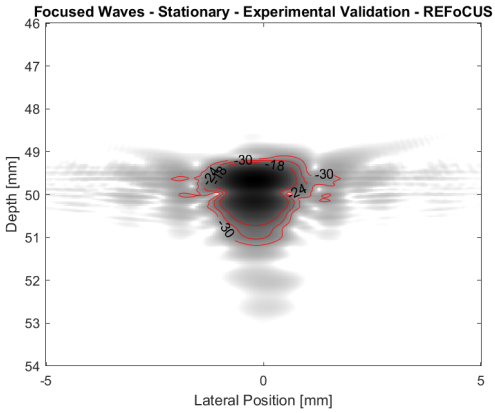

(b) Stationary - REFoCUS

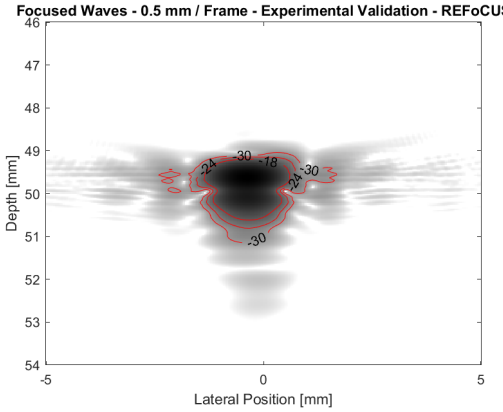

(c) 0.5 mm/frame - VS

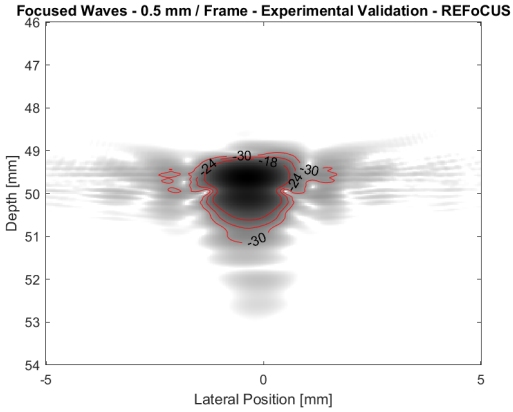

(d) 0.5 mm/frame - REFoCUS

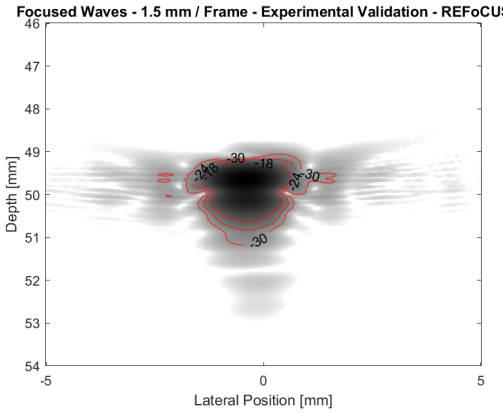

(e) 1.5 mm/frame - VS

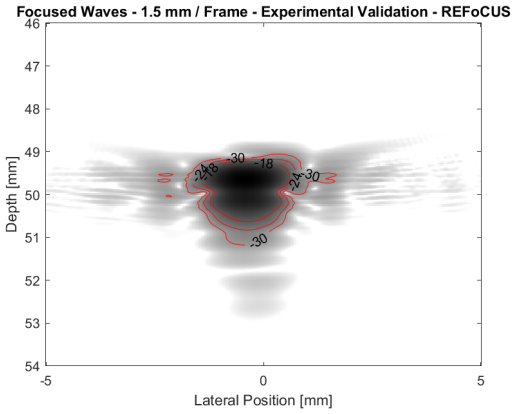

(f) 1.5 mm/frame - REFoCUS

Figure 3.34: Experimental - Axial Motion - Focused Waves - PSFs

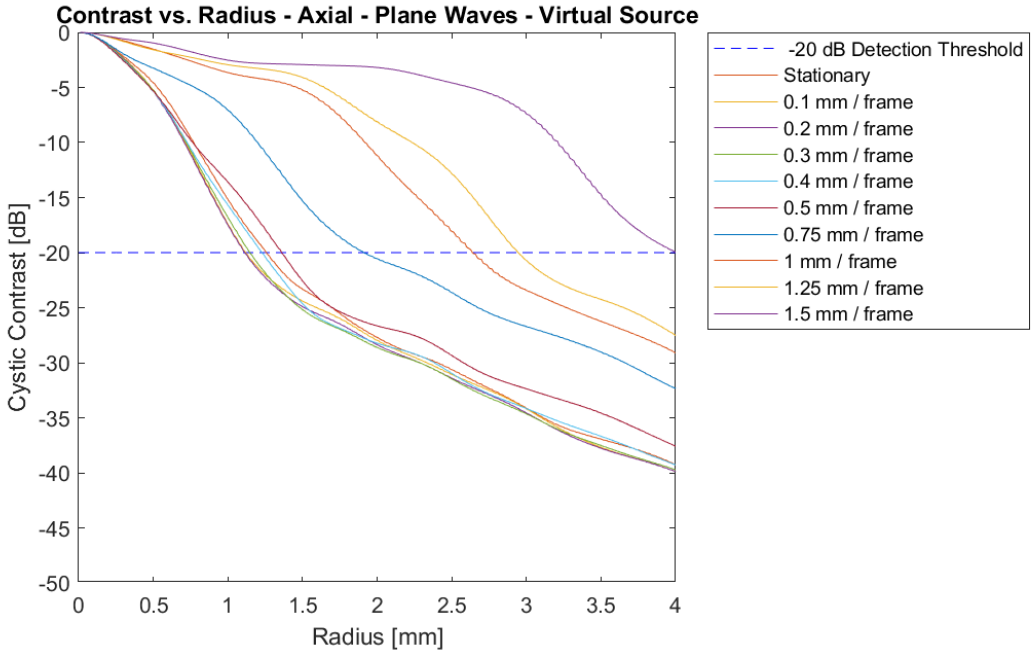

(a) Cystic Contrast vs. Radius - CR Curve - Virtual Source

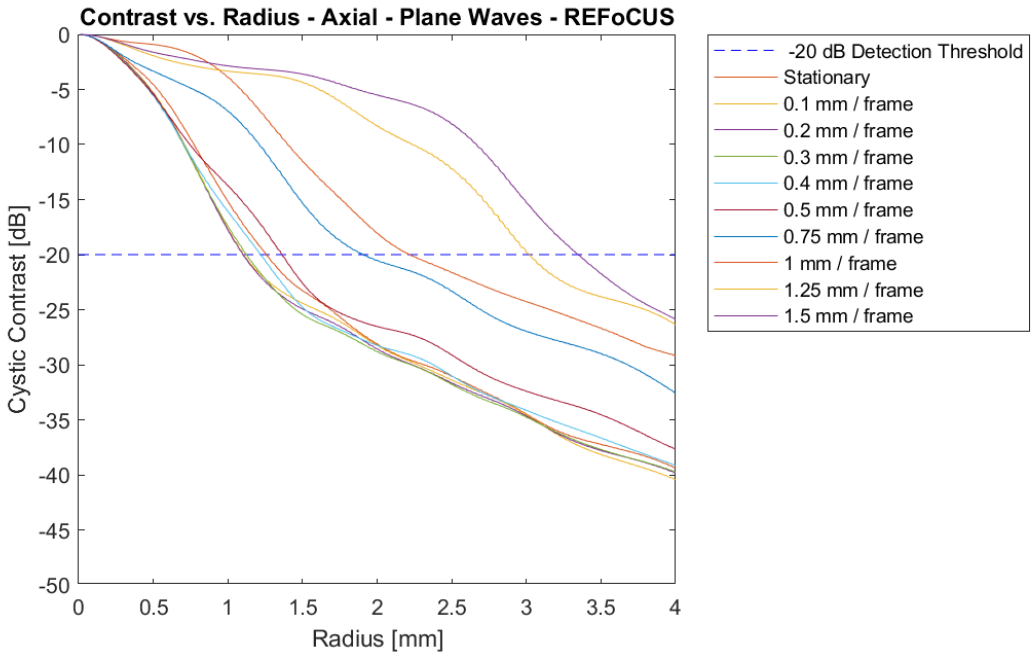

(b) Cystic Contrast vs. Radius - CR Curve - REFoCUS

Figure 3.35: Experimental - Axial Motion - Plane Waves - CR Curves

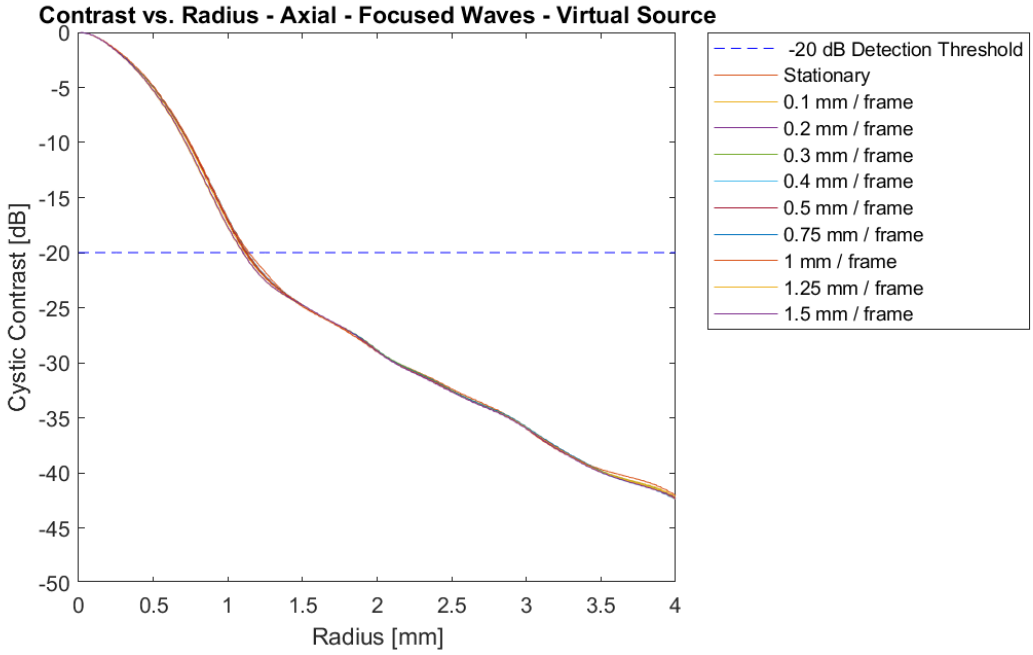

(a) Cystic Contrast vs. Radius - CR Curve - Virtual Source

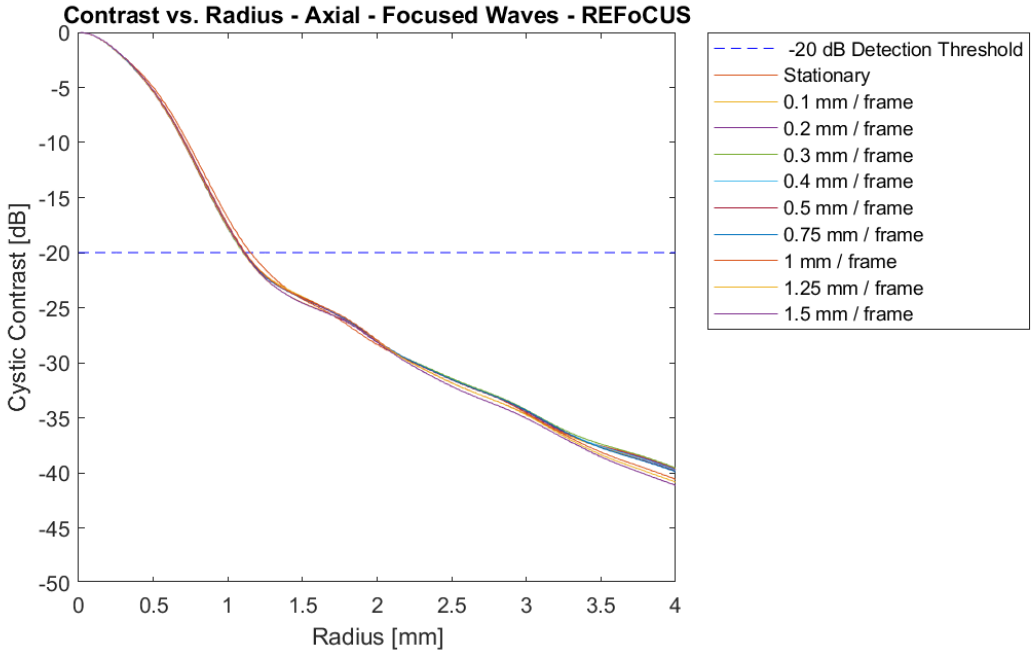

(b) Cystic Contrast vs. Radius - CR Curve - REFoCUS

Figure 3.36: Experimental - Lateral Motion - Axial Waves - CR Curves

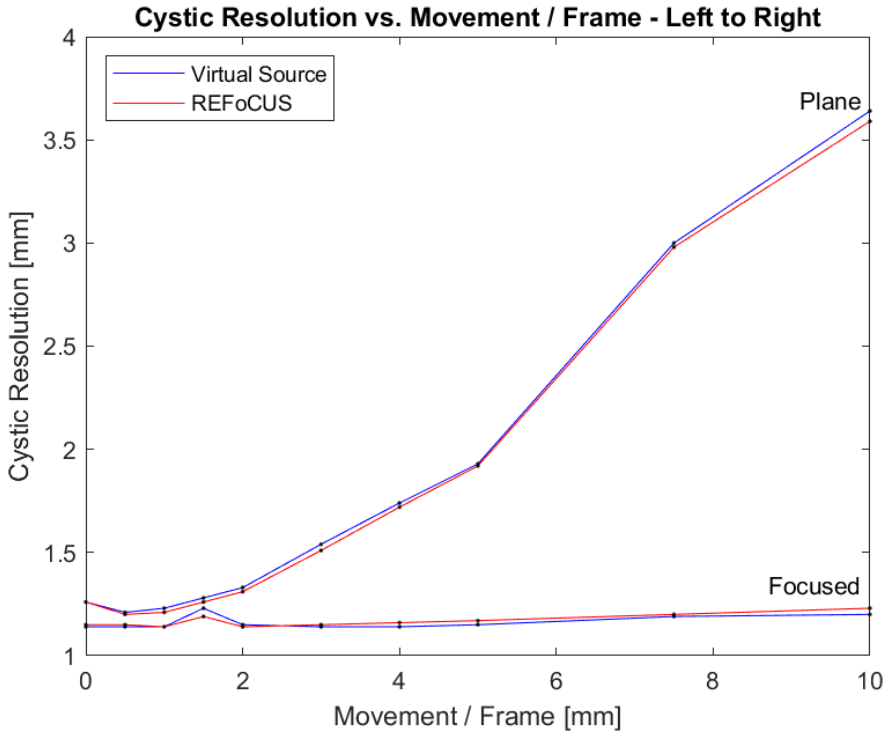

(a) Lateral Motion - Cystic Resolution vs. Movement/Frame

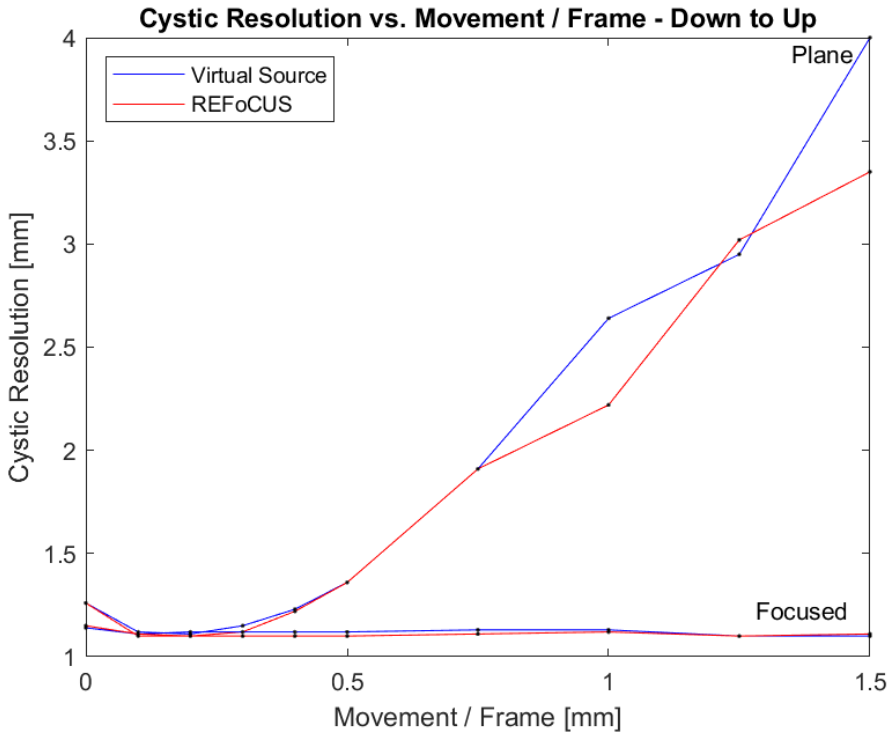

(b) Axial Motion - Cystic Resolution vs. Movement/Frame

Figure 3.37: Experimental - Lateral and Axial Motion - Cystic Resolution vs. Movement/Frame - Plane and focused sequences labelled - Virtual source shown in blue and REFoCUS shown in red

3.2 Mixed Sequences

3.2.1 Data Combination

Data combination was possible with both virtual source and REFoCUS beamforming. The PSFs from imaging 1 mm of axial motion per frame with both plane and focused waves and beamformed with both methods are shown in Figure A.1. The slightly extended side lobes observable in A.1c exist because REFoCUS does not apply a spatial mask. Figure A.2, then, shows 'adding' mixed sequences (left) and 'replacing' mixed sequences (right). Although the PSF in Figure A.2d is severely degraded, it would still generate a uniform image. In contrast, the PSF in Figure A.2b exhibits discontinuities where data are replaced. Thus, REFoCUS allows for simpler and more consistent data combination.

The transmissions order of all subsequent mixed sequences was verified by plotting delay matrices. The delays for plane and focused sequences are shown in Figure B.1. Similarly, the delays for all 'adding' sequences are shown in Figure B.2 and the delays for all 'replacing' sequences are shown in Figure B.3. All sub-figures indicate the total number of transmissions (n) per sequence.

3.2.2 Moving Point Target - Un-Weighted and Weighted - Mixed Sequences

In order to evaluate the efficacy of weighting mixed sequences for resolving motion, a moving point target was simulated in Field II with lateral motion of 5 mm/frame and axial motion of 1 mm/frame (33.4 and 6.7 cm/s, respectively). From these simulations, the outputs of contour plots, CR curves, and cystic resolution plots were produced. Since the every mixing case, unweighted and weighted, was applied to both types of motion, controls are required. Figure 3.38 shows 2 control images: (a) lateral motion imaged with plane waves and (b) lateral motion imaged with focused waves. All control images are unweighted. As before, significant degradation can be seen in the plane wave image, whereas focused waves resolved motion well. Since mixed sequences are a combination of the plane and focused data sets, each contour plot should combine the behaviors of the two control images. For the following results, contour plots from three mixture cases are

shown: middle 20 focused added to plane, middle 20 focused replacing plane, and every fourth focused replacing plane.

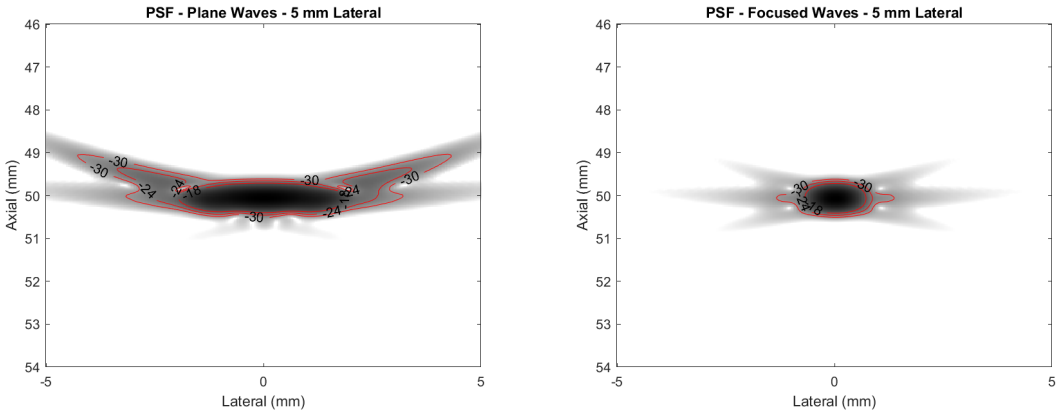

(a) 5 mm/frame - Lateral - Plane

(b) 5 mm/frame - Lateral - Focused

Figure 3.38: Mixed Sequences - Control Images - 5 mm/frame Lateral Motion - REFoCUS

The contour plots for lateral motion imaged with plane waves are shown in Figure 3.38a. The left column shows unweighted PSFs and the right column displays their weighted counterparts. The characteristic lateral degradation of plane waves is still noticeable in every image, but the intensity of degradation and, consequently, side lobes, is diminished when weighting is applied. As far as unweighted sequences are concerned, few improvements are observed. The middle 20 added case shows slightly reduced side lobes, but most unweighted cases did not improve upon the control plane sequence. Replacing every fourth plane transmission with a focused transmission produced noticeable texture differences in the PSF for both the unweighted and the weighted case, although more prominent when weighted. For this reason, adding or replacing the middle 20 transmissions appears more promising, as energy is more centralized and side lobes are drastically reduced.

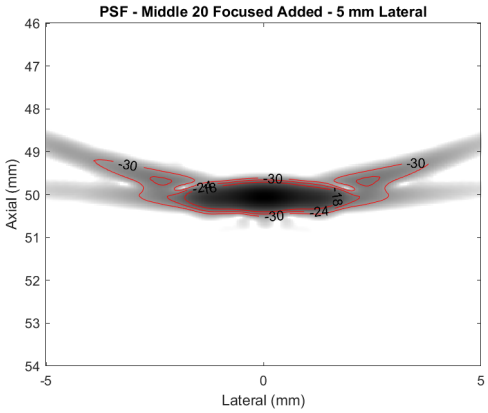

(a) Lateral - Middle 20 Added

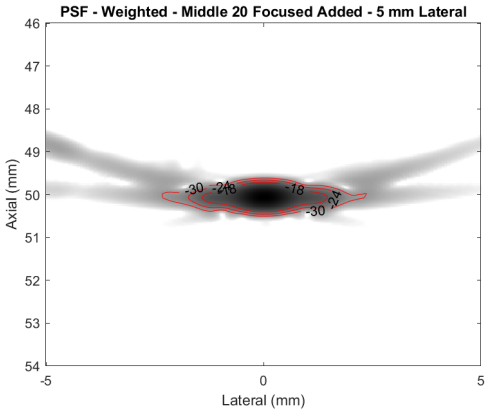

(b) Lateral - Middle 20 Added - Weighted

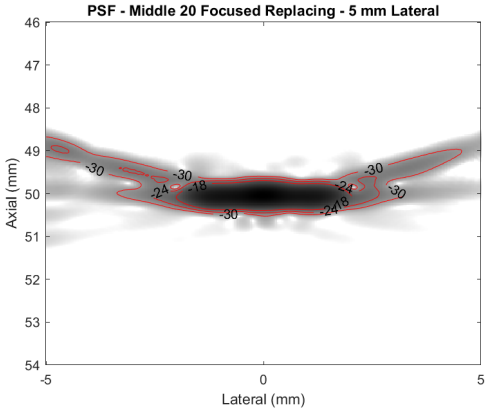

(c) Lateral - Middle 20 Replaced

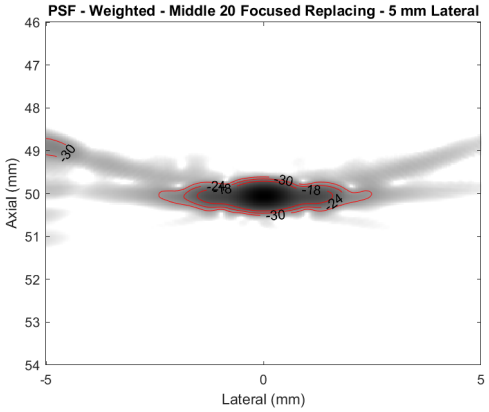

(d) Lateral - Middle 20 Replaced - Weighted

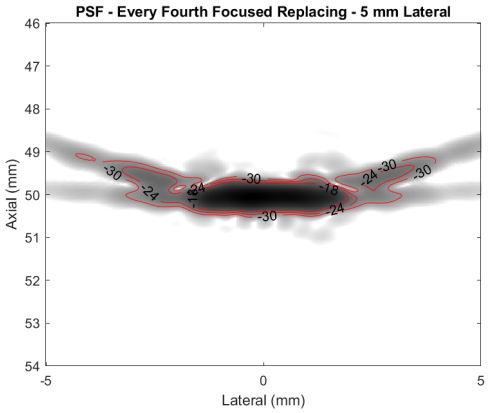

(e) Lateral - Every Fourth Replaced

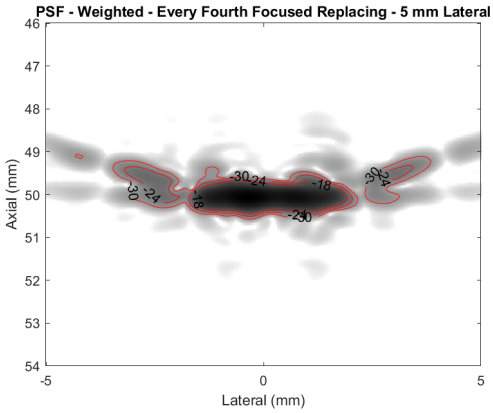

(f) Lateral - Every Fourth Replaced - Weighted

Figure 3.39: Mixed Sequences - Lateral - Contour Plots - Three mixing cases shown: middle 20 focused added, middle 20 focused replacing plane, and every fourth focused replacing plane

Figure 3.40a shows the CR curves for all 'adding' mixture cases and Figure 3.40b shows the same CR curves after weighting was applied. Mixed sequences without weighting clearly match the CR curve of the plane sequence rather than the focused sequence. In some cases, the image quality is diminished compared to the plane control. Once weighting was applied, two mixed sequences showed CR curves closer to the focused CR curve. Specifically, the 'middle 20 focused' and 'full combination' sequences. Similarly, the unweighted and weighted CR curves for the 'replacing' mixture cases are shown in Figures 3.41a and 3.41b. Once again, unweighted mixed sequences perform, at best, much like a plane sequence. When weighted, both the 'middle 20 replacing and 'middle 30 replacing' sequences show improvement compared to the plane sequence.

The overall results of weighted mixed sequences with **lateral** motion can be seen in Figure 3.42. Cystic resolution values are plotted for each sequence type for both the unweighted and weighted case. The left-most section of the figure shows both controls (plane and focused, only), the middle section shows all 'adding' cases, and the right section shows all 'replacing' cases. Note that when the middle 10 plane transmissions were replaced with focused transmissions and a weighted, cystic contrast did not fall below -20 dB. None of the unweighted sequences outperformed the plane control. However, several weighted sequences do show improved resolution: full combo, middle 20 added and replacing, middle 30 replacing, and 1/4 added and replacing.

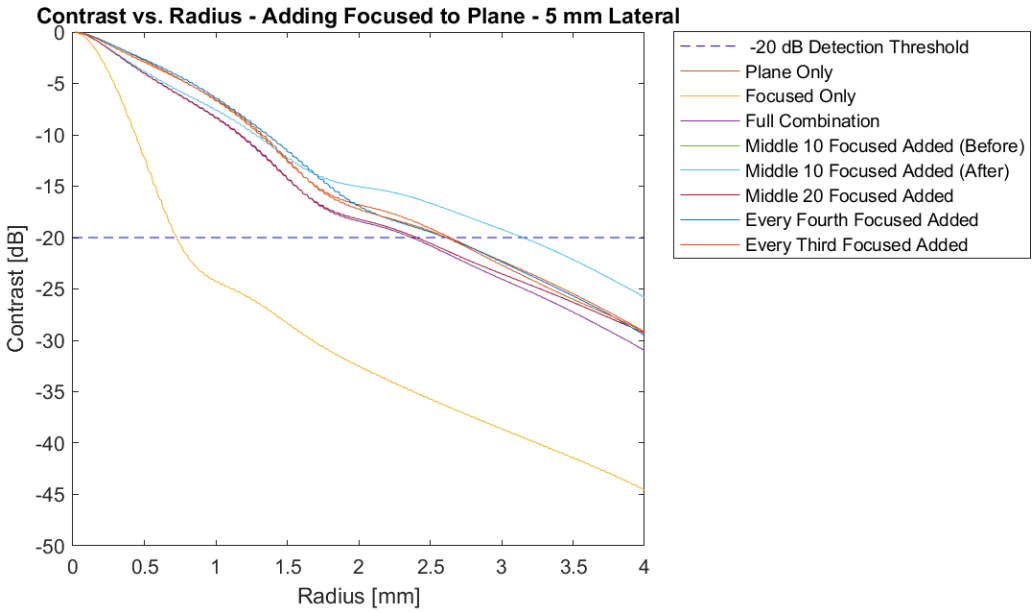

(a) CR Curve - Adding - Unweighted

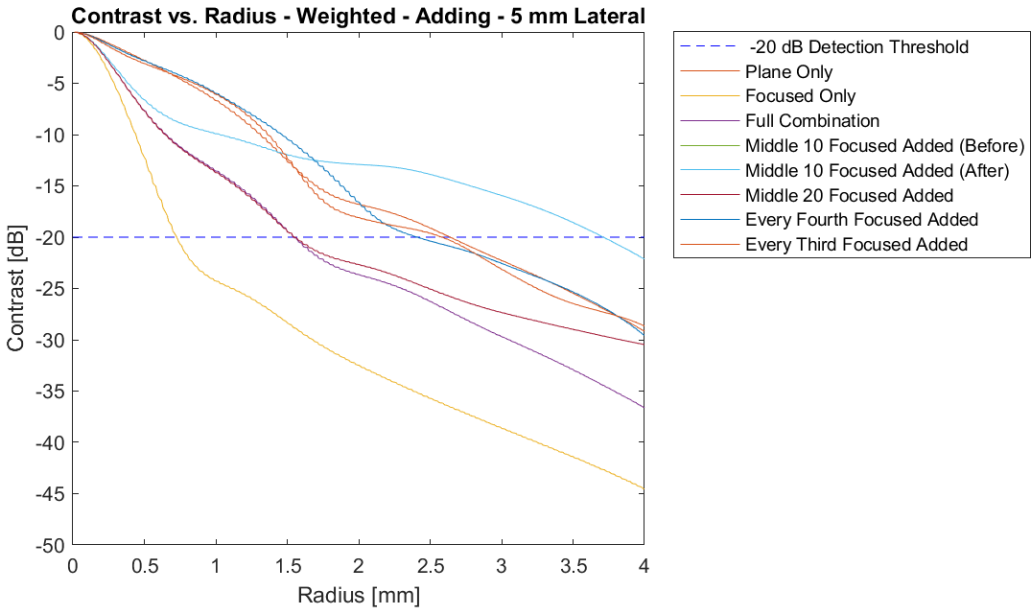

(b) CR Curve - Adding - Weighted

Figure 3.40: Mixed Sequences - Lateral - CR Curves - Adding - Unweighted (top) and weighted (bottom)

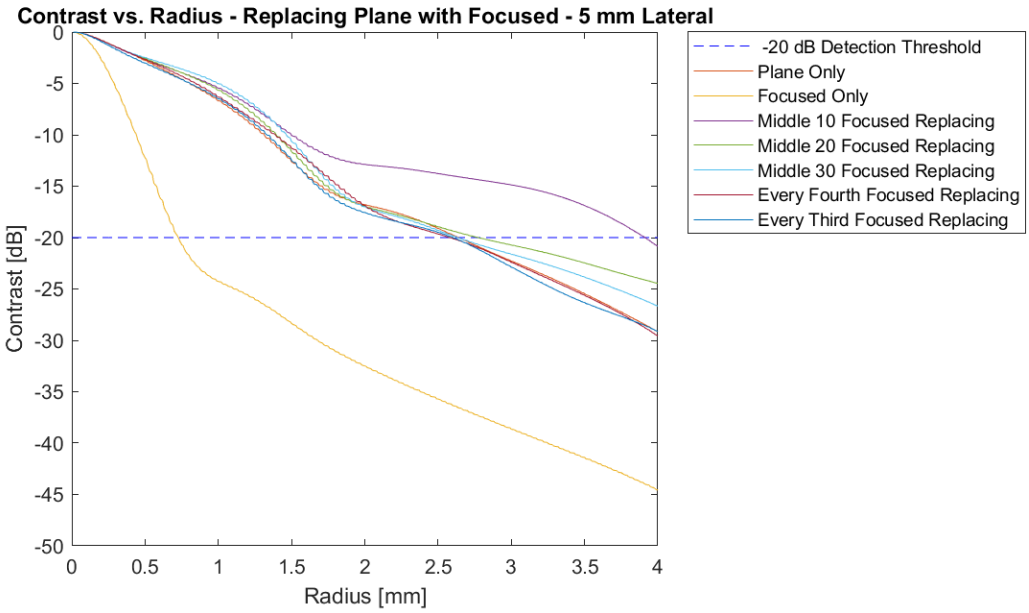

(a) CR Curve - Replacing - Unweighted

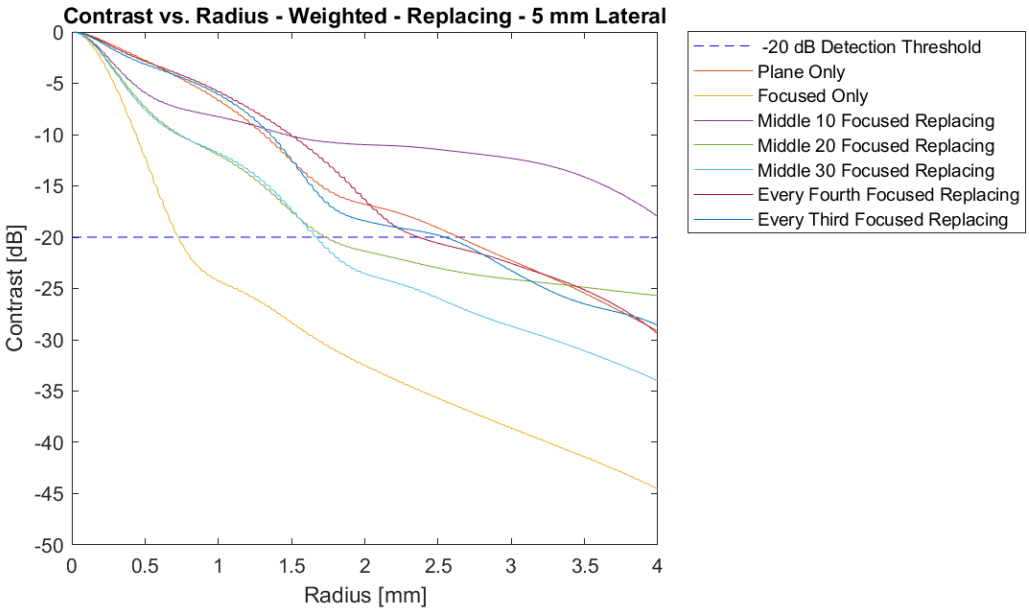

(b) CR Curve - Replacing - Weighted

Figure 3.41: Mixed Sequences - Lateral - CR Curves - Replacing - Unweighted (top) and weighted (bottom)

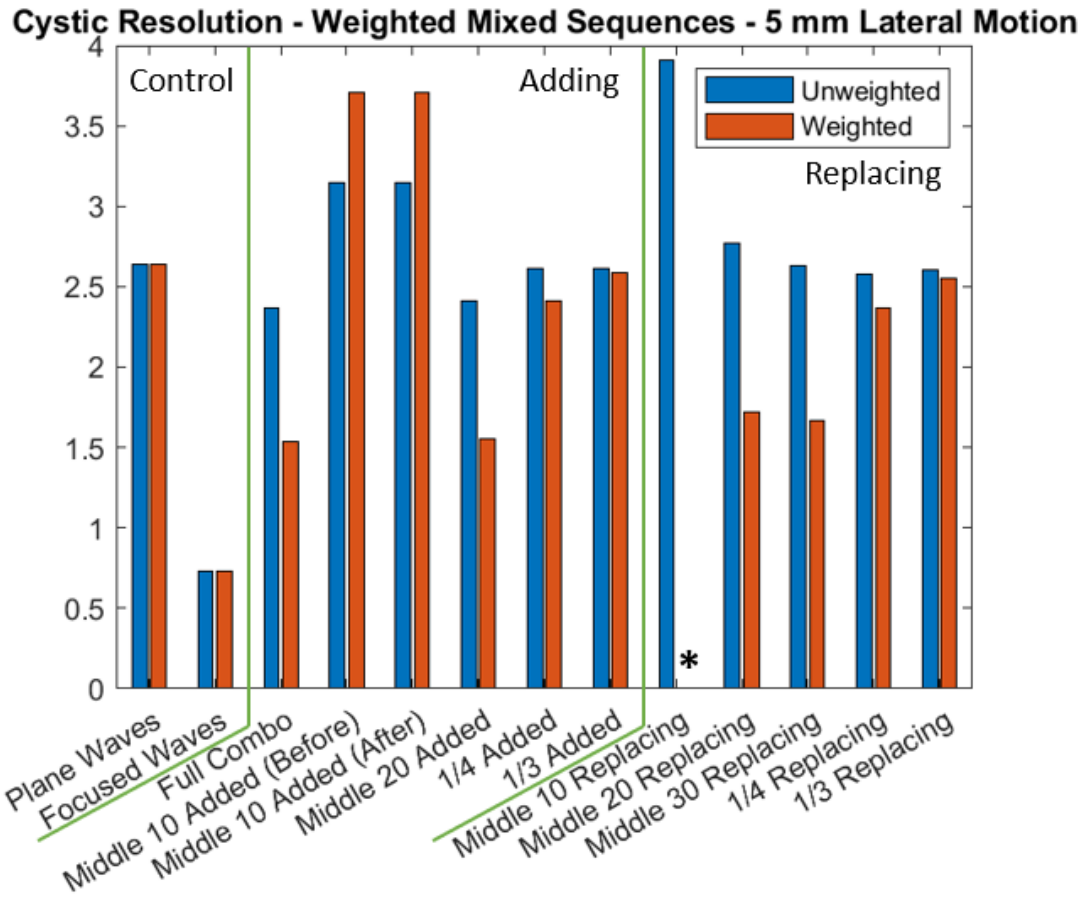

Figure 3.42: Mixed Sequences - Cystic Resolution - Unweighted and Weighted - Controls and all mixture cases shown - *cystic contrast did not drop below -20 dB before 4 mm, so no cystic resolution value is available

In addition to evaluating the contour plots, CR curves, and cystic resolution plots from weighted sequences when imaging **lateral** motion, the same outputs are considered when imaging **axial** motion. First, both control PSFs are shown in Figure 3.43: 1 mm/frame axial motion imaged with (a) plane waves and (b) focused waves. Neither control image has weighting applied. Together, they confirm that focused waves resolve axial motion better than plane waves and that axial motion can produce drastic image degradation.

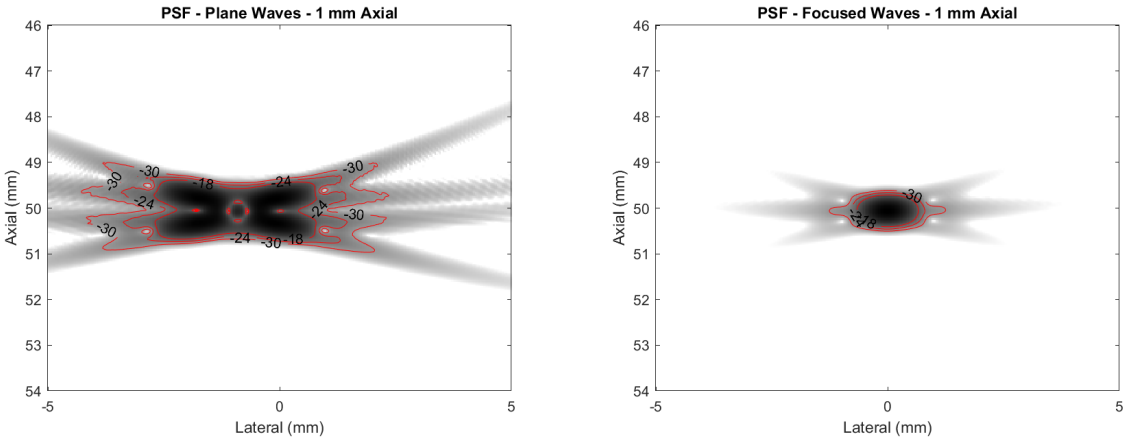

(a) 1 mm/frame - Axial - Plane

(b) 1 mm/frame - Axial - Focused

Figure 3.43: Mixed Sequences - Control Images - 1 mm/frame Axial Motion - REFoCUS

In the same way as before, the contour plots for three mixed sequences are compared to the control PSFs (Figure 3.44). Unweighted mixed sequences are shown in the left column and their corresponding weighted contour plots are shown on the right for three key mixed sequences: 'middle 20 added,' 'middle 20 replacing,' and 'every fourth replacing.' Previously, the every fourth replacing case produced texture differences in side lobes when imaging lateral motion. Now, this motion case produces noticeable lobes in the axial direction. Despite this, weighting this case still reduces off axis energy substantially. Of particular note in this figure, however, are Figures 3.44b and 3.44d. Image degradation is reduced significantly and energy is localized to the center of each PSF quite well.

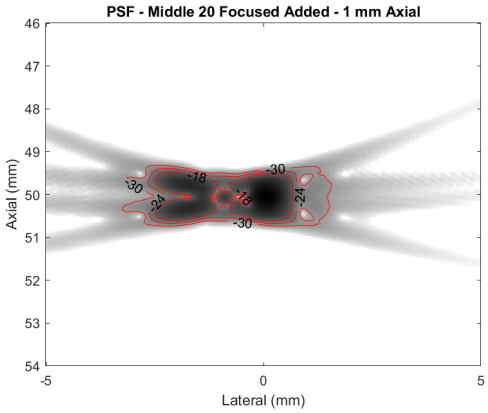

(a) Axial - Middle 20 Added

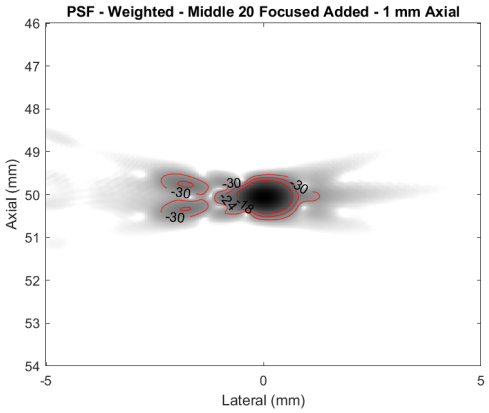

(b) Axial - Middle 20 Added - Weighted

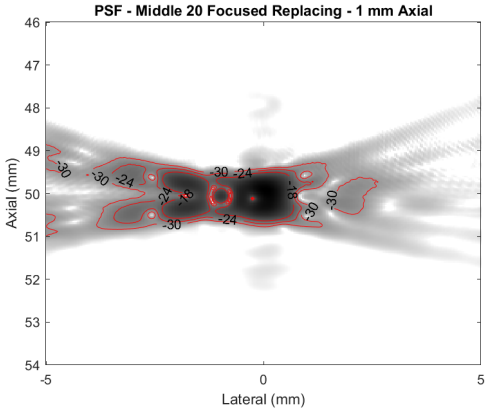

(c) Axial - Middle 20 Replaced

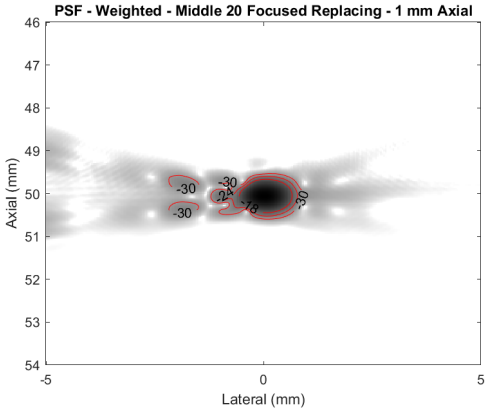

(d) Axial - Middle 20 Replaced - Weighted

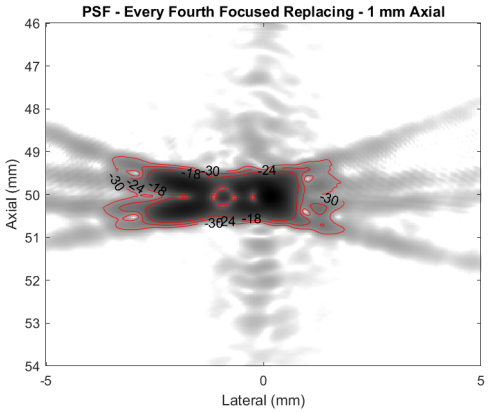

(e) Axial - Every Fourth Replaced

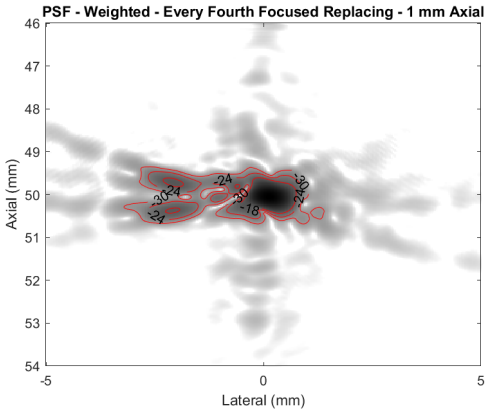

(f) Axial - Every Fourth Replaced - Weighted

Figure 3.44: Mixed Sequences - Axial - Contour Plots - Three mixing cases shown: middle 20 focused added, middle 20 focused replacing plane, and every fourth focused replacing plane

Next, the CR curves for all 'adding' cases are shown when unweighted (Figure 3.45a) and when weighted (Figure 3.45b). Matching the behavior of lateral motion, unweighted mixed sequences do not resolve axial motion better than plane waves. In contrast, the same two weighted mixed sequences, middle 20 added and full combination, math the focused CR curve more closely. When considering the unweighted and weighted 'replacing' mixed sequence CR curves in Figures 3.46a and 3.46b, consistent trends are, again, observed. Weighting the middle 20 and middle 30 replacing sequences provides significant reduction in degradation.

The axial results from the CR curves are confirmed by plotting cystic resolution for every sequence (Figure 3.47). The left section shows the control sequences, the middle section shows the 'adding' sequences, and the right section shows the 'replacing' sequences. Here, four mixed sequences improve cystic resolution in the presence of axial motion: full combo, middle 20 added and replacing, and middle 30 replacing.

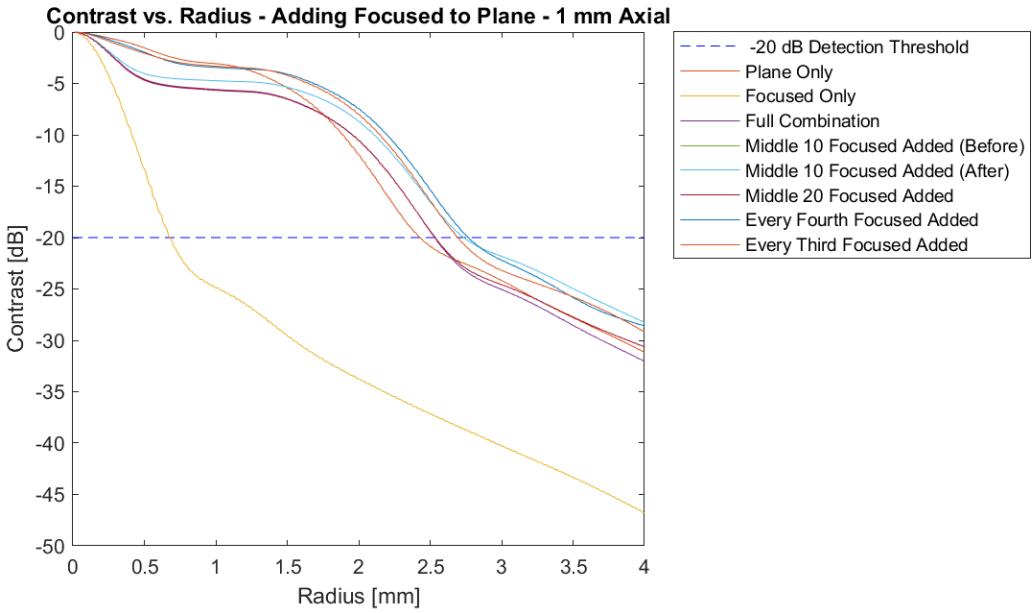

(a) CR Curve - Adding - Unweighted

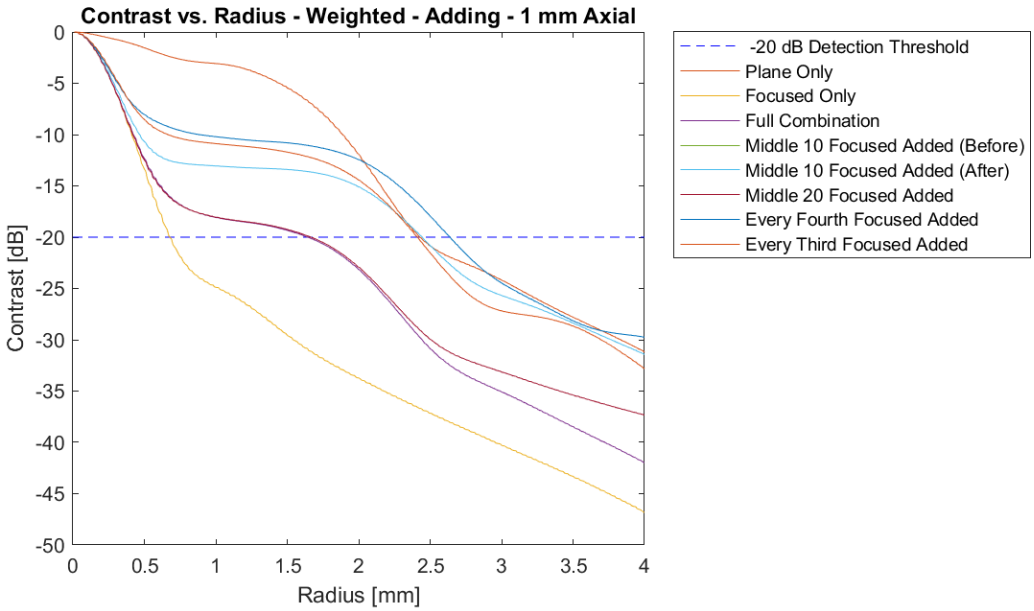

(b) CR Curve - Adding - Weighted

Figure 3.45: Mixed Sequences - Axial - CR Curves - Adding - Unweighted (top) and weighted (bottom)

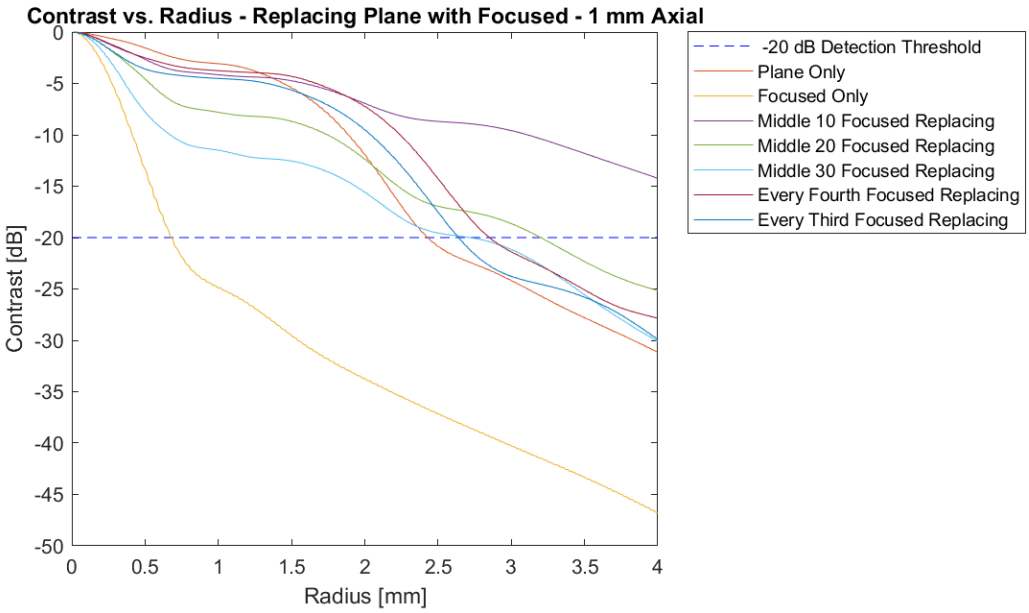

(a) CR Curve - Replacing - Unweighted

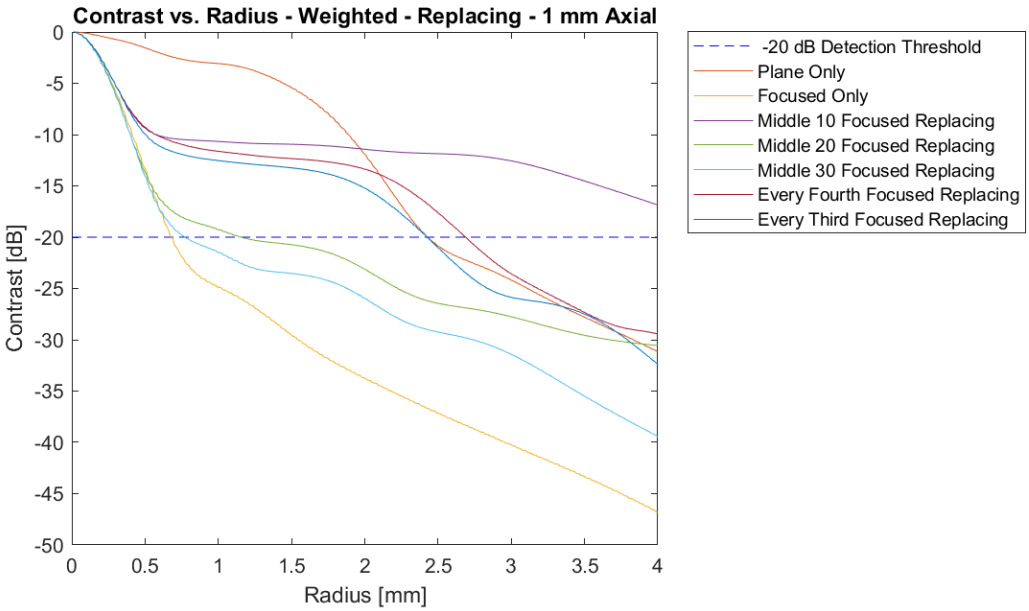

(b) CR Curve - Replacing - Weighted

Figure 3.46: Mixed Sequences - Axial - CR Curves - Replacing - Unweighted (top) and weighted (bottom)

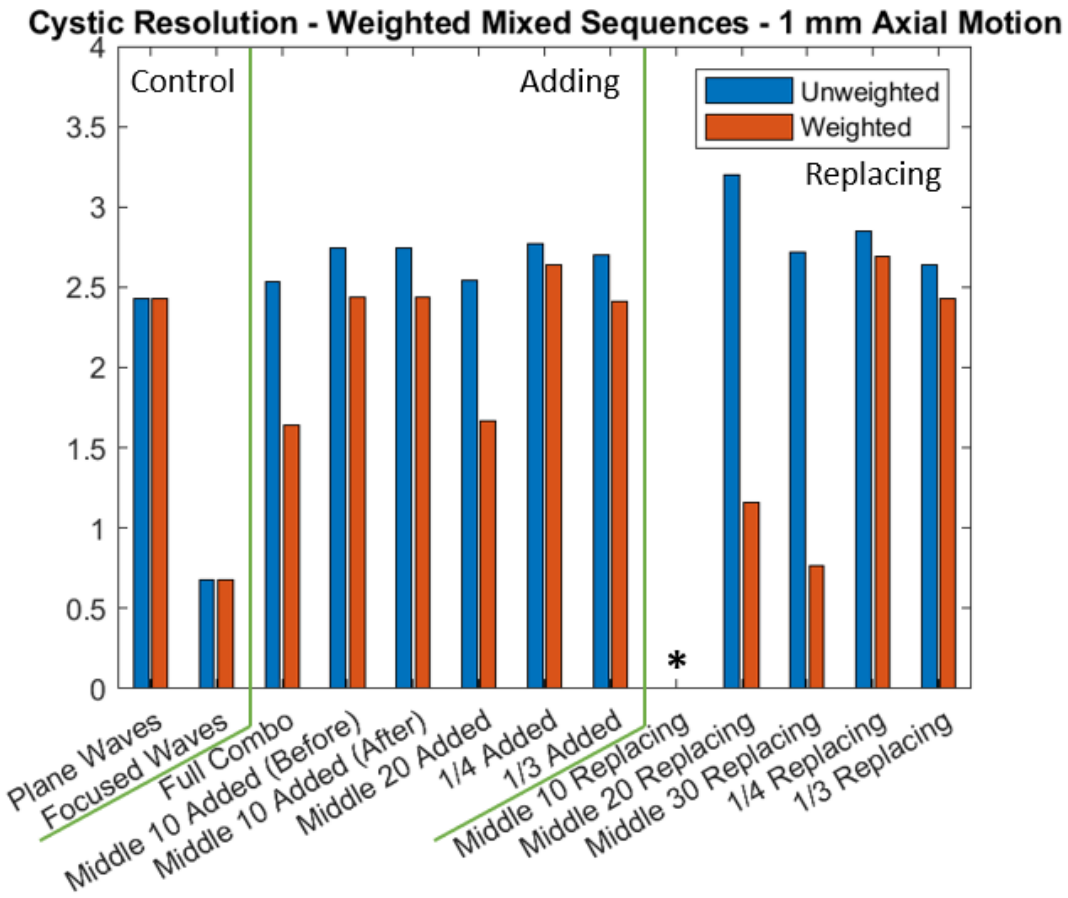

Figure 3.47: Mixed Sequences - Cystic Resolution - Unweighted and Weighted - Controls and all mixture cases shown - *cystic contrast did not drop below -20 dB before 4 mm, so no cystic resolution value is available

3.2.3 Speckle Phantom - Weighted Mixed Sequences - Image Uniformity

Six mixed sequences of interest were used to image cyst targets in a speckle phantom. Control images are required to determine whether or not these mixed sequences influence speckle patterns and overall image uniformity. Figure 3.48 shows these control images; both are unweighted and beamformed with REFoCUS. The left shows the phantom imaged with plane waves and the right shows the phantom imaged with focused waves. Furthermore, the caption of each image specifies the number of transmissions, which varies in certain 'adding' mixed sequences. Generally, speaking

the two images are very similar. Focused waves achieve slightly improved depth penetration, which is to be expected with the focus set to 60 mm. This depth penetration is primarily observable via the improved contrast in the hyper-echoic lesion at approximately (40,60). For all cysts imaged, image quality is comparable. The blurred lines in the bottom corners of both images are beyond the relevant field of view and would be masked off in a clinical setting.

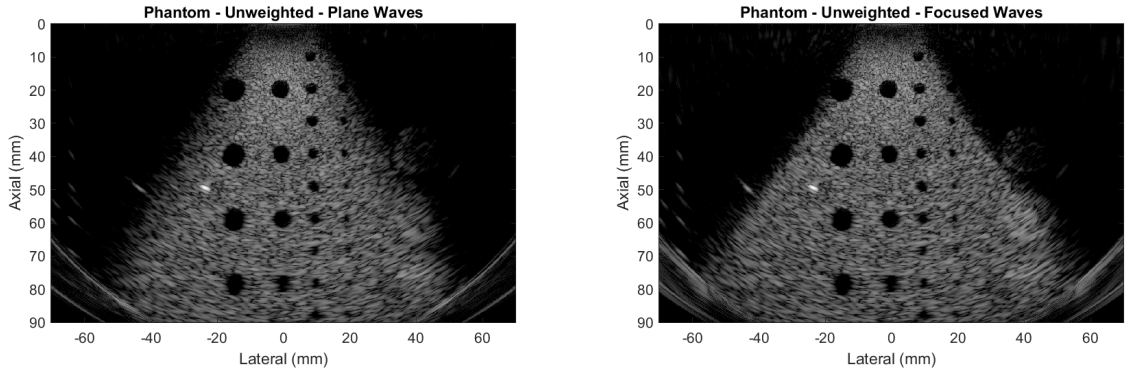

(a) Plane Waves (n=121)

(b) Focused Waves (n=121)

Figure 3.48: Speckle Phantom - Cyst Targets - Control Images - Unweighted

Comparisons to these control images are shown in Figure 3.49. The mixed sequences here are (a) middle 20 added, (b) middle 20 replaced, (c) full combination, (d) middle 30 replaced, (e) every fourth added, and (f) every fourth replaced (adding on left, replacing on right). Note that the total number of transmissions for all adding sequences is increased from $n = 121$. Very slight differences in these images can be observed, related to the number of focused transmissions used in each sequence, since focused waves penetrate more effectively. Similarly, sequences that have more total transmissions have better SNR at depth. Again, both of these behaviors can be seen best via the hyper-echoic lesion at (40,60). Recall, however, the tradeoff between spatial resolution and frame-rate. An increased number of transmissions, or using more focused transmissions, may improve resolution, but it will also reduce the maximum achievable frame-rate.

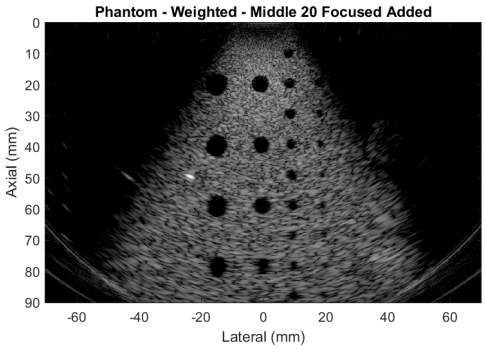

(a) Middle 20 Added (n=141)

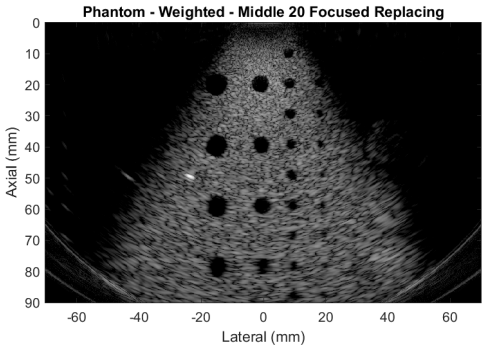

(b) Middle 20 Replaced (n=121)

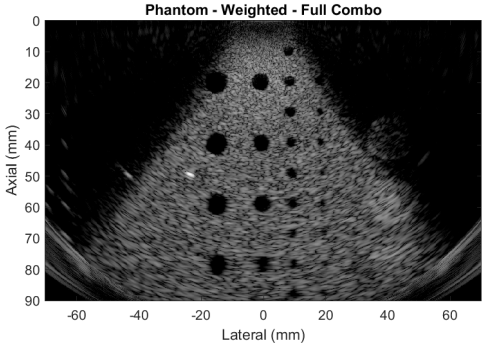

(c) Full Combination (n=242)

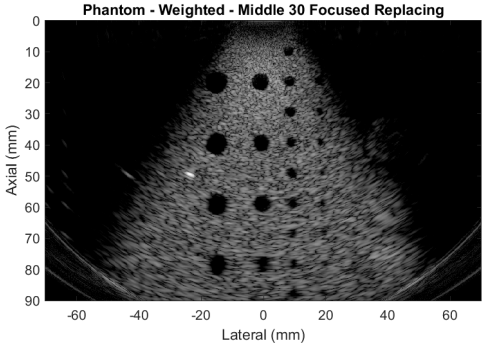

(d) Middle 30 Replaced (n=121)

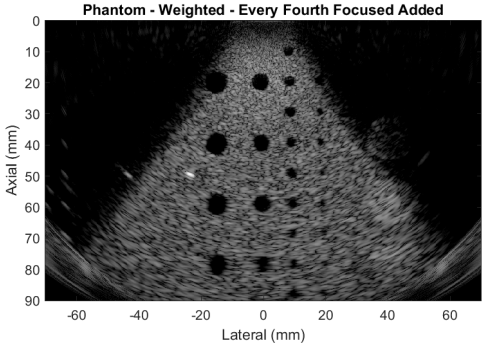

(e) Every Fourth Added (n=152)

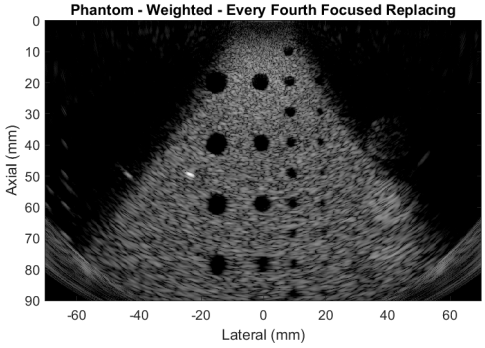

(f) Every Fourth Replaced (n=121)

Figure 3.49: Speckle Phantom - Mixed Sequences - Number of transmissions required to generate each image specified - Speckle pattern unaffected

Crucially, speckle pattern and image uniformity are both **unaffected** by mixed sequences. Neither replacing large portions of center of the sequence with focused transmissions nor interspersing focused transmissions throughout the sequence affects the speckle pattern. Furthermore, all cyst targets in these images are resolvable to the same degree. Even though Figure 3.49 does not offer quantitative outputs, it clearly highlights that a motion-specific sequence will not sacrifice image quality in the full field of view.

Chapter 4

Discussion

4.1 Transmission Order in Mixed Sequences

Here, speckle is unaffected by beamforming methods and mixed sequences. Uniformity of speckle pattern for different mixed sequences is verified in Figure 3.49. Furthermore, two mixed sequences were implemented in order to evaluate the effects of transmission order when combined as RF data. The middle 10 focused transmissions were added to the full plane sequence both before and after the the plane sequence. Crucially, these 10 focused transmissions were taken at the **same time**. Transmission order, as it relates to the position of the point target, would certainly have an impact on the final image. Rather, these results pertain to transmission order within the combined RF data matrix. As shown by the 4^{th} and 5^{th} pairs of bars in Figures 3.21 and 3.28, cystic resolution is unaffected by transmission order. More conclusively, the contour plots of both PSFs are identical, as shown here in Figure 4.1. The same holds true for axial motion.

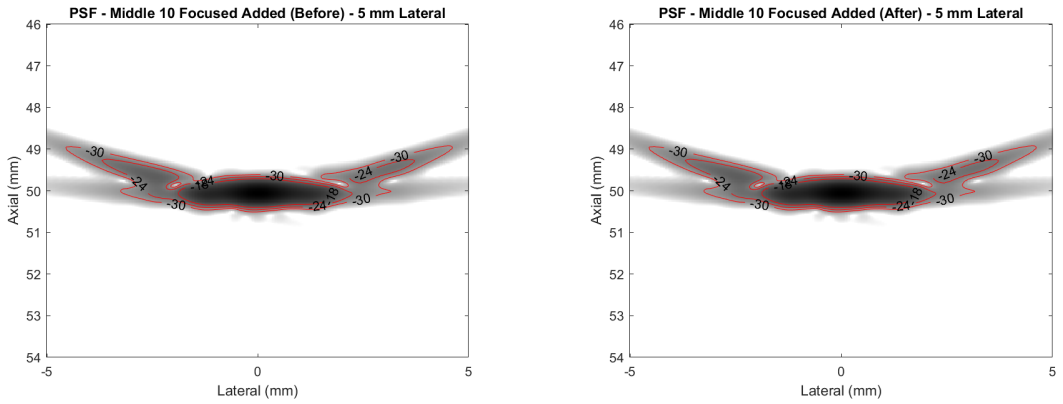

(a) Middle 10 Added - Before

(b) Middle 10 Added - After

Figure 4.1: Middle 10 Focused Transmissions Added - Before and After

4.2 Degradation Behavior in the Presence of Motion

It has been previously established that both lateral and axial motion produce lateral degradation in an ultrasound PSF [36]. The literature is unclear, however, on how the direction of motion influences the direction of degradation. The evaluation of motion sensitivity in this work reveals consistent trends. Shown in Figure 3.1, imaging lateral motion with plane waves produces lateral degradation on both sides of the PSF with side lobes that towards the transducer. In contrast, imaging the same lateral motion of a point target away from the focal point of focused transmissions ('off-focus') produces side lobes that curve away from the transducer (Figure 3.3). Even though the off-focus case begins to behave more like a plane wave transmission, the side lobes curve in the opposite direction. This inverse behavior is observed with axial motion as well. Figures 3.8 and 3.10 show the PSF from imaging a point target moving axially with plane and off-focus waves, respectively. In the plane case, degradation is located to the left of the PSF, whereas in the off-focus case it is located to the right of the PSF, albeit less prominent.

The same trends hold true when the direction of motion is reversed. Figure 3.15 shows that imaging a point target moving from right to left (previously, left to right) produces side lobes that curve *away* from the transducer. The same motion case, then, imaged in the off-focus case produces

side lobes that curve towards the transducer (Figure 3.17). When considering axial motion in the opposite direction (up to down instead of down to up) the location of degradation is also reversed. In Figure 3.22, the degradation due to motion is observed to the right of the PSF, and in Figure 3.24 the slight degradation is visible to the left of the PSF.

Overall, the location of motion-induced degradation is highly dependent on direction of motion. This directional dependence is also related to the direction of the scan sweep. In this work, all scans were conducted from left to right. Scanning from right to left would likely reverse all of the previously described behaviors yet again, but this hypothesis was not investigated. Despite the fact that the direction of motion affects PSF shape, it appears to have minimal influence on final image quality, as quantified by cystic resolution. Figure 3.21 shows that cystic resolution is reduced slightly when the direction of the scan sweep is opposite that of point target motion, but this trend only observed for plane waves. Focused waves are predominantly unaffected by direction of lateral motion. The same holds true for all transmit waveforms when imaging axial motion (Figure 3.28). This behavior of degradation in the presence of motion emphasizes the importance of being able to resolve motion.

4.3 Inherent Masking with REFoCUS

One of the primary differences between virtual source and REFoCUS beamforming is that virtual source depends on geometric masks to reject echoes not received from the virtual source (Figure 1.2). REFoCUS, which isolates individual elements' contributions to any given pixel, does not apply explicit masking but still achieves inherent masking. The reason for this similarity is that both beamforming techniques encode transmit waveform geometry in different ways. Again, virtual source beamforming applies spatial masks, but REFoCUS considers applied transmit delays. Regardless of how the transmit pressure field is arranged during beamforming, the transmit waveform geometries, and therefore transmit delays, are the same.

The effects of masking are illustrated in Figure 3.9. In the virtual source case (left), the PSF was maintained as velocity increased because echoes from the moving point target were only

accepted when they came from within a narrow region of the applied mask. In the case of REFoCUS (right), echoes from the moving point target only contributed to the PSF when they were received correct time, as determined by the removal of delays in the frequency domain.

The lack of an explicit mask during REFoCUS beamforming is rarely problematic, but it does generate image artifacts on the edges of some scans. This behavior is shown in Figure 3.49. The blurring on the bottom corners of these images comes from off-axis echoes that are not rejected by a geometric mask and are not perfectly removed during the pseudoinversion process. These artifacts are, however, only observed on the extreme edges of images produced with REFoCUS and could easily be masked off in a clinical setting (with a mask that does not depend on sequence type) following image reconstruction.

Ultimately, it is highly beneficial that REFoCUS beamforming exhibits effective masking. Not only does REFoCUS free the operator from having to design masks (window size and type), but it also allows the spatial properties of different transmit waveforms to be utilized. If REFoCUS did not maintain a certain amount of masking, focused waves would have heightened sensitivity to motion when beamformed with REFoCUS. As it stands, REFoCUS is a viable beamforming technique for sequences designed to better resolve motion in cardiac ultrasound.

4.4 Relationship Between Resolution and Frame-Rate

In order to improve spatiotemporal resolution in cardiac ultrasound without sacrificing frame-rate, the capability of mixed sequences to resolve motion at clinically relevant depths was investigated. Figures 3.42 and 3.47 show the cystic resolution values achievable with mixed sequences when imaging 5 mm of lateral motion per frame and 1 mm of axial motion per frame, respectively. The first two sets of bars in these figures are the baselines to which mixed sequences are compared, being plane and focused transmissions beamformed with REFoCUS. The plane case gives the minimum cystic resolution to be considered a viable mixed sequence, and the focused case gives the best-case-scenario cystic resolution for any combination of plane and focused transmissions. Several mixed sequences show noticeable improvements over the plane wave case: full combination (n=256),

middle 20 added (n=148), middle 20 replacing (n=128), and middle 30 replacing (n=128). These mixed sequences also all generate uniform images when used to image large, speckle-generating regions of interest (Figure 3.49).

With any mixed sequence, the number of transmissions required to generate an image must be considered. Mixed sequences that add transmissions increase the total number of transmissions, thereby reducing frame-rate. In this instance, 128 focused transmissions can adequately cover the region of interest and resolve motion. Thus, a fully focused sequence would be the best option. That being said, it is possible that a sequence with fewer total transmissions would perform better by incorporating plane waves to broadly insonify stationary tissue and focused waves to resolve areas of significant motion.

Also paramount when implementing a mixed sequence is the location of motion in the field of view. Mixed sequences that rely upon replacing plane transmissions with focused transmissions successfully improve cystic resolution because the transmissions that are replaced are the transmissions that insonified the moving point target. Simply put, mixed sequences will work the best when focused transmissions are used to image regions exhibiting motion. Two strategies to ensure this are immediately apparent: (1) design sequences for specific views of the heart and (2) utilize motion tracking techniques to dynamically determine the location of motion and adjust the mixed sequence accordingly. The first solution is simple but, given that echocardiography relies on prescribed views of the heart, may prove feasible. The second solution, meanwhile, would be more difficult to implement but also much more robust. An adaptable mixed sequence would be much more reliable, especially since patient physiology varies dramatically.

4.5 Conclusions

This work has shown that weighted mixed sequences have the potential to improve spatial resolution in cardiac imaging without sacrificing frame-rate. Specifically, REFoCUS, an element-based beamforming method, was shown to perform consistently when imaging motion through both simulations and experimental validation. REFoCUS also retains the spatial encoding from

transmit geometry despite not applying spatial masking. This spatial encoding is useful when combining transmissions of different types in a mixed sequence; a process that REFoCUS is well suited for. The two transmit geometries investigated were plane and focused waves. Generally, plane waves image wide regions efficiently, resulting in high frame-rate, but are more susceptible to motion-induced degradation. Focused waves resolve motion more effectively but have reduced line width, thereby limiting frame-rate. Mixed sequences incorporate the beneficial aspects of plane and focused transmissions when focused transmissions are weighted more heavily. Without weighting, sequences combining plane and focused waves behave predominantly like plane wave sequences. Here, mixed sequences have been presented that integrate plane waves and focused waves, resolve lateral and axial motion, and do not degrade image uniformity.

4.6 Future Work

Weighted mixed sequences have been shown to improve cystic resolution compared to plane wave imaging, but focused sequences still perform better. That being said, the inclusion of plane waves in a mixed sequence may provide advantages in temporal resolution. Further evaluation of mixed sequences is required to determine the feasibility of matching the spatial resolution of a modern cardiac ultrasound with fewer transmissions. This ideal mixed sequence will require a strategy for locating motion in the field of view. Whether sequences are designed for specific views of the heart or with dynamic motion tracking, identifying regions of motion will enable the accurate aiming of focused transmissions. Moreover, only a single weighting scheme was investigated in this work. Refining the weighting of plane and focused waves may further enhance the capabilities of mixed sequences. It is also possible to apply spatially distributed weighting after beamforming.

In addition, images from a more dynamic environment are required. In theory, a phantom could be simulated with a moving target and speckle throughout. However, generating speckle in Field II is computationally intensive and a moving point target cannot emulate the complex motion observed in the heart. Ultimately, imaging the heart, *in-vivo*, will provide strong evidence for the potential of mixed sequences to better resolve cardiac motion and maintain frame-rate.

Bibliography

[1] Rehman Ali, Carl D. Herickhoff, Dongwoon Hyun, Jeremy J. Dahl, and Nick Bottenus. Extending retrospective encoding for robust recovery of the multistatic data set. IEEE Transactions on Ultrasonics, Ferroelectrics, and Frequency Control, 67:943–956, 5 2020.

[2] Islam Aly, Asad Rizvi, Wallisa Roberts, Shehzad Khalid, Mohammad W. Kassem, Sonja Salandy, Maira du Plessis, R. Shane Tubbs, and Marios Loukas. Cardiac ultrasound: An anatomical and clinical review, 1 2021.

[3] Jon-Austin Ash and Yuvraj S. Chowdhury. Pediatric echocardiography assessment, protocols, and interpretation, 12 2021.

[4] Philippe B. Bertrand, Robert A. Levine, Eric M. Isselbacher, and Pieter M. Vandervoort. Fact or artifact in two-dimensional echocardiography: Avoiding misdiagnosis and missed diagnosis, 5 2016.

[5] Bart H. Bijnens, Maja Cikes, Piet Claus, and George R. Sutherland. Velocity and deformation imaging for the assessment of myocardial dysfunction, 2009.

[6] Nick Bottenus. Comparison of virtual source synthetic aperture beamforming with an element-based model. The Journal of the Acoustical Society of America, 143:2801–2812, 5 2018.

[7] Nick Bottenus. Recovery of the complete data set from focused transmit beams. IEEE Transactions on Ultrasonics, Ferroelectrics, and Frequency Control, 65:30–38, 1 2018.

[8] Christian Bruch, Joerg Stypmann, Matthias Grude, Rainer Gradaus, Günter Breithardt, and Thomas Wichter. Tissue doppler imaging in patients with moderate to severe aortic valve stenosis: Clinical usefulness and diagnostic accuracy. American Heart Journal, 148:696–702, 10 2004.

[9] Jeffrey S.K. Chan, Gary Tse, H. Zhao, X. X. Luo, C. N. Jin, Kevin Kam, Y. T. Fan, and Alex P.W. Lee. Echocardiography update for primary care physicians: A review, 2 2020.

[10] Maja Cikes, Ling Tong, George R Sutherland, and Jan D'hooge. Ultrafast cardiac ultrasound imaging technical principles, applications, and clinical benefits, 2014.

[11] M R Cowie, A Mosterdft, D A Wood, J W Deckers, P A Poole-Wilson, G C Sutton, and D E Grobbeef. The epidemiology of heart failure, 1997.

[12] Libertario Demi. Practical guide to ultrasound beam forming: Beam pattern and image reconstruction analysis, 9 2018.

[13] Torbjørn Hergum, Tore Bjåstad, Kjell Kristoffersen, and Hans Torp. Parallel beamforming using synthetic transmit beams. IEEE Transactions on Ultrasonics, Ferroelectrics, and Frequency Control, 54:271–279, 2 2007.

[14] Jorgen Arendt Jensen. Field: A program for simulating ultrasound systems, 1996.

[15] Jrgen Arendt Jensen and Niels Bruun Svendsen. Calculation of pressure fields from arbitrarily shaped, apodized, and excited ultrasound transducers. IEEE Transactions on Ultrasonics, Ferroelectrics, and Frequency Control, 39:262–267, 1992.

[16] Mustafa Karaman, Hasan Bilge, and Matthew O'Donnell. Adaptive multi-element synthetic aperture imaging with motion and phase aberration correction. IEEE Transactions on Ultrasonics, Ferroelectrics, and Frequency Control, 45:1077–1087, 1998.

[17] Alexander L. Klibanov and John A. Hossack. Ultrasound in radiology: From anatomic, functional, molecular imaging to drug delivery and image-guided therapy, 9 2015.

[18] Ateet Kosaraju, Amandeep Goyal, Yulia Grigorova, and Amgad N. Makaryus. Left ventricular ejection fraction, 7 2021.

[19] Huong T. Le, Nicholas Hangiandreou, Robert Timmerman, Mark J. Rice, W. Brit Smith, Lori Deitte, and Gregory M. Janelle. Imaging artifacts in echocardiography, 3 2016.

[20] T. Douglas Mast, Laura M. Hinkelman, Leon A. Metlay, Michael J. Orr, and Robert C. Waag. Simulation of ultrasonic pulse propagation, distortion, and attenuation in the human chest wall. The Journal of the Acoustical Society of America, 106:3665–3677, 12 1999.

[21] Sophie I. Mavrogeni, Flora Bacopoulou, George Markousis-Mavrogenis, George Chrousos, and Evangelia Charmandari. Cardiovascular imaging in obesity, 3 2021.

[22] Alaa A. Mohamed, Ahmed A. Arifi, and Ahmed Omran. The basics of echocardiography. Journal of the Saudi Heart Association, 22:71–76, 4 2010.

[23] Douglas C. Montgomery, Elizabeth A. Peck, and G. Geoffrey Vining. Introduction to linear regression analysis, 2012.

[24] Alexander Ng and Justiaan Swanevelder. Resolution in ultrasound imaging. Continuing Education in Anaesthesia, Critical Care and Pain, 11:186–192, 2011.

[25] Nghia Q. Nguyen and Richard W. Prager. High-resolution ultrasound imaging with unified pixel-based beamforming. IEEE Transactions on Medical Imaging, 35:98–108, 1 2016.

[26] Svetoslav Ivanov Nikolov, Jacob Kortbek, and Jørgen Arendt Jensen. Practical applications of synthetic aperture imaging. 2010.

[27] Ammar A. Oglat, M. Z. Matjafri, Nursakinah Suardi, Mohammad A. Oqlat, Mostafa A. Abdelrahman, and Ahmad A. Oqlat. A review of medical doppler ultrasonography of blood flow in general and especially in common carotid artery. Journal of Medical Ultrasound, 26:3–13, 1 2018.

[28] Karthik Ranganathan and William F. Walker. Cystic resolution: A performance metric for ultrasound imaging systems. IEEE Transactions on Ultrasonics, Ferroelectrics, and Frequency Control, 54:782–792, 2007.

[29] Morten Fischer Rasmussen and Jorgen Arendt Jensen. 3-d ultrasound imaging performance of a row-column addressed 2-d array transducer: A measurement study. pages 1460–1463, 2013.

[30] Véronique L. Roger. Epidemiology of heart failure: A contemporary perspective. Circulation Research, pages 1421–1434, 2021.

[31] Andrzej Smereczyński, Katarzyna Kołaczyk, and Elżbieta Bernatowicz. Chest wall – underappreciated structure in sonography. part i: Examination methodology and ultrasound anatomy. Journal of Ultrasonography, 17:197–205, 9 2017.

[32] L Sun, C Ma, S Liu, L Zou, and D Jia. Mitral annular tissue velocity in the diagnosis of coronary artery disease, 2014.

[33] Arco J. Teske, Bart W.L. De Boeck, Paul G. Melman, Gertjan T. Sieswerda, Pieter A. Doevendans, and Maarten J.M. Cramer. Echocardiographic quantification of myocardial function using tissue deformation imaging, a guide to image acquisition and analysis using tissue doppler and speckle tracking, 2007.

[34] Ling Tong, Alessandro Ramalli, Ruta Jasaityte, Piero Tortoli, and Jan D'Hooge. Multi-transmit beam forming for fast cardiac imaging-experimental validation and in vivo application. IEEE Transactions on Medical Imaging, 33:1205–1219, 2014.

[35] M. T. Upton, D. G. Gibson, and D. J. Brown. Instantaneous mitral valve leaflet velocity and its relation to left ventricular wall movement in normal subjects. British Heart Journal, 38:51–58, 1976.

[36] Jing Wang and Jian Yu Lu. Motion artifacts of extended high frame rate imaging. IEEE Transactions on Ultrasonics, Ferroelectrics, and Frequency Control, 54:1303–1315, 7 2007.

[37] Haichong K. Zhang, Alexis Cheng, Nick Bottenus, Xiaoyu Guo, Gregg E. Trahey, and Emad M. Boctor. Synthetic tracked aperture ultrasound imaging: design, simulation, and experimental evaluation. Journal of Medical Imaging, 3:027001, 4 2016.

Appendix A

Data Combination - Virtual Source vs. REFoCUS

The images shown in this Appendix illustrate the effectiveness of combining transmissions for either virtual source or REFoCUS beamforming. Figure A.1 gives the unmixed data sets, which serve as controls. On the left, plane waves used to image 1 mm of axial motion, and on the right, focused waves used to image 1 mm of axial motion. Virtual source beamforming is shown on the top and REFoCUS is shown on the bottom. In Figure A.2, virtual source and REFoCUS are used to both add focused data to plane waves (left) and replace plane data with focused data (right). Note that since combination takes place after virtual source beamforming but before REFoCUS beamforming, virtual source must combine lines of the final image whereas REFoCUS can combine transmission of the RF data.

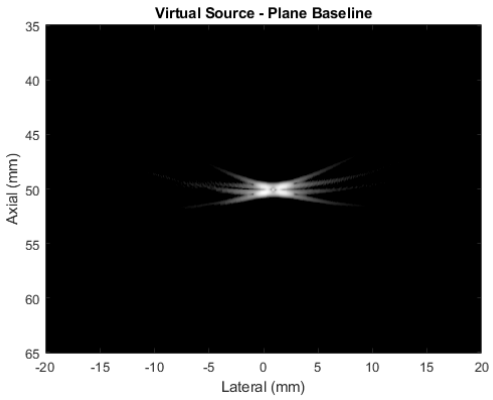

(a) Plane - Virtual Source

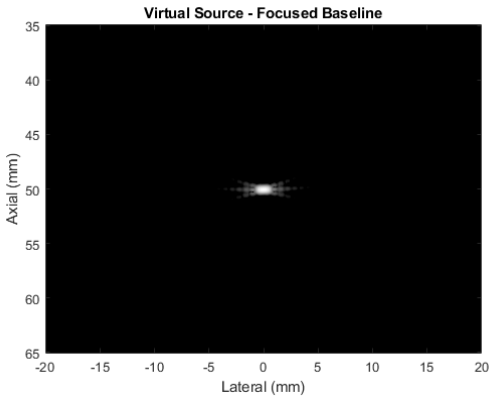

(b) Focused - Virtual Source

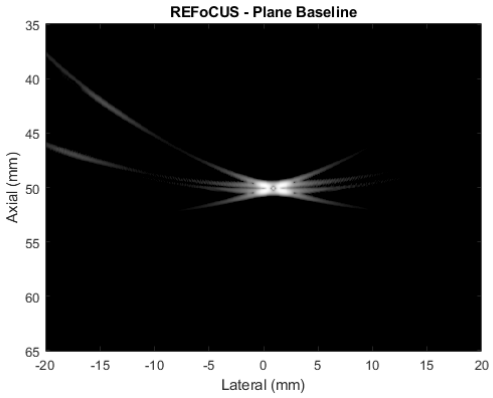

(c) Plane - REFoCUS

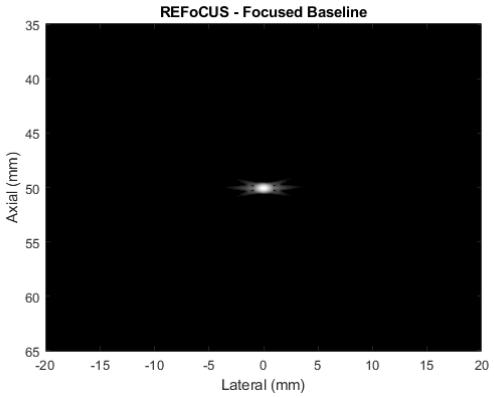

(d) Focused - REFoCUS

Figure A.1: Plane and Focused Baseline PSFs - Virtual Source and REFoCUS - 1 mm Axial Motion

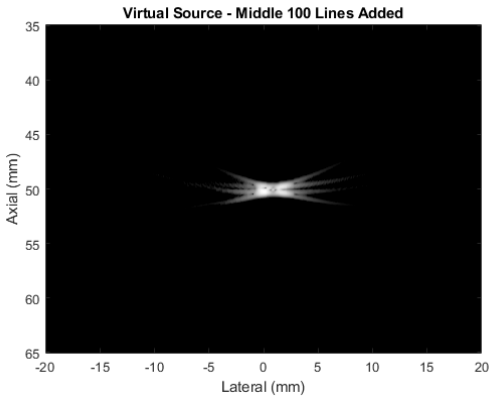

(a) Middle 100 Added - Virtual Source

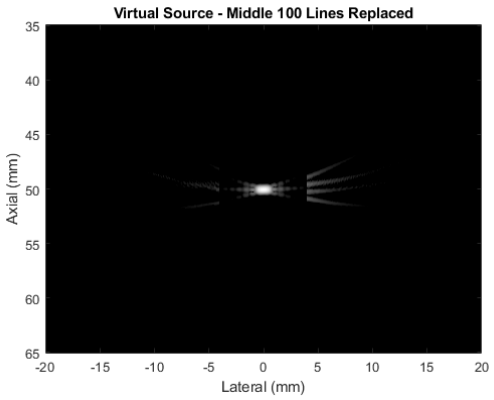

(b) Middle 100 Replaced - Virtual Source

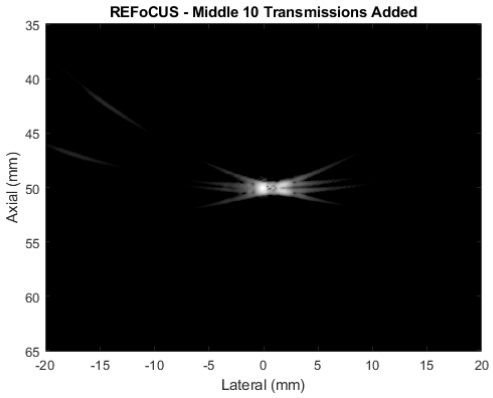

(c) Middle 10 Added - REFoCUS

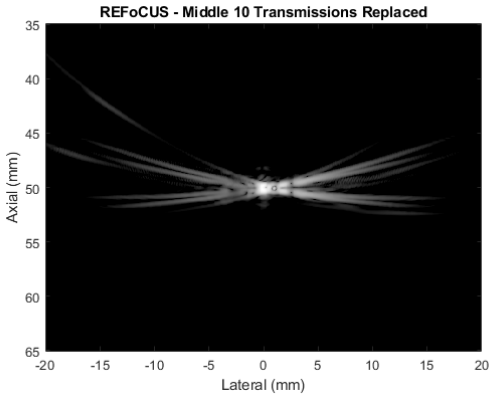

(d) Middle 10 Replaced - REFoCUS

Figure A.2: Plane and Focused Baseline PSFs - Virtual Source and REFoCUS - 1 mm Axial Motion - Note that virtual source added/replaced the middle 100 lines of beamformed data, whereas REFoCUS added/replaced the middle 10 transmissions of RF data

Appendix B

Delay Matrices for Mixed Sequences

The delay matrices used to confirm proper data combination are shown in this Appendix. First, the delays for a plane wave and focused wave sequence are shown (Figure B.1). Next, Figures B.2 and B.3 show the delay matrices when 'adding' and 'replacing' transmissions, respectively. For all combined delay matrices, values are normalized to the maximum delay.

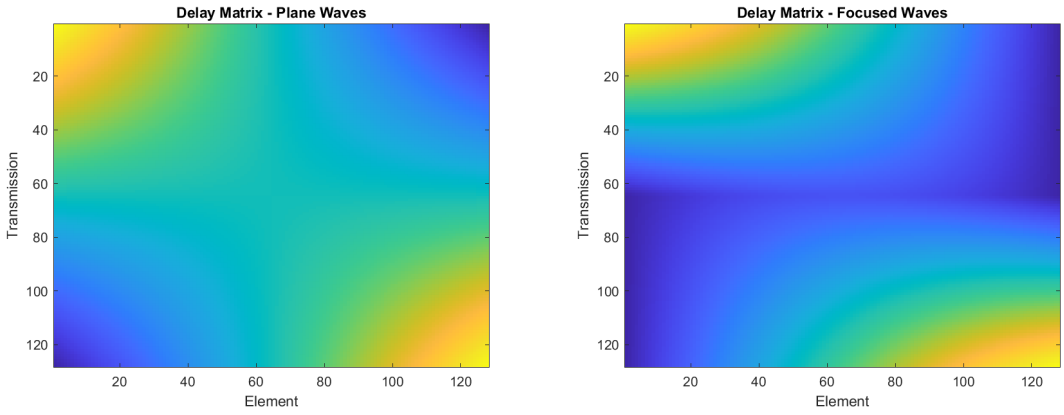

(a) Plane (n=128)

(b) Focused (n=128)

Figure B.1: Delay Matrices - Plane and Focused

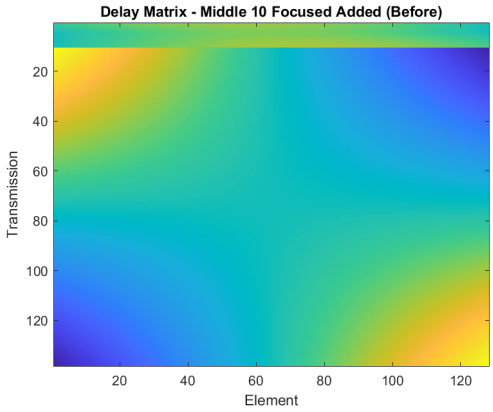

(a) Middle 10 Added Before (n=138)

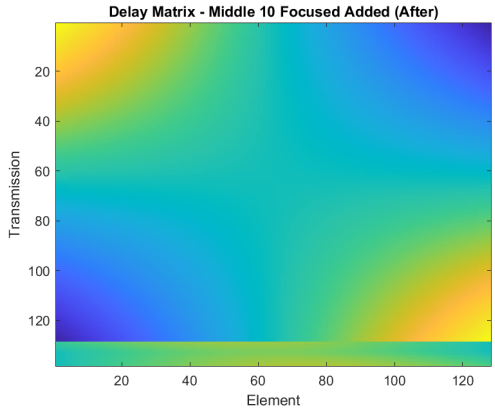

(b) Middle 10 Added After (n=138)

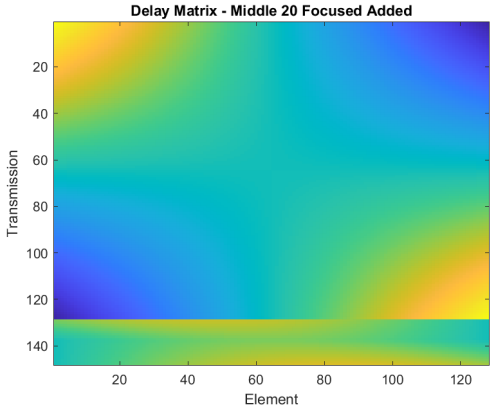

(c) Middle 20 Added (n=148)

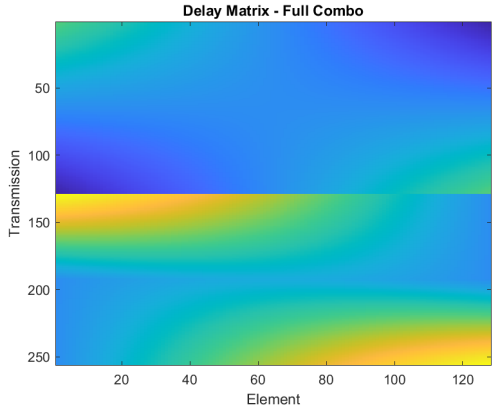

(d) Full Combination (n=256)

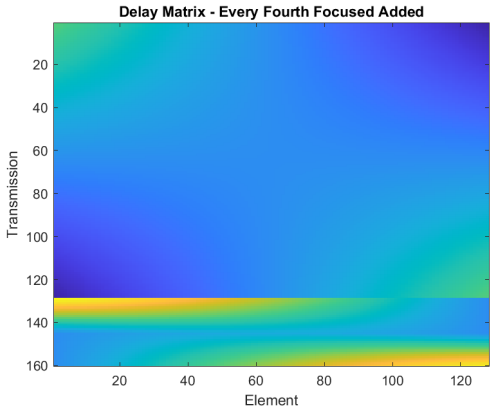

(e) Every Fourth Added (n=160)

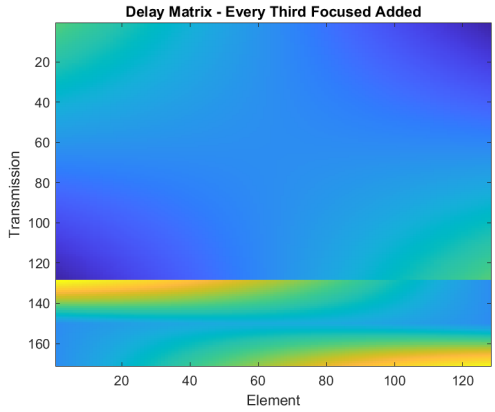

(f) Every Third Added (n=171)

Figure B.2: Delay Matrices - 'Adding' Mixed Sequences

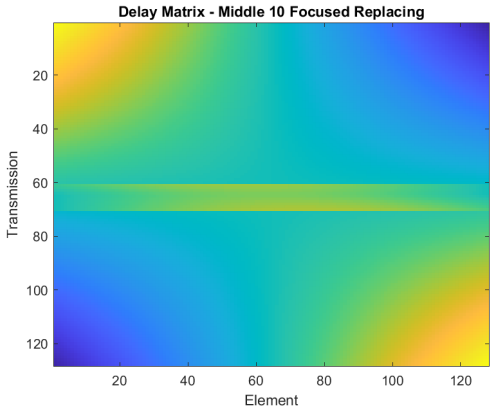

(a) Middle 10 Replacing (n=128)

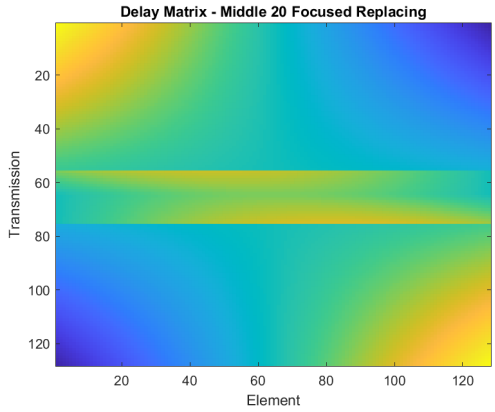

(b) Middle 20 Replacing (n=128)

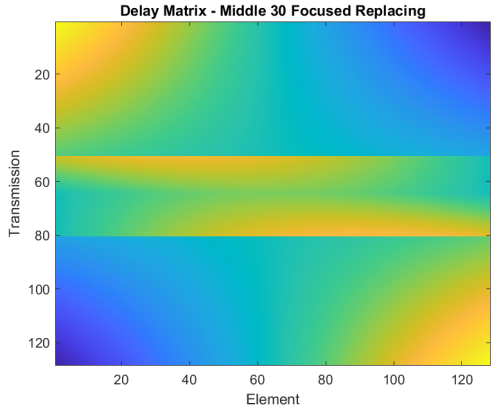

(c) Middle 30 Replacing (n=128)

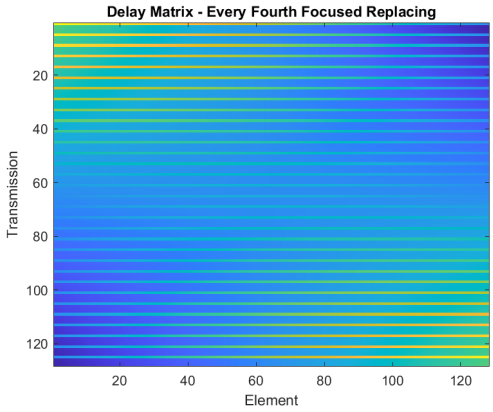

(d) Every Fourth Replacing (n=128)

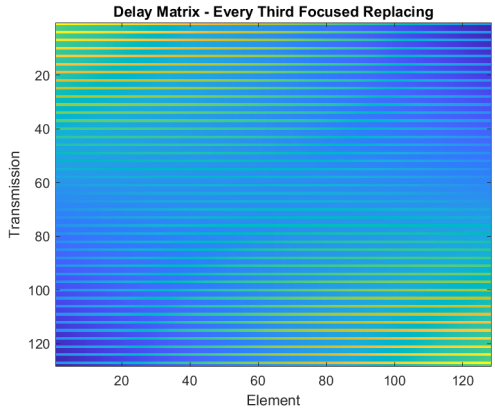

(e) Every Third Replacing (n=128)

Figure B.3: Delay Matrices - 'Replacing' Mixed Sequences